SEAL INLET DISTURBANCE BOUNDARY CONDITIONS FOR ROTORDYNAMIC MODELS AND INFLUENCE OF SOME OFF-DESIGN CONDITIONS ON LABYRINTH ROTORDYNAMIC INSTABILITY

A Dissertation

by

JINXIANG XI

Submitted to the Office of Graduate Studies of
Texas A&M University
in partial fulfillment of the requirements for the degree of

DOCTOR OF PHILOSOPHY

December 2005

Major Subject: Mechanical Engineering

SEAL INLET DISTURBANCE BOUNDARY CONDITIONS FOR ROTORDYNAMIC MODELS AND INFLUENCE OF SOME OFF-DESIGN CONDITIONS ON LABYRINTH ROTORDYNAMIC INSTABILITY

A Dissertation

by

JINXIANG XI

Submitted to the Office of Graduate Studies of
Texas A&M University
in partial fulfillment of the requirements for the degree of

DOCTOR OF PHILOSOPHY

Approved by:

Chair of Committee,	David L. Rhode
Committee Members,	Alan B. Palazzolo
	Hamn-Ching Chen
	Daejong Kim
Head of Department,	Dennis O'Neal

December 2005

Major Subject: Mechanical Engineering

ABSTRACT

Seal Inlet Disturbance Boundary Conditions for Rotordynamic Models and
Influence of Some Off-Design Conditions on Labyrinth Rotordynamic Instability.
(December 2005)

Jinxiang Xi, B.S., Shanghai Jiaotong University, China;
M.S., Xi'an Jiaotong University, China
Chair of Advisory Committee: Dr. David L. Rhode

Systematic parametric studies were performed to better understand seal-inlet rotordynamics. A CFD-perturbation model was employed to compute the seal-inlet flow disturbance quantities. Seal inlet disturbance boundary condition correlations were proposed from the computed seal-inlet quantities using the important parameters. It was found that the cosine component of the seal-inlet swirl velocity disturbance W_{1C} has a substantial impact on the cross-coupled stiffness, and that the correlations for W_{1C} and W_{1S} should be used to replace the historical guess that seal inlet $W_{1C} = 0$ and $W_{1S} = 0$. Also, an extremely precise relationship was found between the swirl disturbance W_{1C} and the seal-inlet swirl velocity $(\omega R_{sh} - \bar{W}_0)$. Thus, the number of experiments or computer runs needed to determine the effect of spin speed, shaft radius and/or inlet swirl velocity on the cross-coupled stiffness is greatly reduced by plotting the simplified relationship of the cross-coupled stiffness against the swirl slip velocity. The benefits of using the new seal-inlet boundary condition correlations were assessed by implementing them into a CFD-perturbation model. Consistently improved agreement with measurements was obtained for both liquid annular seals and gas labyrinth seals.

Further, the well-established CFD-perturbation model with new boundary condition correlations was employed to investigate the rotordynamics of two off-design situations. The first case considered the influence of labyrinth seal teeth damage on the performance and the rotordynamic characteristics of impeller eye seals in centrifugal compressors. The second case considered the influence of rotor-axial-shifting on rotordynamic forces for high-low labyrinth seals in steam turbines during the start-up and shut-down process. The results should provide useful information for labyrinth seal design and fault diagnosis of stability problems in turbines and compressors.

To my parents and my wife Xiuhua

ACKNOWLEDGMENTS

Special thanks goes to Dr. D. L. Rhode for his support, guidance, and constant encouragement during my four years of study. His integrity and enthusiasm for research is a perfect example of a scientist. Under his guidance, I learned not only research expertise, but also his kindness and love of people.

I appreciate the support from Dr. M. Andrews and Dr. H. C. Chen for many insightful discussions on my research. Thanks also goes to Dr. A. B. Palazzolo and Dr. D. Kim. for serving on my committee.

I would like to thank my colleagues Guoguang Su and Jinming Xu. They gave me a lot of help with my research. I also cherish the fellowship and friendship with my brothers, Zhihua Xu and Jian Yang, and E. Kirk for their spiritual support.

Finally, I give my special thanks to my parents and my wife, Xiuhua, for their love, support, and patience. Without their endless love and countless sacrifices, it is impossible for me to finish my research. I would like to share this moment with my lovely wife, Xiuhua and son, Jensen.

All glory to our God!

TABLE OF CONTENTS

CHAPTER Page

LIST OF TABLES

LIST OF FIGURES

FIGURE Page

FIGURE Page

FIGURE Page

CHAPTER I

INTRODUCTION

The increasing power and efficiency of turbomachinery requires reliable turbomachine components (e.g. bearings, dampers, and seals). Non-contacting seals, such as smooth-plain and labyrinth seals, are extensively used in compressors, turbines and pumps to isolate regions of different pressure and to minimize the fluid leakage or sometimes to provide a controlled leakage. However, the interaction between a whirling rotor and the leakage flow generates reaction forces. Operating at high pressures and tight clearances, labyrinth seals may develop a significant force imbalance and many load-dependent instability problems have been attributed to labyrinth seals [1]. As turbomachinery designs continue to push the performance envelope and as the market drives manufacturers to increase service life, the need for advanced sealing continues to grow.

For small radial displacements about an arbitrary rotor position (see Fig. 1), the reaction forces F_y and F_z can be modelled as a linearized set of equations:

$$-\begin{bmatrix} F_y \\ F_z \end{bmatrix} = \begin{bmatrix} K_{yy} & K_{yz} \\ K_{zy} & K_{zz} \end{bmatrix} \begin{bmatrix} y \\ z \end{bmatrix} + \begin{bmatrix} C_{yy} & C_{yz} \\ C_{zy} & C_{zz} \end{bmatrix} \begin{bmatrix} \dot{y} \\ \dot{z} \end{bmatrix} + \begin{bmatrix} M_{yy} & M_{yz} \\ M_{zy} & M_{zz} \end{bmatrix} \begin{bmatrix} \ddot{y} \\ \ddot{z} \end{bmatrix} \tag{1.1}$$

where y, $\dot{y}$, $\ddot{y}$ and $z, \dot{z}, \ddot{z}$ are displacements, velocities, and accelerations in the y and z directions. When the nominal position of the rotor is concentric with respect to the housing, the coefficient matrix becomes simpler and assumes a skew-symmetric form,

---

The journal model is *IEEE Transactions on Automatic Control.*

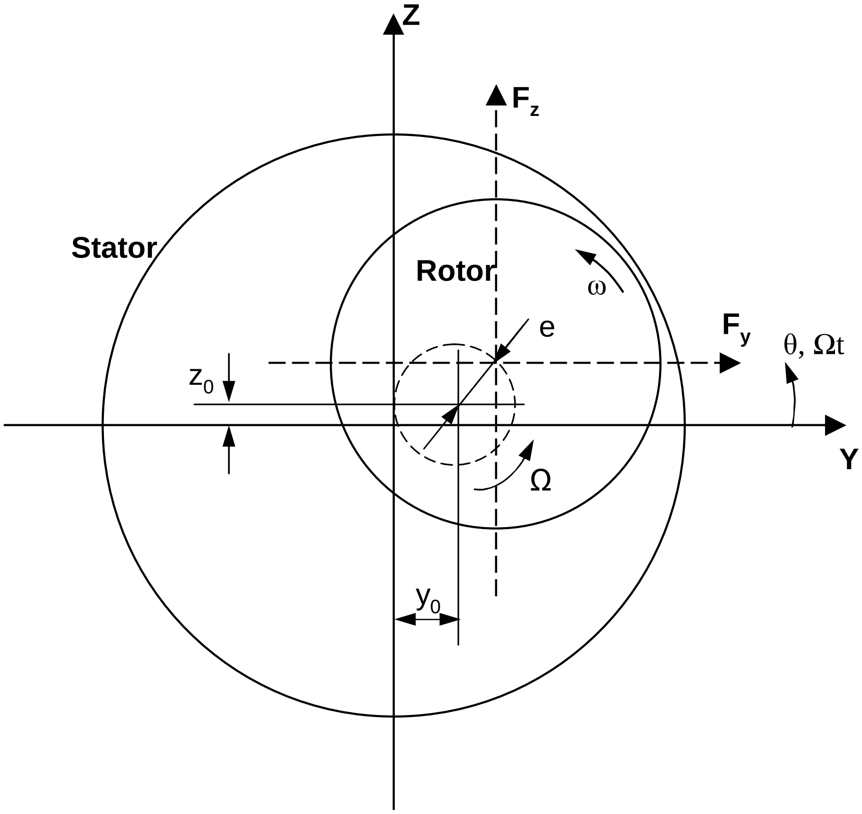

Fig. 1. Forces acting on a rotor whirling about an arbitrary position.

shown as,

$$-\begin{bmatrix} F_y \\ F_z \end{bmatrix} = \begin{bmatrix} K & k \\ -k & K \end{bmatrix} \begin{bmatrix} y \\ z \end{bmatrix} + \begin{bmatrix} C & c \\ -c & C \end{bmatrix} \begin{bmatrix} \dot{y} \\ \dot{z} \end{bmatrix} + \begin{bmatrix} M & m \\ -m & M \end{bmatrix} \begin{bmatrix} \ddot{y} \\ \ddot{z} \end{bmatrix} \tag{1.2}$$

K and k are the direct and cross-coupled stiffness coefficients, C and c are the direct and cross-coupled damping coefficients, and M and m are the direct and cross-coupled inertial coefficients, respectively. For counterclockwise whirling rotor, the resulting radial and tangential forces are shown in Fig. 2. Among the above force coefficients, the tangential components k and C are important in the determination of the rotor-dynamic stability. A positive value of k represents a destabilizing stiffness force (*i.e.*

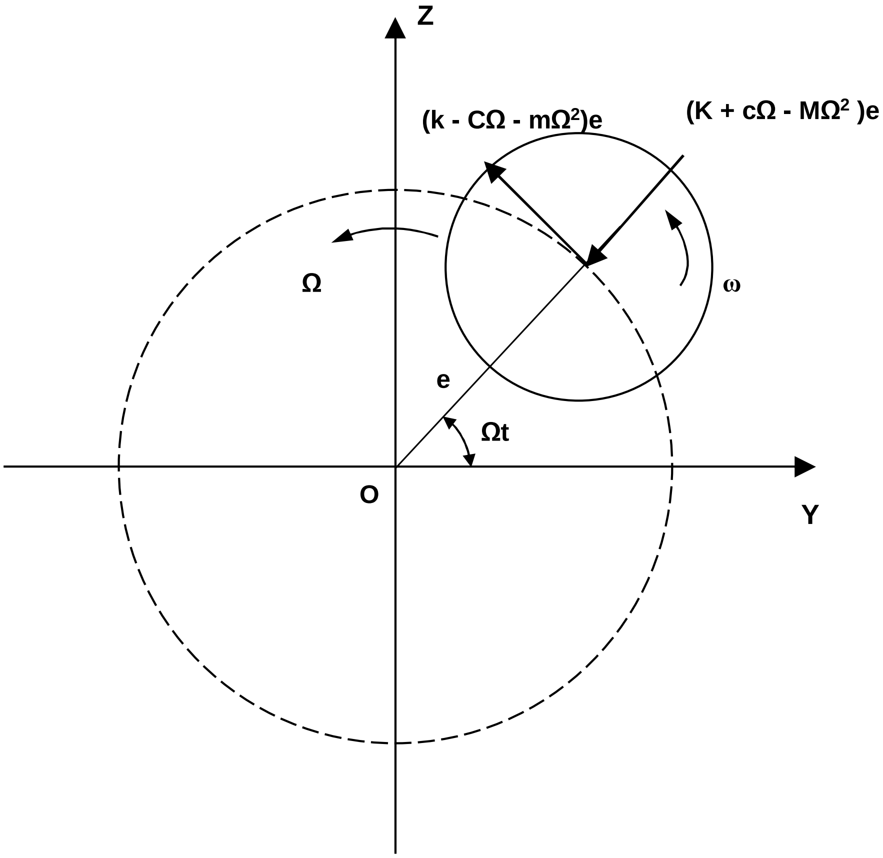

Fig. 2. Forces acting on a rotor whirling about the stator center.

acting in the whirl direction), and a positive value of C represents a stabilizing damping force (*i.e.* acting against the whirl). The combined effect of these two coefficients forms the effective damping C_{eff} $[= C - k/\Omega]$ for which a positive value represents a whirl resisting force. Specifically, the cross-coupled stiffness k is a crucial element in establishing rotordynamic stability or instability. Although k is small in magnitude compared to its bearing or liquid-seal counterparts, seals are sometimes located at locations of large shaft displacement, and their k values can easily be the difference between stable and unstable operations. Therefore, it is necessary to predict these force coefficients accurately.

Research efforts to predict the reaction force date back to 1965 when Alford [2] reported the initial analysis for labyrinth seals. Bulk flow models were proposed and refined by Black and Jensen [3] and Childs [4], [5], among others. The quasi-three-dimensional CFD-perturbation approach was introduced to improve the accuracy shortcoming of labyrinth bulk flow models and to reduce the large CPU requirement of full 3-D CFD models. The CFD-perturbation approach is somewhat similar to that of bulk flow models. The main difference lies in the treatment of the governing equations. Diezen and Nordmann [6] developed the first CFD-perturbation model based on a coordinate transformation approach. However, the coordinate transformation is not exact for complicated seal geometries. More recently, Kim and Rhode [7] developed a version to approximate the boundary conditions on the disturbed rotor surface which avoids the coordinate transformation and is applicable for axisymmetric seals of any geometry. Due to that lack of information, nearly all existing seal rotordynamics models give incorrect domain-inlet boundary conditions for the first-order (*i.e.* flow disturbance) quantities. Specifically, the first-order swirl velocity seal-inlet boundary condition has sine and cosine components W_{1S} and W_{1C} that have historically been assumed as zero, whereas Kim and Rhode [7] showed that this is unrealistic. An additional concern is that existing models typically use a perturbed Bernoulli type of equation to relate the first-order axial velocity and pressure at the seal-inlet boundary, but this approach must rely on a very uncertain inlet loss coefficient. Recently, Venkatesan and Rhode [8] developed correlations for first-order domain-inlet boundary condition values located in the upstream chamber. However, existing bulk-flow models do not immediately allow the presence of an upstream chamber. Further, the presence of an upstream chamber within the domain of fully-3D and CFD-perturbation models sometimes gives numerical stability problems.

A. Research Need

The lack of universally applicable modelling in existing rotordynamics bulk flow perturbation codes , for example, for labyrinth seals has led to serious vibration problems for some compressors, stream turbines and pumps. Specifically, inaccurate estimates of the labyrinth seal force coefficients from bulk flow models was recently shown to be at the root of this problem. For example, evidence of the large discrepancy between Dr. Childs' bulk flow model prediction and his measurements for the labyrinth rotordynamic driving force was shown by Childs [1] for the challenging cases of high speeds and high supply pressures.

All the previous seal rotordynamic models (*i.e.* bulk flow, CFD-perturbation and full 3-D CFD) specified the seal-inlet first-order boundary condition by either the assumption of zero values for all disturbed variables or a perturbed Bernoulli equation to relate the first-order pressure and streamwise velocity through an empirical minor loss coefficient at the seal inlet. In almost every case, the first-order seal-inlet swirl disturbance components were guessed to have zero values and the seal-inlet minor loss coefficient was guessed as 0.5.

The assumption of zero values for both components of the first-order flow disturbance swirl velocity at the seal inlet has never been verified. Kim and Rhode [7] showed that the previously guessed zero value for the inlet swirl disturbance in labyrinth seals is unrealistic. Venkatesan and Rhode [8] for the first time specified the swirl disturbance through a correlation. However, the applicability of this correlation suffered from the fact that it was developed from test cases with a confined range of geometry and operating conditions without parametric study of each quantity's influence. Moreover, very little information is available about the influence of the upstream chamber on the first-order variables at the seal inlet. Since the boundary conditions are what determine each particular solution of the governing equation, they are extremely important and must be quantified to allow improved solutions from all gas and liquid models.

The analysis of the transient conditions of turbines and compressors is essential for safe operations in power and propulsion systems. Transient operations such as load changes and start-ups in complex industrial processes have been found to cause many vibration problems. Two distinct issues of such problems such as teeth damage and relative axial rotor growth have been long recognized in industrial practice while unfortunately, still remain unexplored.

Labyrinth seal teeth damage in rotating machinery often happens during a machine's service life. Damage from rotor impacting and/or intense rubbing is the most frequently encountered cause of damage, which occurs when the machine undergoes transients or severe vibrations. Sudden load changes of a centrifugal compressor, for example, could generate severe rubs of the labyrinth and cause the teeth tips to "mushroom" out, which increases the radial clearance and creates undesirable flow characteristics across the labyrinth. These factors are detrimental to a compressor's efficiency and rotordynamic stability, and could be the root cause for persistent and worsening rotor vibration [9]. In addition, higher differential pressure, and hence larger thrust loading of the machine will arise from the excessive gas leakage from the discharge end seal.

Rotors in large rotating steam turbines experience noticeable thermal axial growth during transient operations such as the start-up process. The rotor axial shifting caused by the thermal expansion and/or by net pressure loads could significantly alter the performance and rotordynamic forces of the sealing labyrinth. The seal forces could contribute to the rotordynamic instability of the rotor-bearing-seal system even though the force magnitude is smaller than that of the bearing fluid film forces. As the rotating speed increases or the seal clearance decreases, the labyrinth-seal-excited problems often become more and more critical in the system design. It is therefore necessary to predict these forces accurately for both reliable operations and safer design of high-performance steam turbines.

B. Objectives

The present study was partially motivated by the worrisome lack of reasonable estimates of the first-order, *i.e.* flow disturbance variables at the seal inlet, especially the disturbed swirl velocities, and the compromised applicability of Venkatesan's correlation in the upstream chamber given by Venkatesan and Rhode [8]. In addition, given the exceptional importance of self-excited vibrations, the present paucity of reported data on rotordynamic characteristics under these off-design circumstances is discouraging. The objectives are:

1. To better understand the fluid dynamics at the seal inlet, and to develop a seal-inlet boundary condition correlation for disturbance quantities with simplicity, breadth of application, and relative freedom from numerical difficulties.

2. To evaluate how much solution improvement to expect from the newly-developed seal-inlet boundary condition correlation by comparing with measurements of both gas and liquid seal situations.

3. To apply the CFD-perturbation model with the boundary condition correlation developed herein to investigate the rotordynamic characteristics of selected labyrinth seals in rotating machinery, as well as to gain insight into various effects on the seal-inlet swirl which affects seal rotordynamics.

CHAPTER II

LITERATURE REVIEW

A. Rotordynamics Models

Theoretical investigations to predict the rotordynamic coefficients of seals and dampers can be classified into three approaches. The first approach involves bulk-flow models with simplified assumptions about the flow field and requires minimal computing resources. The second approach, solving three-dimensional Navier-Stokes equations, captures the flow phenomena more accurately than the bulk-flow models, although it needs much more CPU time. The third approach, using a quasi-three-dimensional CFD-perturbation model (i.e. 2-D computing), has a significant advantage because of its ability to model the flow field more realistically than the bulk-flow models, while requiring much less computational resources than 3-D CFD analysis.

The bulk-flow models, based on the thin film assumption, use radially averaged flow variables and remove the radial momentum equation. Assuming small rotor displacement, the generic flow variable can be approximated by,

$$\Phi\left(x,r,\theta,t\right)=\Phi_0\left(x,r\right)+\epsilon\left\{\Phi_{1C}\left(x,r\right)\cos\left(\Omega t-\theta\right)-\Phi_{1S}\left(x,r\right)\sin\left(\Omega t-\theta\right)\right\} \tag{2.1}$$

The nonlinear governing equations are perturbed using the above perturbation relation, resulting in two sets of equations, referred to as the zeroth- and first-order equations. The zeroth-order solution gives the mean flow variables of the concentric rotor position, while the first-order solution gives the disturbed velocity and pressure field from which the rotordynamic force coefficients are evaluated.

The initial rotordynamic analysis was reported by Alford [2] for labyrinth seals. Black and Jensen [3] first introduced a bulk flow model to analyze the influence of annular seal forces on the dynamics of centrifugal pumps. This model was extended by Iwatsubo [10] for labyrinth seals by including the effect of circumferential flow. Based on Hirs' turbulent lubrication empirical equation, Childs [4] and [5] developed an analytical-computational method for short and finite length annular liquid seals. This work was advanced by Nelson [11] who proposed a revised model by utilizing Moody's equation to better describe the seal surface roughness. A two-control-volume bulk flow model was presented by Wyssmann, et al. [12] who divided the cavity flow field into a jet flow and a cavity flow, followed by the improvements of Scharrer [13] who considered the recirculation flow inside the labyrinth cavity. Further, San Andes [14] and [15] analyzed the annular seal force with a model accounting for cylindrical and conical whirling motions, respectively. More recently, Marquette and Childs [16] developed a three-control-volume model for liquid grooved seals to account for the flow separation and mixing inside the seal.

The advantage of the bulk flow models is less computing time compared to CFD-based rotordynamic models. The disadvantage is their reduced prediction accuracy which results from neglecting the separation and recirculation prevalent in labyrinth cavities and not properly accounting for the effect of circumferential flow.

Methods dealing with separation and recirculation flows without using user-provided correlations are based on fully 3-D, time-averaged Navier-Stokes equations. Tam, et al. [17] first reported the flow field in a centered, whirling smooth-plain seal. Athavale, et al. [18] presented unsteady, fully 3-D solutions for gas annular seals to simulate the measurements by Childs and Scharrer [19]. Rotordynamic analysis for labyrinth seals based on three-dimensional solutions was first given by Rhode, et al. [20] and [21], followed by Isshi, et al. [22], who used a different turbulence model. Unlike the finite volume methods mentioned above, Baskharone and Hensel [23] developed a three-dimensional finite element approach using deformable mesh arrangements. Although the full 3-D models have a chance to better describe the rotordynamic phenomena, they have suffered from numerical limitations, such as the iteration convergence problem and the tremendous CPU requirement.

The quasi-three-dimensional perturbation model was introduced to improve the accuracy problem of bulk flow models and to lessen the large CPU requirement of full three-dimensional models. The perturbation concept is similar to that of the bulk flow models. The difference lies in the treatment of the flow domain and the governing equations. Dietzen and Nordmann [6] developed the first CFD-perturbation model based on a coordinate transformation approach. However, this model is not applicable when the seal geometry is not plain, i.e. for grooved, labyrinth, stepped seals, etc. Arghir and Frene [24] extended the applicability of the above coordinate transformation approach to complex seal geometries by introducing linear interpolation functions. Kim and Rhode [7] and Kim, et al. [25] proposed an approach to approximate the boundary conditions on the disturbed rotor surface (PDBC) which avoided the limitation due to coordinate transformation and is applicable for axisymmetric seals of any geometry. Venkatesan and Rhode [8] developed correlations for boundary conditions at the upstream chamber and the seal inlet, and for the first time the swirl disturbance boundary condition was specified as a function of the seal geometry and the operating condition quantities. However, the applicability of Venkatesan's correlation is uncertain because it was developed from a limited number of test cases without a complete parametric study of the influence of seal geometry and operating conditions on the inlet flow disturbance quantities.

B. Disturbance Boundary Conditions

A great amount of literature exists describing how to specify undisturbed (*i.e.* zeroth-order) boundary conditions for labyrinth seals, and it is not intended to review them here. The book by Patankar [26] and a review by Gresho [27] are suggested as starting points for understanding this subject in more detail. In what follows, the methods of specifying disturbance boundary conditions for the first-order governing equations will be briefly reviewed.

1. Up-Chamber Domain Inlet Boundary Conditions

A turbomachinery seal has an up-chamber immediately upstream as well a back-chamber immediately downstream of the seal. Nearly all the perturbation models discussed earlier have excluded these two chambers from the seal and only the seal itself was modelled as the computational domain. Partially motivated by skeptics about the zero assumption of the disturbance swirl velocities at the seal inlet, Kim and Rhode [7] examined the effect of including both the upstream and downstream chambers. The upstream chamber inlet disturbance boundary conditions are given by:

$$\hat{\Phi}_1(x_{in}, r) = 0; \{\hat{\Phi}_1 = \hat{U}_1, \hat{V}_1, \hat{W}_1\} \tag{2.2}$$

$$\left.\frac{\partial \hat{P}_1'(x, r)}{\partial x}\right|_{x=x_{in}} = 0 \tag{2.3}$$

By starting the computations with the above boundary conditions, they found an abrupt change in the axial distribution of the first-order velocities and pressures at the seal inlet. It is straightforward to assume that the magnitude of disturbance quantities developed inside the upstream chamber will have a certain influence upon the results. Therefore, to minimize the uncertainty from the seal inlet boundary condition, the computational domain is recommended to include the upstream chamber where the flow disturbance is expected to begin. For example, Moore and Palazzolo [28] included an upstream chamber in their rotordynamic force prediction for liquid annular seals.

Venkatesan and Rhode [8] developed an approach of specifying the domain-inlet boundary swirl disturbance variables through a correlation at an upstream chamber location. The disturbance quantities were evaluated using STAR-CD by subtracting the three-dimensional numerical solutions for the concentric rotor position from those for an eccentric rotor position. This correlation, however, was greatly limited by the presence of the upstream chamber. Bulk-flow perturbation models, for example, do not immediately allow locating the domain inlet in the upstream chamber. Further, the presence of an upstream chamber in the computational domain sometimes gives numerical stability problems for 3D-CFD and CFD-perturbation approaches.

2. Seal Inlet Boundary Conditions

The disturbance flow variables are often unknown at the seal inlet. The inlet, as well as exit boundary conditions must take into account the inertia effects developed in the domains external to the seal. These conditions are usually specified using the perturbed Bernoulli's equation [1]:

$$\hat{U}_1(x_{in}, r) = -\frac{\hat{P}_1(x_{in})}{\rho U_0(1+\xi_{in})} \tag{2.4}$$

$$\hat{P}_1(x_{in}, r) = -\rho(1-\xi_{in})U_0(x_{in})\hat{U}_1(x_{in}) \tag{2.5}$$

A value of 0.5 has often been adopted for the inlet minor loss coefficient ξ_{in}. Eq. (2.4) represents a boundary condition for the first order axial velocity. The other two components have often been assumed undisturbed in the inlet section.

$$\hat{V}_1(x_{in}) = 0, \quad \hat{W}_1(x_{in}) = 0 \tag{2.6}$$

This method was followed by bulk flow modelers like Childs [4], [5], Nelson [11], San Andes [14], [15] and CFD-perturbation modelers like Dietzen [6], [29], Arghir [30], [31], [24] in their seal-inlet boundary condition formulations.

As noted earlier, Kim and Rhode [7] found a sharp peak in the axial dostribution of the disturbance variables near the seal inlet. Their findings showed that the previous assumption $W_{1C} = W_{1S} = 0$ in labyrinth seals is unrealistic and needs to be improved for an accurate prediction of the flow-induced dynamic forces. In this research, a new approach will be developed for specifying flow disturbance boundary conditions at the seal inlet for labyrinth seal perturbation rotordynamics models.

Kim and Rhode [7] also found that the disturbance flow variables have relatively smooth profiles at the seal exit region and showed that the downstream chamber can be excluded from the computational domain without affecting the solution significantly.

3. Seal Exit Boundary Conditions

The Neumann boundary condition for disturbance velocities at the seal exit are given as:

$$\left.\frac{\partial \hat{\Phi}_1(x_{ex}, r)}{\partial x}\right|_{x=x_{ex}} = 0; \quad \{\hat{\Phi}_1 = \hat{U}_1, \hat{V}_1, \hat{W}_1\} \tag{2.7}$$

The exit pressure boundary condition is obtained by perturbing the approximate energy equation between the seal exit and the downstream chamber using the bulk values of the variables, *i.e.* U, W, and P.

$$\hat{P}_1(x_{ex}, r) = -\rho(1-\xi_{ex})[U_0(x_{ex})\hat{U}_1(x_{ex}) + W_0(x_{ex})\hat{W}_1(x_{ex})] \tag{2.8}$$

The minor loss coefficient ξ_{ex} ranges from 0.9 to 1.1. The disturbance pressure is zero when $\xi_{ex} = 1.0$.

4. Wall Boundary Conditions

In general, the disturbance velocity components have zero values on the stator surface as expected and non-zero values on the the rotor surface due to the rotor displacement.

As discussed previously, Dietzen and Nordmann [6] developed a model based on an analytical coordinate transformation to remove the boundary condition problem due to the nominally eccentric position of the rotor. Because of the mathematical complexities, this model is only applicable to plain seal geometries. Arghir and Frene [24] extended the applicability of Dietzen and Nordmann's approach to complex seal geometries by assuming an axially linear distribution of the disturbance quantities. Utilizing the Taylor series expansion method, Kim and Rhode [7] proposed a perturbation approach for the disturbed boundary conditions (PDBC) on the rotor surface. This approach avoids the mathematical difficulties of a coordinate transformation and is applicable for axisymmetric seals of any geometry.

Without loss of generality, we assume $t = 0$ here. The absolute velocities on the disturbed rotor surface can be approximated as follows:

$$x : U(x, R^* + \epsilon C_r \cos\theta, \theta) = 0 \tag{2.9}$$

$$r : V(x, R^* + \epsilon C_r \cos\theta, \theta) = \epsilon C_r (\Omega - \omega) \sin\theta \tag{2.10}$$

$$\theta : W(x, R^* + \epsilon C_r \cos\theta, \theta) = R^* \omega + \epsilon C_r \Omega \cos\theta \tag{2.11}$$

Here the perturbation parameter is $\epsilon = e_0/C_r$ and has the relation $\epsilon \ll 1$. Applying the perturbation equation, *i.e.* Eq. (2.1) into Eq. (2.9) and by Taylor series expansion, the Dirichlet boundary condition for the the disturbance velocities is derived as:

$$U_0(x, R^*) + \epsilon C_r \left.\frac{\partial u(x,r)}{\partial r}\right|_{R^*} \cos\theta + \epsilon[U_{1C}(x, R^*)\cos\theta + U_{1S}(x, R^*)\sin\theta] + O(\epsilon^2) = 0 \tag{2.12}$$

Grouping the coefficients of $\cos\theta$ and $\sin\theta$ terms and equating them to zero yields the boundary conditions for the axial disturbance velocities on the rotor surface, which in complex form are expressed as:

$$\hat{U}_1(x, R^*) = -C_r \left. \frac{\partial U_0(x,r)}{\partial r} \right|_{R^*} \tag{2.13}$$

Similarly, the disturbance boundary conditions for radial and circumferential velocity components can be derived as:

$$\hat{V}_1(x, R^*) = -C_r \left. \frac{\partial V_0(x,r)}{\partial r} \right|_{R^*} + \mathbf{j} C_r(\Omega - \omega) \tag{2.14}$$

$$\hat{W}_1(x, R^*) = C_r \left[\Omega - \left. \frac{\partial W_0(x,r)}{\partial r} \right|_{R^*} \right] \tag{2.15}$$

The above Eqs. (2.13) - (2.15) constitute the Dirichlet boundary conditions for the first-order velocities on the perturbed rotor surface. For any flow variable having a zeroth-order Neumann boundary condition such as pressure, it will also have a first-order Neumann boundary condition.

C. Previous Works on Damaged Teeth and Rotor Shifting

Rotating machinery is an integral part of process equipment in chemical, oil, and gas industries. Abnormal operations or failures of rotating machinery can result in performance deterioration, damage to other equipment, and production loss. An unexpected outage of the process unit may easily result in loss of production revenues of $10,000 per hour [32]. Excessive vibrations of rotating equipment have been reported as frequent causes of the unit failure [33], [34], [35]. Due to their critical nature, rotating equipment has been routinely subjected to maintenance to avoid unpredicted shutdowns.

Numerical analysis has become a powerful tool in the design and failure diagnosis of turbomachinery components. The insight afforded by such analysis provides further understandings of the complexity of turbomachinery flow physics. Considerable numerical efforts have been undertaken in the area of transient analysis relating to both performance and vibrations. Readers can find more detail in White [36], Meher-Homji and Bhagave [37], and Lakshminarasimha, et al. [38], etc. Using a bulk flow model, San Andes [15] reported a numerical analysis of the effect of shaft misalignment on the dynamic force response in liquid annular seals.

One important issue that gains more and more attention is the seal damage influence upon leakage and dynamic forces. Sudden load changes could induce excessive rotor vibration and severely damage the aluminum labyrinth teeth, causing the teeth tips to mushroom out and the teeth clearance to increase. Undesirable flow characteristics can be developed across the labyrinth and further degrade its efficiency and rotordynamic stability. Higher differential pressure and hence larger thrust loading of the machine will arise from an excessive gas leakage from the discharge end seal [9]. Furthermore, the possibility of rubbing damage due to force/thermal imbalances increases with reduced seal clearance and increasing running speed. Therefore, an accurate prediction of performance deterioration and rotordynamic force variations during off-design operational conditions is necessary to estimate the dynamic behavior and to avoid rotor vibration. The effects of seal tooth thickness and radial clearance upon labyrinth seal flow leakage have been reported by Rhode and Hibbs [39] [40]. It has been found that the radial clearance has a major effect on the labyrinth seal performance while the tooth thickness exerts a negligible effect. Zimmermann, et al. [41] obtained leakage results for a few seals with worn tooth seal tips for straight-through and stepped labyrinths. Childs [42] studied the seal clearance effects on spiral vibrations due to rubbing and showed that an increased clearance could improve the system's stability, in particular with regard to unstable spiral vibrations.

The influence of leakage path inlet swirl on annular seal rotordynamics was experimentally investigated by Guinzburg, et al. [43] and Hsu and Brennen [44] with water as the working fluid. A destabilizing effect was found arising from increasing inlet swirl for both normal and tangential forces. More recently, Wilcox and O'Brien [9] presented an in-depth fault diagnosis of stability problems in a centrifugal compressor and identified the rub-damaged buffer gas seals as the root cause for the persistent and worsening rotor vibrations.

A considerable amount of work has been done to circumvent the teeth/rotor damage problem especially in centrifugal compressors. An exhaustive review of them will not be given here. One option is to use thermoplastic seals in place of the aluminum labyrinth [45], [46]. The main benefit of the thermoplastic labyrinth is reducing the radial clearance and maintaining these tight clearances through transient operations without damaging the shaft. With proper application, substantial compressor efficiency improvement can be achieved by reducing the seal leakage. However, this type of seal is more fragile than aluminum seals and it can be damaged while being handled. It is not widely adopted because of its chemical compatibility to the specific process and stress variation under high pressures and high temperatures.

Another option to lessen the teeth damage problem is to use honeycomb seals which are more robust than aluminum seals when a rub occurs [1], [47]. Due to their unique structure, the honeycomb seals allow abrasive wear during the contact between the rotating and stationary parts and will not typically harm the rotor surface. Honeycomb seals also have the benefit of reducing the averaged circumferential velocity within the seal and consequently the cross-coupled stiffness k. When properly designed, this type of seal has been successfully used as a balance-drum in compressors and as turbine interstage seals in high-pressure turbopumps [1]. A careful stress analysis is necessary before using honeycomb applications in order to avoid structural failure, as Benaboud, et al. [48] have reported such problems in a high-pressure compressor.

Also of importance to turbomachinery rotordynamics is the rotor axial shifting under transient operations. Specifically, rotors in large steam turbines experience noticeable thermal axial growth during the start-up process and could considerably alter the rotordynamic forces of labyrinth seals. Baumann [49] investigated the damping behavior for a high-pressure radial compressor and mentioned that axial rotor positions seemed to have an insignificant influence on tangential forces and hence couldn't be verified as the root cause for the system instability. More recently, Wang, et al. [50] studied the flow characteristics in stepped seals when teeth disengagements occur due to axial movement and showed that the airflow features are largely dictated by the distance between the teeth tip and the step. In their leakage prediction inside straight-through labyrinths with rub-grooves, Rhode and Adams [51] discussed the effect of the labyrinth tooth tip location due to the centrifugal force and thermal growth of the rotor and stator. The influence of rotor-shifting on rotordynamic force variations in labyrinth seals, however, still remains unexplored.

CHAPTER III

CFD-PERTURBATION ROTORDYNAMIC MODEL

A. Perturbed Governing Equations

1. Perturbation Method

The flow field in the eccentric seal clearance, as shown in Fig 3, is characterized as unsteady, three-dimensional and turbulent. The governing equations are the Reynolds-averaged, turbulent Navier-Stokes equations in a stationary reference frame

$$\frac{\partial(\rho u_i)}{\partial t}+\frac{\partial}{\partial x_j}(\rho u_i u_j)=-\frac{\partial P}{\partial x_i}+\frac{\partial \tau_{ij}}{\partial x_j} \tag{3.1}$$

and the continuity equation

$$\frac{\partial \rho}{\partial t}+\frac{\partial}{\partial x_j}(\rho u_j)=0 \tag{3.2}$$

The Reynolds stress is given in the cylindrical coordinate system as:

$$[\tau_{ij}]=\begin{bmatrix} 2\mu_e\dfrac{\partial u}{\partial x}-\Pi & \mu_e\left(\dfrac{\partial u}{\partial r}+\dfrac{\partial v}{\partial x}\right) & \mu_e\left(\dfrac{1}{r}\dfrac{\partial u}{\partial \theta}+\dfrac{\partial w}{\partial x}\right) \\ \mu_e\left(\dfrac{\partial u}{\partial r}+\dfrac{\partial v}{\partial x}\right) & 2\mu_e\dfrac{\partial v}{\partial r}-\Pi & \mu_e\left(r\dfrac{\partial}{\partial r}\left(\dfrac{w}{r}\right)+\dfrac{1}{r}\dfrac{\partial v}{\partial \theta}\right) \\ \mu_e\left(\dfrac{1}{r}\dfrac{\partial u}{\partial \theta}+\dfrac{\partial w}{\partial x}\right) & \mu_e\left(r\dfrac{\partial}{\partial r}\left(\dfrac{w}{r}\right)+\dfrac{1}{r}\dfrac{\partial v}{\partial \theta}\right) & 2\mu_e\left(\dfrac{1}{r}\dfrac{\partial w}{\partial \theta}+\dfrac{v}{r}\right)-\Pi \end{bmatrix} \tag{3.3}$$

and

$$\Pi=\frac{2}{3}\rho k+\mu_e\left[\frac{\partial u}{\partial x}+\frac{1}{r}\frac{\partial}{\partial r}(rv)+\frac{1}{r}\frac{\partial w}{\partial \theta}\right] \tag{3.4}$$

where μ_e is the effective turbulent viscosity. This quantity is evaluated as the sum of the laminar viscosity and turbulent viscosity, i.e. $\mu_e=\mu+C_\mu\rho k^2/\varepsilon$ with $C_\mu=0.09$. Assuming medium to high Re, which has widely been found in turbomachinery seals,

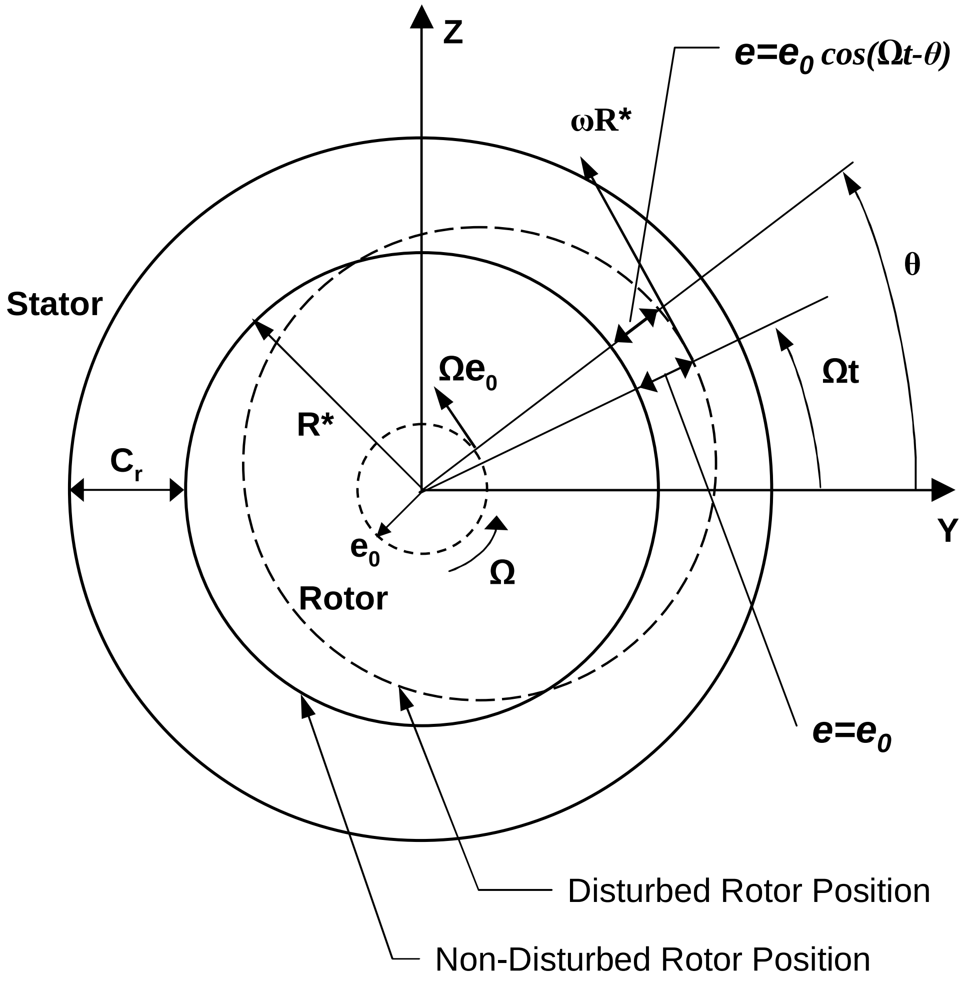

Fig. 3. Geometric and kinematic relationship of circular rotor whirl about the stator center at t = 0, ω: rotating speed; Ω: whirling speed.

the standard form of the $k-\epsilon$ turbulence model is used. The governing equations for the turbulent kinetic energy k and the turbulent energy dissipation ϵ are:

$$\rho\frac{\partial \mathrm{k}}{\partial t}+\frac{\partial}{\partial x_i}\left(\rho u_i \mathrm{k}\right)=\frac{\partial}{\partial x_i}\left(\frac{\mu_e}{\sigma_{\mathrm{k}}}\frac{\partial \mathrm{k}}{\partial x_i}\right)+\tau_{ij}\frac{\partial u_i}{\partial x_j}-\rho\varepsilon \tag{3.5}$$

$$\rho\frac{\partial \varepsilon}{\partial t}+\frac{\partial}{\partial x_i}\left(\rho u_i \varepsilon\right)=\frac{\partial}{\partial x_i}\left(\frac{\mu_e}{\sigma_{\varepsilon}}\frac{\partial \varepsilon}{\partial x_i}\right)+\frac{\varepsilon}{k}\left(c_1\tau_{ij}\frac{\partial u_i}{\partial x_j}-c_2\rho\varepsilon\right) \tag{3.6}$$

The empirical constants are $c_1 = 1.44$, $c_2 = 1.92$, $\sigma_k = 1.0$, and $\sigma_\varepsilon = 1.3$ [52]. When the working fluid is compressible, the equation of state is also employed:

$$P=\gamma\rho RT \tag{3.7}$$

where γ is the compressibility factor and R is the universal gas constant.

This model assumes a circular rotor motion about the housing center position with an obit radius that is small relative to the seal clearance. Transient 3-D CFD solutions for a labyrinth seal would require enormous computer resources. However, based on the observation that the boundaries (i.e. radial clearance) are both temporally and circumferentially periodic, and assuming that the eccentricity of the rotor is small compared with the seal radial clearance, one can approximately decompose the position of the displaced rotor surface into a steady, axisymmetric part and a small, unsteady, asymmetric part (see Fig 3) as:

$$R\left(\theta,t\right)=R^{*}+\epsilon\mathrm{Re}\left\{C_r e^{\mathrm{j}\left(\Omega t-\theta\right)}\right\} \tag{3.8}$$

where R^* represents the concentric-rotor surface location and j indicates an imaginary number. Assuming that velocities, pressure and density can also be considered to have a steady and axisymmetric part as well as an unsteady and asymmetric part, one can write a general expression for them as:

$$\Phi\left(x,r,\theta,t\right)=\Phi_0\left(x,r\right)+\epsilon\mathrm{Re}\left\{\hat{\Phi}_1\left(x,r\right)e^{\mathrm{j}\left(\Omega t-\theta\right)}\right\} \tag{3.9}$$

where Φ is a generic fluid flow variable, and $\epsilon = \mathrm{e}/C_r$ with $\mathrm{e} << C_r$. Further, Φ_0 represents the axisymmetric (zeroth-order, *i.e.* undisturbed) part, while the complex first-order variable $\hat{\Phi}_1$ is the first-order, *i.e.* disturbed part varying only in the x-r space. Equation (3.9) implies that the rotor whirl motion of a small eccentricity generates a periodic flow disturbance. When the complex function is defined as $\hat{\Phi}_1 = \Phi_{1C} + \mathbf{j}\Phi_{1S}$, Eq. (3.9) can be expressed in a simpler form as:

$$\Phi\left(x,r,\theta,t\right) = \Phi_0\left(x,r\right) + \epsilon\left\{\Phi_{1C}\left(x,r\right)\cos\left(\Omega t-\theta\right) - \Phi_{1S}\left(x,r\right)\sin\left(\Omega t-\theta\right)\right\} \quad (3.10)$$

Observe that the cosine flow disturbance component, for example W_{1C}, represents the 2-D function $W_{1C}(x,r)$ for the θ-plane at the circumferential position of the minimum seal clearance as shown in Fig. 3. Similarly, the sine flow disturbance component represents the 2-D function $W_{1S}(x,r)$ for the θ-plane at the circumferential position that is 90^o ahead of the minimum seal clearance. Because this method is applicable only to a very small rotor displacement amplitudes about the housing centerline, it is assumed that the turbulent viscosity, turbulent kinetic energy and turbulent energy dissipation are not significantly influenced by the very slight rotor displacement. By substituting Eqs. (3.3), (3.4), and (3.10) into Eqs. (3.1) and (3.2), the zeroth- and first-order equations are obtained. Additional details are available in [25].

2. Zeroth-Order Equations

Continuity equation:

$$\frac{\partial}{\partial x}\left(\rho_0 u_0\right) + \frac{1}{r}\frac{\partial}{\partial r}\left(r\rho_0 v_0\right) = 0 \quad (3.11)$$

General momentum equation:

$$\frac{\partial}{\partial x}\left(\rho_0 u_0 \Phi_0\right) + \frac{1}{r}\frac{\partial}{\partial r}\left(r\rho_0 v_0 \Phi_0\right) = \frac{\partial}{\partial x}\left(\mu_e\frac{\partial \Phi_0}{\partial x}\right) + \frac{1}{r}\frac{\partial}{\partial r}\left(r\mu_e\frac{\partial \Phi_0}{\partial r}\right) + S\left(\Phi_0\right) \quad (3.12)$$

Where the source terms for each variable are given as:

$$\begin{aligned} S\left(u_0\right) = &-\frac{\partial p_0}{\partial x} + \frac{1}{3}\frac{\partial}{\partial x}\left(\mu_e\frac{\partial u_0}{\partial x}\right) + \frac{1}{r}\frac{\partial}{\partial r}\left(r\mu_e\frac{\partial v_0}{\partial x}\right) - \frac{2}{3}\frac{\partial}{\partial x}\left(\rho_0 k\right) \\ &- \frac{2}{3}\frac{\partial}{\partial x}\left[\mu_e\left(\frac{\partial v_0}{\partial r} + \frac{v_0}{r}\right)\right] \end{aligned} \tag{3.13}$$

$$\begin{aligned} S\left(v_0\right) = &-\frac{\partial p_0}{\partial r} + \frac{1}{3r}\frac{\partial}{\partial r}\left(r\mu_e\frac{\partial v_0}{\partial r}\right) - \frac{2}{3}\frac{v_0}{r}\frac{\partial \mu_e}{\partial r} - \frac{2}{3}\frac{\partial}{\partial r}\left(\mu_e\frac{\partial u_0}{\partial x}\right) \\ &- \frac{4}{3}\mu_e\frac{v_0}{r^2} + \frac{\partial}{\partial x}\left(\mu_e\frac{\partial u_0}{\partial r}\right) + \rho_0\frac{w_0^2}{r} - \frac{2}{3}\frac{\partial}{\partial r}\left(\rho_0 k\right) \end{aligned} \tag{3.14}$$

$$S\left(w_0\right) = -\frac{\rho_0 v_0 w_0}{r} - \frac{w_0}{r^2}\frac{\partial}{\partial r}\left(r\mu_e\right) \tag{3.15}$$

3. First-Order Equations

Continuity equation in complex function form:

$$\begin{aligned} \frac{\partial}{\partial x}\left(\rho_0\hat{u}_1\right) + \frac{1}{r}\frac{\partial}{\partial r}\left(r\rho_0\hat{v}_1\right) = &-\frac{\partial}{\partial x}\left(\hat{\rho}_1 u_0\right) - \frac{1}{r}\frac{\partial}{\partial r}\left(r\hat{\rho}_1 v_0\right) \\ &+ \mathbf{j}\left\{\frac{1}{r}\left(\rho_0\hat{w}_1 + \hat{\rho}_1 w_0\right) - \hat{\rho}_1\Omega\right\} \end{aligned} \tag{3.16}$$

General momentum equation in complex function form:

$$\frac{\partial}{\partial x}\left(\rho_0 u_0\hat{\Phi}_1\right) + \frac{1}{r}\frac{\partial}{\partial r}\left(r\rho_0 v_0\hat{\Phi}_1\right) = \frac{\partial}{\partial x}\left(\mu_e\frac{\partial\hat{\Phi}_1}{\partial x}\right) + \frac{1}{r}\frac{\partial}{\partial r}\left(r\mu_e\frac{\partial\hat{\Phi}_1}{\partial r}\right) + S\left(\hat{\Phi}_1\right) \tag{3.17}$$

Where the source terms for each variable are given as:

$$\begin{aligned} S\left(\hat{u}_1\right) = &-\frac{\partial\hat{p}_1}{\partial x} + \frac{1}{3}\frac{\partial}{\partial x}\left(\mu_e\frac{\partial\hat{u}_1}{\partial x}\right) + \frac{1}{r}\frac{\partial}{\partial r}\left(r\mu_e\frac{\partial\hat{v}_1}{\partial x}\right) - \rho_0\left[\hat{v}_1\frac{\partial u_0}{\partial r} + \hat{u}_1\frac{\partial u_0}{\partial x}\right] \\ &- \mu_e\frac{\hat{u}_1}{r^2} - \hat{\rho}_1\left[v_0\frac{\partial u_0}{\partial r} + u_0\frac{\partial u_0}{\partial x}\right] - \frac{2}{3}\frac{\partial}{\partial x}\left[\mu_e\left(\frac{\partial\hat{v}_1}{\partial r} + \frac{\hat{v}_1}{r}\right) + \hat{\rho}_1 k\right] \\ &- \mathbf{j}\left\{\frac{\mu_e}{r}\frac{\partial\hat{w}_1}{\partial x} - \frac{2}{3}\frac{1}{r}\frac{\partial}{\partial x}\left(\mu_e\hat{w}_1\right) - \rho_0\frac{w_0\hat{u}_1}{r} + \rho_0\Omega\hat{u}_1\right\} \end{aligned} \tag{3.18}$$

$$
\begin{aligned}
S\left(\hat{v}_1\right) = &- \frac{\partial \hat{p}_1}{\partial r} + \frac{1}{3}\frac{\partial}{\partial r}\left(\mu_e \frac{\partial \hat{v}_1}{\partial r}\right) + \frac{\partial}{\partial x}\left(\mu_e \frac{\partial \hat{u}_1}{\partial r}\right) - \frac{7}{3}\mu_e \frac{\hat{v}_1}{r^2} \\
&- \frac{2}{3}\frac{1}{r}\frac{\partial}{\partial r}\left(\mu_e \hat{v}_1\right) + \frac{1}{3}\frac{\mu_e}{r}\frac{\partial \hat{v}_1}{\partial r} - \frac{2}{3}\frac{\partial}{\partial r}\left(\mu_e \frac{\partial \hat{u}_1}{\partial x} + \hat{\rho}_1 k\right) \\
&- \rho_0 \left[\hat{v}_1 \frac{\partial v_0}{\partial r} - 2\frac{w_0 \hat{w}_1}{r} + \hat{u}_1 \frac{\partial v_0}{\partial x}\right] - \hat{\rho}_1 \left[v_0 \frac{\partial v_0}{\partial r} - \frac{w_0^2}{r} + u_0 \frac{\partial v_0}{\partial x}\right] \\
&- \mathbf{j}\left\{\frac{\mu_e}{r}\frac{\partial \hat{w}_1}{\partial r} - \frac{2}{3}\frac{1}{r}\frac{\partial}{\partial r}\left(\mu_e \hat{w}_1\right) - \frac{7}{3}\frac{\mu_e \hat{w}_1}{r^2} - \rho_0 \frac{w_0 \hat{v}_1}{r} + \rho_0 \Omega \hat{v}_1\right\}
\end{aligned}
\tag{3.19}
$$

$$
\begin{aligned}
S\left(\hat{w}_1\right) = &- \frac{7}{3}\mu_e \frac{\hat{w}_1}{r^2} - \frac{\hat{w}_1}{r}\frac{\partial \mu_e}{\partial r} - \rho_0 \left[\hat{v}_1 \frac{\partial w_0}{\partial r} + \frac{v_0 \hat{w}_1}{r} + \frac{w_0 \hat{v}_1}{r} + \hat{u}_1 \frac{\partial w_0}{\partial x}\right] \\
&- \hat{\rho}_1 \left[v_0 \frac{\partial w_0}{\partial r} + \frac{v_0 w_0}{r} + u_0 \frac{\partial w_0}{\partial x}\right] - \mathbf{j}\left\{-\frac{\hat{p}_1}{r} + \frac{7}{3}\frac{\mu_e \hat{v}_1}{r^2} + \frac{\hat{v}_1}{r}\frac{\partial \mu_e}{\partial r}\right. \\
&\left. + \frac{1}{3}\frac{\mu_e}{r}\frac{\partial \hat{v}_1}{\partial r} - \frac{2}{3}\frac{\mu_e}{r}\frac{\partial \hat{u}_1}{\partial x} + \frac{1}{r}\frac{\partial}{\partial x}\left(\mu_e \hat{u}_1\right) - \frac{2}{3}\frac{\hat{\rho}_1 k}{r} - \frac{\rho_0 w_0 \hat{w}_1}{r} + \rho_0 \Omega \hat{w}_1\right\}
\end{aligned}
\tag{3.20}
$$

The perturbed governing equations for the zeroth- and first-order variables were solved using a finite-volume computer code utilizing the SIMPLEC algorithm with the QUICK differencing scheme for the convection terms.

B. Boundary Conditions

Previous quasi-3D rotordynamic seal models employed a perturbation coordinate transformation in deriving the first-order governing equations and boundary conditions to align the displaced rotor surface (Fig. 3) with a grid line in the transformed plane ([6] and [30]). This approach introduced considerable complications, including a large increase of first-order source terms in the governing equations. The present approach, as discussed by Kim and Rhode [7], avoids these complications by utilizing a Taylor series expansion in the radial direction to approximate the first-order variables on the displaced rotor surface in terms of those on the concentric rotor surface. This allows the non-displaced rotor surface to be used as the domain rotor boundary for both the zero- and first-order solutions.

The first-order boundary values on the stator wall were specified as zero, and those on the rotor were taken from standard dynamics relations that account for rotor displacement, whirl and shaft speed. Details can be found in a work by Kim and Rhode [7] and Kim et al. [25]. At the domain exit, the axial gradient of the first-order velocity components was assumed to be zero. Further, the Dirichlet boundary condition for the disturbance pressure was specified using the perturbed Bernoulli (*i.e.* bulk energy) equation applied between the seal exit and the downstream chamber; see Eq. (3.21):

$$\hat{p}_1\left(x_{ex}\right) = -p_{dn}\left(1-\xi_{ex}\right)\left[\frac{u_0\left(x_{ex}\right)\hat{u}_1\left(x_{ex}\right)+w_0\left(x_{ex}\right)\hat{w}_1\left(x_{ex}\right)}{\gamma R T_{ex}}\right] \tag{3.21}$$

where the subscript ex signifies the condition at the seal exit while dn signifies the downstream chamber condition. The minor loss coefficient ξ_{ex} can be in the range from 0.9 to 1.1. A value of 1.0 is used in the present study.

C. Rotordynamic Coefficients

The resulting radial and tangential force components, F_r and F_t, acting upon the whirling rotor can be obtained by integrating the disturbance pressures along the length of the rotor surface, as shown in Eqs. (3.22) and (3.23),

$$-\frac{F_r}{e} = \pi\int\limits_L \left.\frac{dP_0\left(x,r\right)}{dr}\right|_{R^*} R^* dx + \frac{\pi}{C_r}\int\limits_L P_{1C}\left(x,R^*\right)R^* dx \tag{3.22}$$

$$-\frac{F_t}{e} = \frac{\pi}{C_r}\int\limits_L P_{1S}\left(x,R^*\right)R^* dx \tag{3.23}$$

The relations between the radial and tangential force components and the corresponding rotordynamic force coefficients are expressed as Eqs. (3.24) and (3.25),

$$-\frac{F_r}{e} = K + c\Omega - M\Omega^2 \tag{3.24}$$

$$-\frac{F_t}{e} = -k + C\Omega + m\Omega^2 \tag{3.25}$$

By using the above relations and least square curve fitting in terms of the whirling speed, one can obtain the rotordynamic force coefficients for different flow conditions. Usually, the the inertial coefficients are negligible in comparison with stiffness and damping coefficients in seals. Therefore, Eq. (3.25) reduces to:

$$-\frac{F_t}{e} = \left[C - \frac{k}{\Omega}\right]\Omega \tag{3.26}$$

where the effective damping C_{eff} can be defined as $C_{eff} = C - k/\Omega$, which incorporates the typically destabilizing k and the stabilizing C. A positive effective damping is the net stabilizing (resisting whirl) tangential force acting on the rotor per unit rotor displacement and per unit whirl frequency. In this research, sub-synchronous vibration with Ω equal to 0.5ω was assumed in evaluating C_{eff}.

CHAPTER IV

DEVELOPMENT OF SEAL-INLET DISTURBANCE BOUNDARY CONDITION CORRELATIONS

A. Introduction

One of the objectives of the present study is to develop seal inlet flow disturbance boundary conditions with broad applicability. Achieving this goal requires a better understanding of the fluid dynamics at the seal inlet, *i.e.* how the force impedances are influenced by the flow disturbance variables and how the seal configuration and operating condition influence these disturbance variables. A thorough parametric study was performed corresponding to this requirement. New physical insights were gained about the relation between flow disturbance variables and operating conditions.

B. Parametric Studies

The seal configurations considered in the present study can be divided into two classes according to their up-chambers: (a) seals with axial-inlet upstream chambers and (b) seals with radial injection up-chambers, as illustrated in Fig 4 (a) and (b), respectively. The CFD perturbation code was used to compute the flow disturbance quantities assuming zero disturbance at the domain inlet (location 1 in Fig. 4 (a) or location 4 in Fig. 4 (b)). This assumption is justified for two reasons. First, because the domain inlet is far away from the rotor where the disturbance originates, the disturbance quantities at the domain inlet are negligible. Secondly, whatever disturbance exists at the inlet is diffused and dampened by the large up-chamber.

Operating condition ranges are shown in Table I. For seals with the axial-inlet up-chamber, CFD solutions at location 2 in Fig. 4 (a) (location 5 in Fig. 4 (b) if

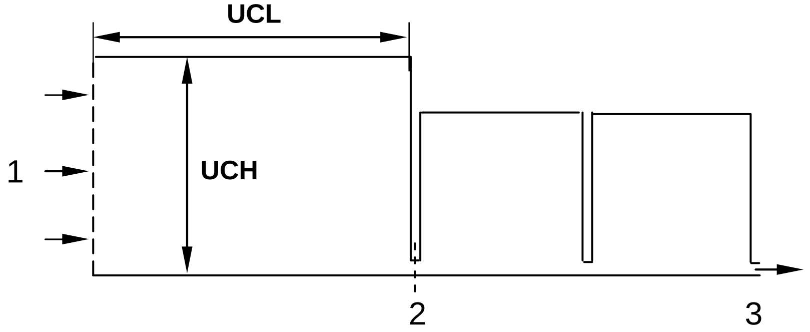

(a) Labyrinth seal with axial-inlet upstream chamber

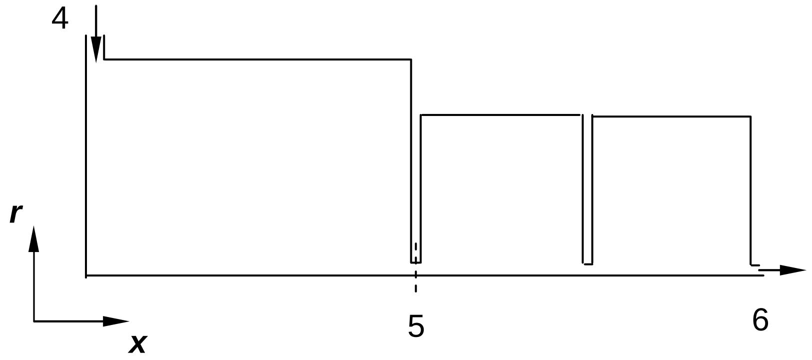

(b) Labyrinth seal with radial-injection chamber

Fig. 4. Overall seal configuration with up-chamber: (a) with axial inlet upstream chamber; (b) with radial injection chamber.

Table I. Geometry and Operating Condition Range of the Parametric Study Cases

Geometries				Operating Conditions			
C_r (mm)	R_{sh} (mm)	$\frac{UCL}{C_r}$	M	W_0 (m/s)	P_0 (bar)	ω ($10^3 rpm$)	$\frac{\Omega}{\omega}$
0.12∼0.4	50∼152	10∼150	0.1∼0.3	-100∼250	10∼70	4∼20	0∼0.75

Table II. Grid Independence Testing Results

NI×NJ	Δy within C_r (mm)	K (MN/m)	$\frac{(K_c - K_f)}{K_f}$ (%)	k (MN/m)	$\frac{(k_c - k_f)}{k_f}$ (%)	C (KNs/m)	$\frac{(C_c - C_f)}{C_f}$ (%)
126×47	0.0381	-0.111	−−	0.322	−−	0.459	−−
175×61	0.0254	-0.106	4.62	0.332	-3.16	0.472	-2.72
230×80	0.0191	-0.104	2.47	0.340	-2.36	0.479	-1.57

with radial-injection chamber) give the values that were obtained in this study for the previously unavailable seal inlet boundary condition values. A very large number of operating conditions were computed, and the seal inlet solution values of each were tabulated in order to determine the inlet boundary condition correlations.

1. Grid Independence Testing

Grid independence testing was performed with a seal inlet axial Mach number M of 0.15, a spin speed ω of 8640 rpm and an inlet swirl velocity of 60 m/s. The geometric layout and dimensions were given by Fig. 4 and Table I. Three grids were utilized with control cells inside the tooth clearance of 0.0381 mm × 0.0381 mm (coarse grid), 0.0254 mm × 0.0254 mm (production grid) and 0.0191 mm × 0.0191 mm (fine grid), respectively. The deviation of the computed force coefficients from these three grids is very small. The coarse grid gave solutions with less than 4.62% deviation from the production grid and the production grid gave solutions with less than 2.47% deviation from the fine grid (see Table II).

The seal inlet radial profiles of the axial and swirl velocity disturbance variables from different grids are shown in Fig. 5 and Fig 6. The deviation from different grids is very small. As is observed from Fig. 6 (a), the seal inlet W_{1C} has a steep radial profile.

2. Effect of Disturbance Variables on Force Coefficients

Parametric studies were performed to determine the impact of varying disturbance quantities on the force coefficients. The test case geometry was a two-cavity seal as shown in Fig 4 (a) from location 2 to 3 with $C_r = 0.254$ mm, $R_{sh} = 64.69$ mm and $L = 6.35$ mm. The operating conditions were as follows: a shaft spin speed of 4680 rpm, an inlet swirl of -26.57 m/s and up- and down-stream pressures of 13.77 and 11.7 bar, respectively. The results show that the cross-coupled stiffness k is influenced in the order of importance by W_{1C}, U_{1S}, P_{1S}, W_{1S}, U_{1C} and P_{1C} at the seal inlet. The effects of W_{1C}, U_{1C}, and U_{1S} are shown in Figs. 7 to 9. The effects of seal inlet U_{1C} and P_{1C} are negligible compared to other parameters.

a. W_{1C} Radial Profile *vs.* Flat Bulk Value

For a given magnitude, the W_{1C} inlet radial profile, when compared with the W_{1C} bulk-averaged flat profile, gives about a 33% increase of the cross-coupled stiffness k (see Fig. 7). Further, W_{1C} magnitude at the seal inlet is found to have a surprisingly large effect on the cross-coupled stiffness k. In previous models (Bulk flow models, 3-D CFD models, and CFD perturbation models), W_{1C} has always been assumed to be zero because of the lack of information about this disturbance variable. This assumption will apparently cause consequential errors in the prediction of k, and presumably K and C as well.

Based on the current CFD results from the zeroth-order, *i.e.* concentric-rotor model, the W_{1C} inlet radial profile is much more realistic than the flat profile. For 3-D CFD models and CFD-perturbation models, the W_{1C} radial profile is recommended

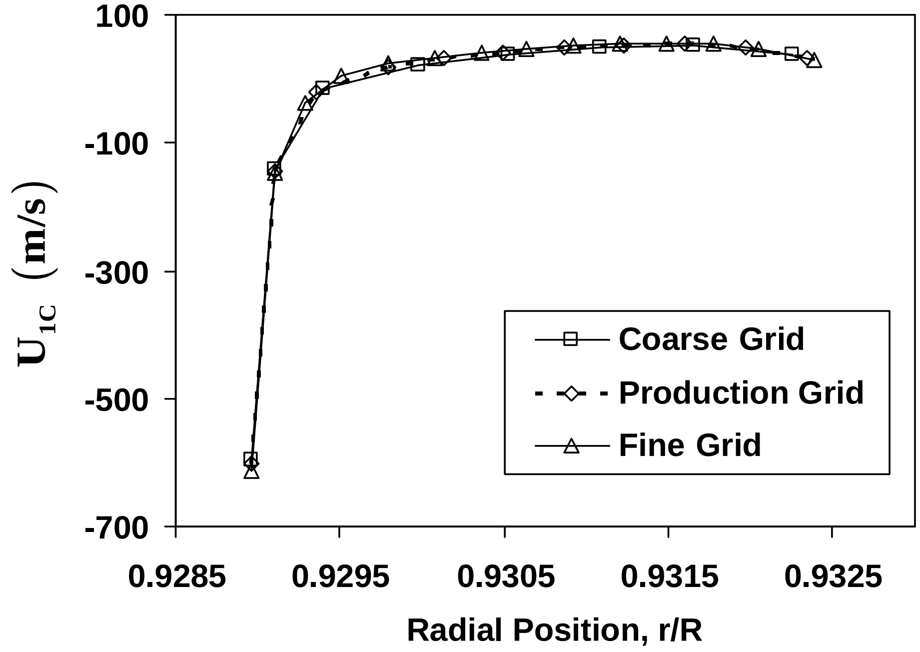

(a) Cosine Component

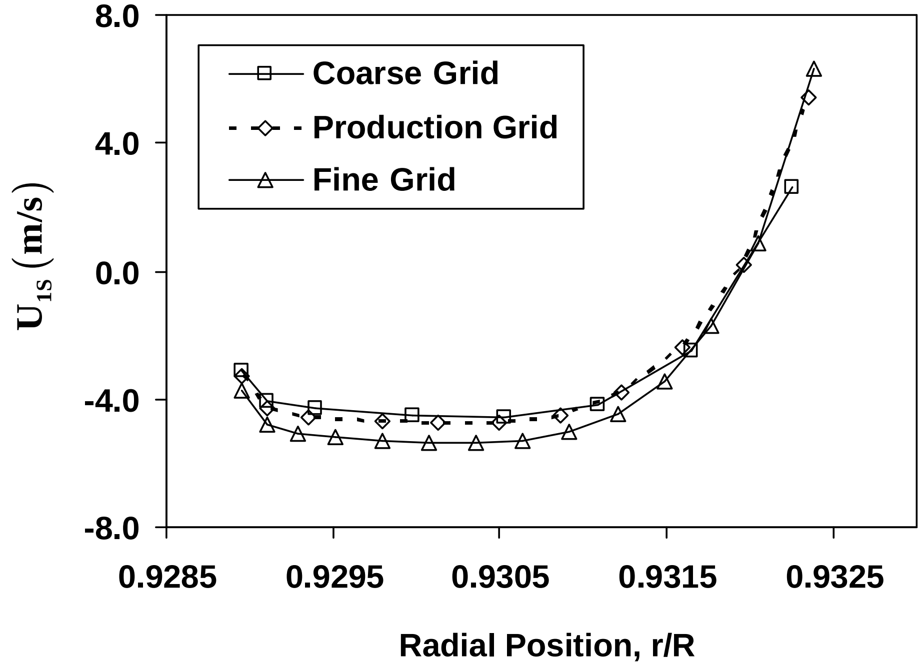

(b) Sine Component

Fig. 5. Seal inlet disturbance axial velocity: (a) cosine component and (b) sine component.

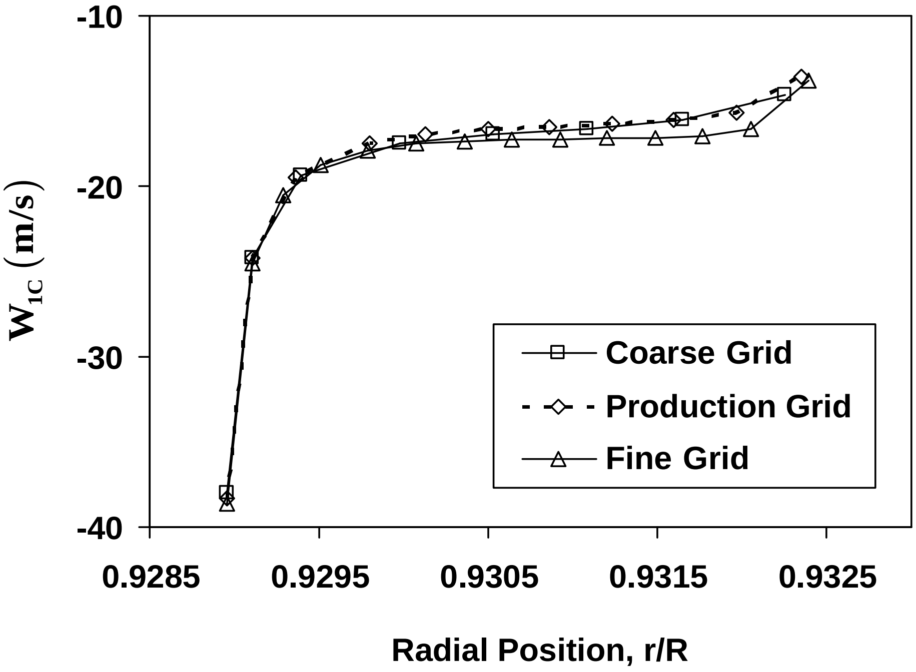

(a) Cosine Component

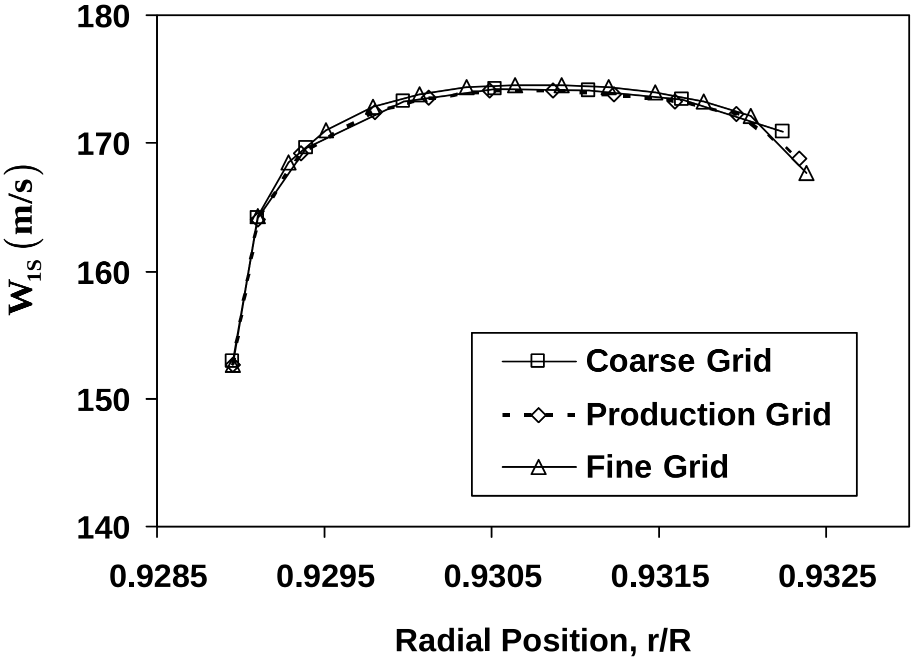

(b) Sine Component

Fig. 6. Seal inlet disturbance swirl velocity: (a) cosine component and (b) sine component.

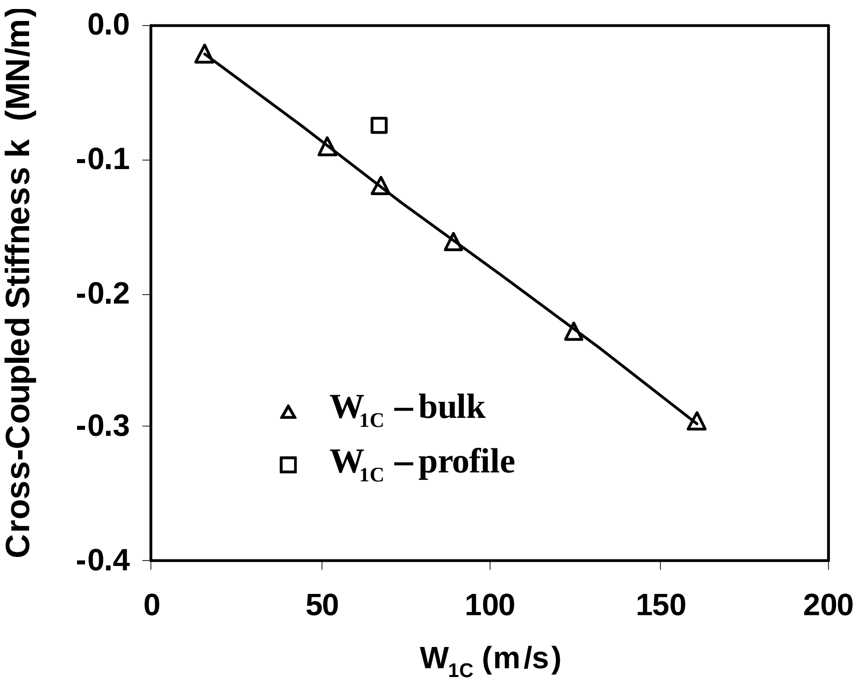

Fig. 7. Surprisingly large effect of the seal inlet cosine component of the swirl velocity disturbance on cross-coupled stiffness k.

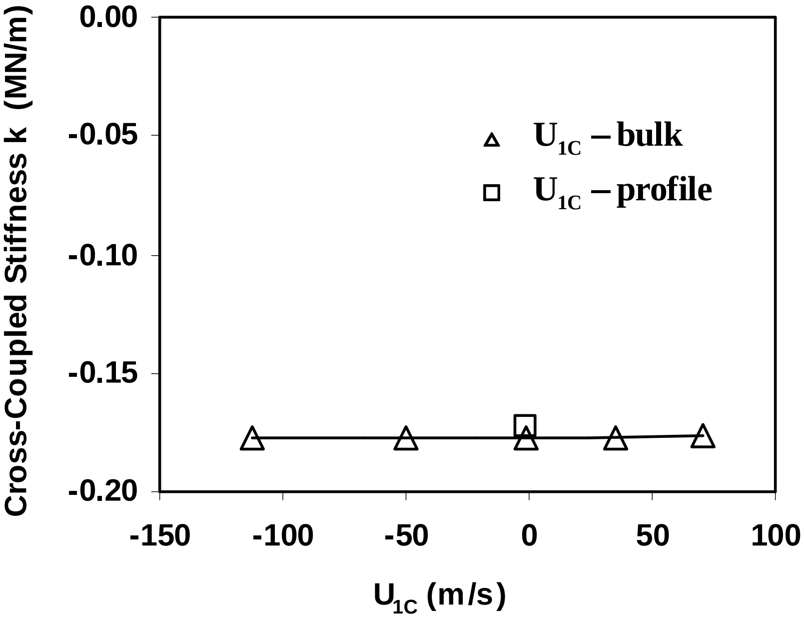

(a) Cross-coupled stiffness

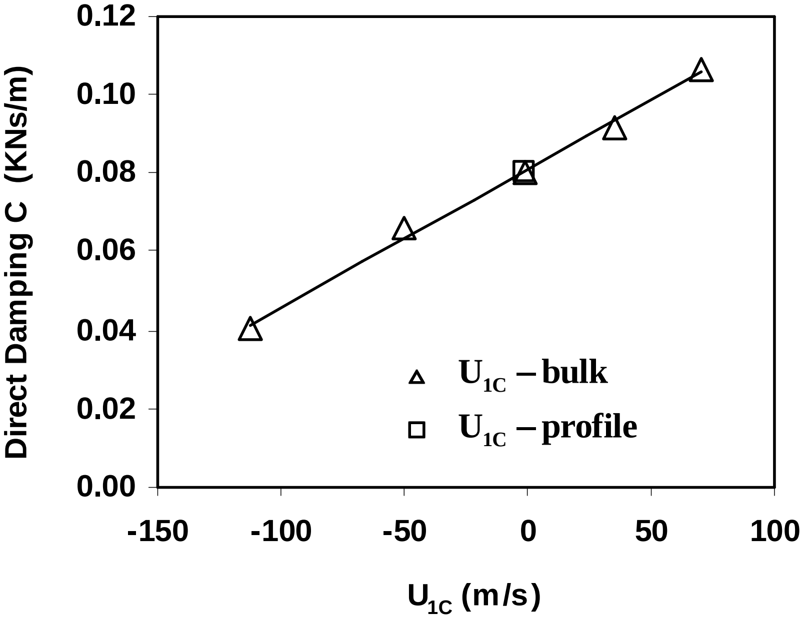

(b) Direct damping

Fig. 8. Influence of the seal inlet cosine component of the streamwise velocity disturbance magnitude (bulk and radial profile) on force coefficients: (a) cross-coupled stiffness; (b) direct damping.

as the seal inlet boundary condition. The bulk profile, which is required by the bulk flow models, still gives a reasonable prediction in this test case (see Fig. 7).

b. Other Disturbance Variables

The cosine component of the axial disturbance velocity U_{1C} at the seal inlet gives a negligible effect on k while having a considerable effect on the direct damping C, which increases as U_{1C} becomes more positive (see Fig. 8). Since the tangential force is the combination of the cross-coupled stiffness and direct damping effects, the seal inlet U_{1C} is expected to have a significant effect on rotordynamic stability.

The U_{1S} magnitude at the seal inlet has a fairly large effect on the cross-coupled stiffness k as shown in Fig 9, and only a slight effect on the direct damping C. Specifically, k decreases as U_{1S} becomes more positive. Further, it was found that U_{1S} is not a major concern in the present study because its magnitude is usually significantly smaller than that of W_{1C} as well as U_{1C} in the operating condition range as shown in Table I.

In addition, it was found that P_{1C} and P_{1S} at the seal inlet have only a slight effect on k and C.

3. Effect of Geometry and Operating Conditions on Disturbance Variables

It has long been recognized that geometry and operating condition have a large influence on the flow disturbance quantities at the seal inlet. Furthermore, the effect of each geometry or operating condition quantity will be different on each flow disturbance variable. Despite its potential to further illuminate the mechanism of seal rotordynamics, no parametric study has been reported concerning the effect of geometry and operating condition, either experimentally or numerically, on the disturbance boundary conditions for the seal inlet. The present study was motivated by this lack

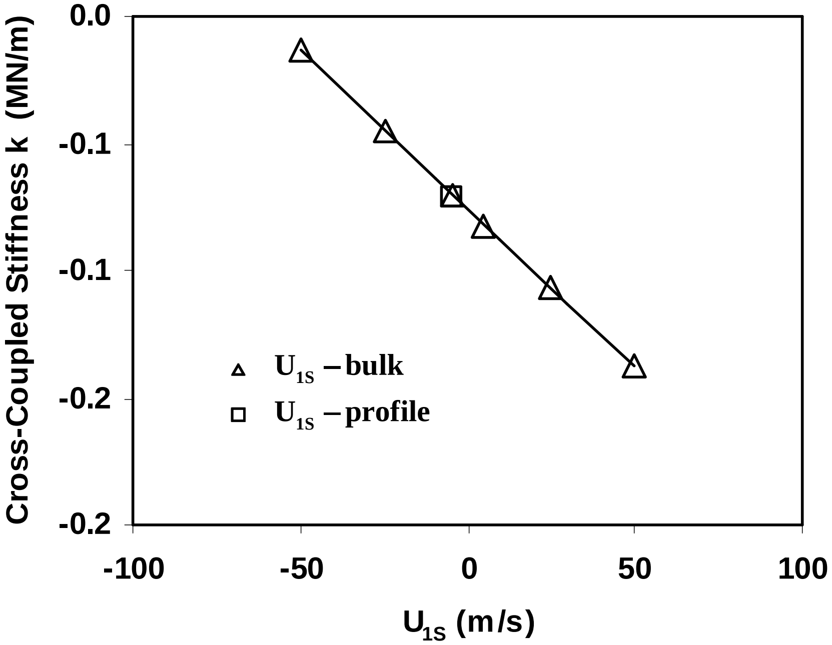

Fig. 9. Influence of the seal inlet sine component of the streamwise velocity disturbance magnitude (bulk and radial profile) on cross-coupled stiffness k.

of information.

a. Numerical Considerations

Thorough parametric studies were conducted to investigate the impact of geometry and operating condition quantities on the flow disturbance variables. The geometries and operating conditions were selected to cover a wide range of seals. The range considered is indicated in Table I.

(1) Geometry

Because the seal clearance was assumed to have a large effect on the disturbance variables, three radial clearances were selected: 0.127 mm, 0.254 mm and 0.381 mm. From past experiences, both the shape and the size of the upstream chamber were found to have a fairly significant effect on dynamic coefficients, especially on direct

Table III. Order of Importance of Variables Affecting Seal Inlet Flow Disturbance Quantities

1	$\bar{W}_{1C} = f\left(\left(\omega R_{sh} - \bar{W}_0\right), C_r, \bar{P}_0, UCL, UCH, \Omega, ...\right)$	Independent of $\bar{U}_0$
2	$\bar{W}_{1S} = f\left(C_r, \bar{U}_0, UCL, UCH, R_{sh}, \Omega, ...\right)$	Independent of $\bar{W}_0$
3	$\bar{U}_{1C} = f\left(\bar{U}_0, \bar{W}_0, C_r, \Omega, ...\right)$	
4	$\bar{U}_{1S} = f\left(\left(\omega R_{sh} - \bar{W}_0\right), C_r, \bar{U}_0, ...\right)$	
5	$\bar{P}_{1C} = f\left(\bar{U}_0, \bar{W}_0, \bar{P}_0, C_r, \Omega, ...\right)$	
6	$\bar{P}_{1S} = f\left(\left(\omega R_{sh} - \bar{W}_0\right), \bar{U}_0, \bar{P}_0, \Omega, ...\right)$	

stiffness. To investigate the effect of the upstream chamber, two types of chamber were considered here: axial inlet chamber and radial injection chamber. The upstream chamber length *UCL* and height *UCH* ranged from 10∼150 times the clearance and 10∼30 times the clearance, respectively.

(2) Operating Condition

The effect of seal inlet swirl was the main focus of the present study. A very wide range of W_0 was considered which ranged from -100m/s to 250 m/s, covering almost all applications of industrial seals. The spin speeds ranged from 4,000 to 20,000 rpm. The shaft radius ranged from 50.8 mm to 152.4 mm.

The Mach number of the streamwise velocity at the seal inlet varied from about 0.1 to 0.3. The upstream pressure had a range from 10 bar to 70 bar. These two variables are directly associated with the seal leakage and served as two indicators of the relationship between leakage and the force coefficients.

b. Results and Discussion

A summary of some of the results of the parametric study are listed in Table III. Here, the order of importance of variables that affect each inlet flow disturbance quantity is given. The order of importance was determined by the absolute magnitude of the exponent 'a' in a power-curve-fitted equation $y = x^a$. In this study, 'y' was one dependent disturbance quantity and 'x' was one configuration or operating condition variable.

(1) Swirl Disturbance Cosine Component, $\bar{W}_{1C}$

The swirl disturbance cosine component $\bar{W}_{1C}$ at the seal inlet was found to be affected, in descending order of importance, by $(\omega R_{sh} - \bar{W}_0)$, clearance C_r, pressure $\bar{P}$, upstream chamber length *UCL* and height *UCH*, and whirling speed Ω. Additionally, the seal inlet $\bar{W}_{1C}$ showed negligible dependence on $\bar{U}_0$.

Before this study, the zeroth-order swirl velocity at the seal-inlet $\bar{W}_0$, as well as the peripheral speed ωR_{sh}, was known to have a significant effect on k. As the result of the current systematic parametric study, it was determined that seal-inlet W_{1C} also has a large effect on k. It was further found that W_{1C} depends primarily on only W_0 and ωR_{sh}, although Table III shows that C_r, P_0, *UCL, UCH* and Ω also play a role. Using this new finding, it was learned that the precision of the relationship between W_{1C} and W_0 (see Fig. 10 (a)) could be greatly improved by instead relating W_{1C} to the swirl slip velocity $(\omega R_{sh} - \bar{W}_0)$ (see Fig. 10 (b)). In addition, Fig. 10 (b) shows that this improved relationship is very nicely correlated by a simple linear function.

Next, because W_{1C} was found to be the seal-inlet flow disturbance quantity exerting the largest effect on k, it was decided to try to improve the relationship between k and W_0 by relating k to the swirl slip velocity $(\omega R_{sh} - \bar{W}_0)$. Comparison of Figs. 11 (a) and 11 (b) show that the use of the seal-inlet swirl slip velocity also

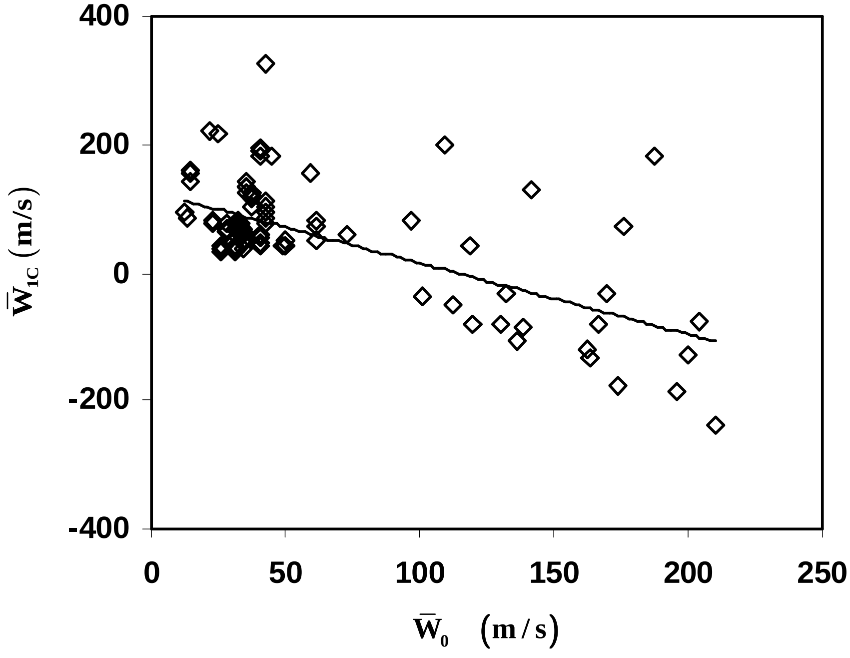

(a) Plotting $\bar{W}_{1C}$ against $\bar{W}_0$

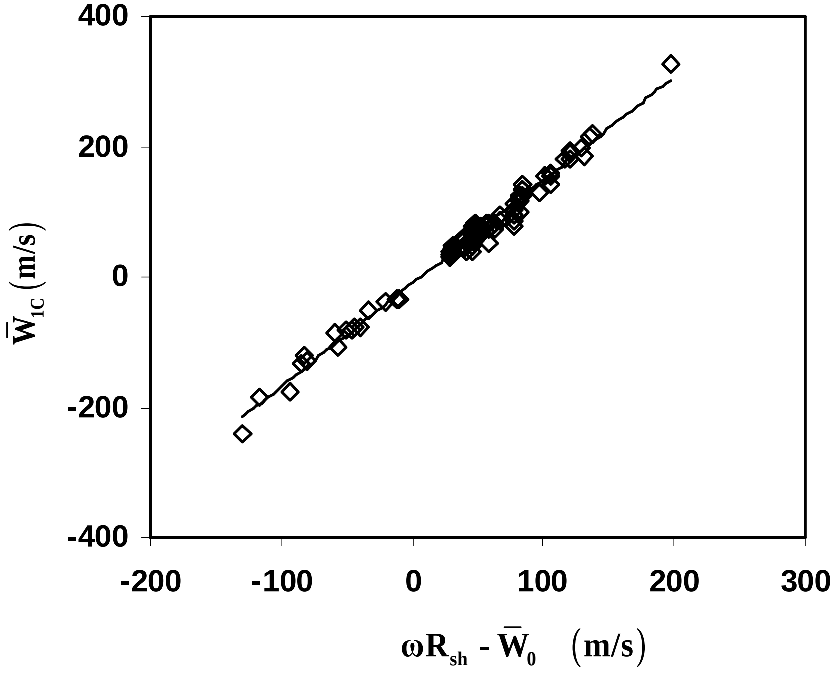

(b) Plotting $\bar{W}_{1C}$ against $[\omega R_{sh} - \bar{W}_0]$

Fig. 10. More precise relation between seal-inlet $\bar{W}_{1C}$ and $\bar{W}_0$ from plotting $\bar{W}_{1C}$ against the seal-inlet swirl slip $[\omega R_{sh} - \bar{W}_0]$ as shown in Fig. 10 (b).

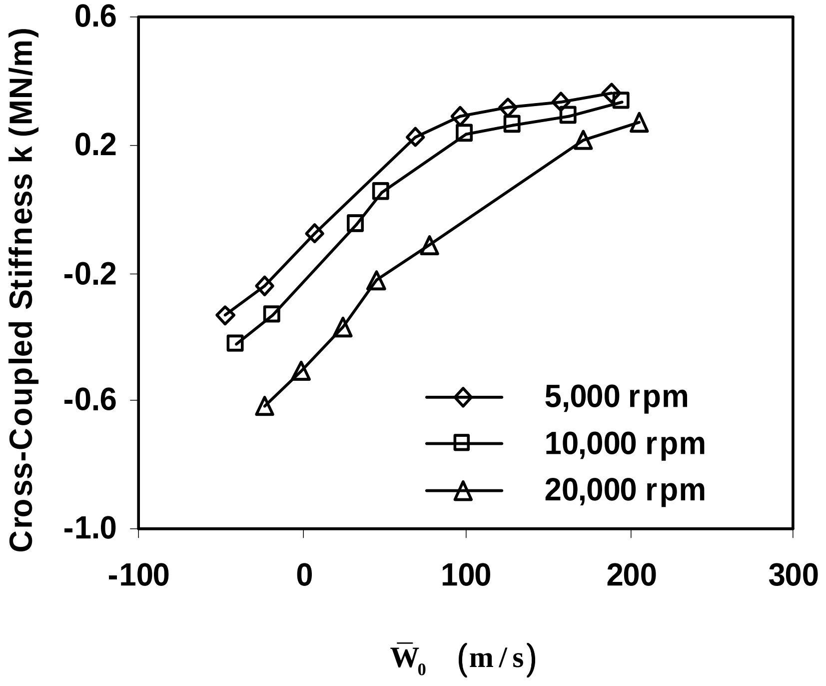

(a) Plotting k against $\bar{W}_0$

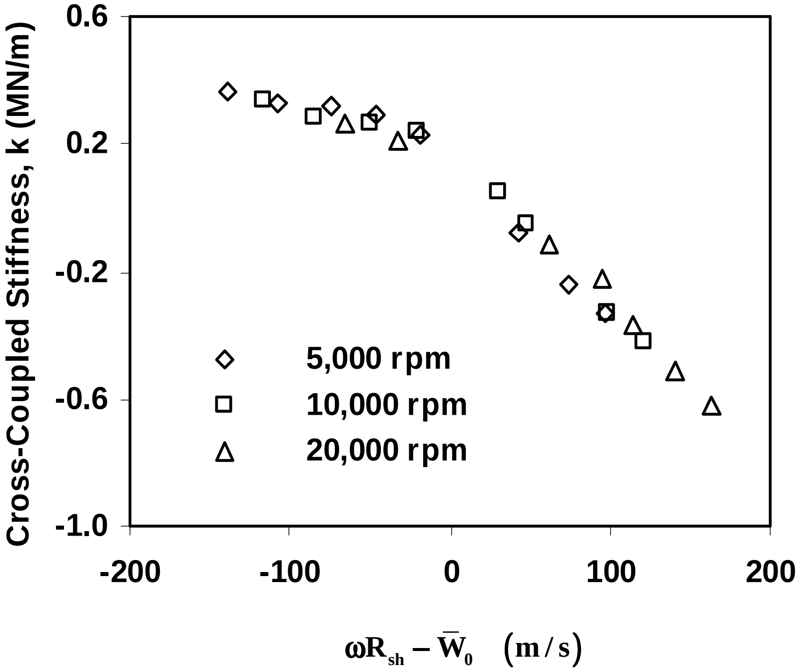

(b) Plotting k against $[\omega R_{sh} - \bar{W}_0]$

Fig. 11. More precise relation between cross-coupled stiffness k and $\bar{W}_0$ from plotting k against the seal-inlet swirl slip $[\omega R_{sh} - \bar{W}_0]$ as shown in Fig. 11 (b).

gives a major improvement in the precision of the relationship between k and W_0.

The influence of seal clearance C_r on $\bar{W}_{1C}$ is minor compared with that of the swirl "slip". The impact exponent of the clearance on $\bar{W}_{1C}$ is 0.288, while that of the swirl "slip" is 1.0. Moreover, $\bar{W}_{1C}$ is almost independent of the leakage ($\bar{U_0}$) (the impact exponent of $\bar{U_0}$ on $\bar{W}_{1C}$ is 0.02).

(2) Swirl Disturbance Sine Component, $\bar{W}_{1S}$

The sine component of the swirl disturbance $\bar{W}_{1S}$ depends, in descending order of importance, upon C_r, $\bar{U_0}$, *UCL, UCH*, R_{sh} and Ω. It was also found that $\bar{W}_{1S}$ is almost independent of inlet swirl velocity $\bar{W}_0$, which has an impact exponent of -0.0626 on $\bar{W}_{1S}$.

The streamwise velocity $\bar{U_0}$ at the seal inlet has a considerable effect on $\bar{W}_{1S}$, with an impact exponent of 0.847, as exhibited in Fig. 12. $\bar{W}_{1S}$ increases nearly linearly as $\bar{U_0}$ increases.

The seal clearance is found to have an essentially linear relation with $\bar{W}_{1S}$ with an impact exponent of 0.959. Increasing C_r while keeping the axial velocity $\bar{U_0}$ constant at the seal inlet will linearly increase $\bar{W}_{1S}$.

The influence of upstream chamber size/shape on $\bar{W}_{1S}$ is illustrated in Fig. 13 which was obtained by varying *UCL, UCH* and C_r respectively. The effect of each quantity on $\bar{W}_{1S}$ was evaluated separately. For large axial-inlet upstream chambers, a longer (large *UCL*) and taller (large *UCH*) chamber will result in a smaller $\bar{W}_{1S}$. The impact exponents of *UCL* and *UCH* were found to be -0.884 and -0.667, respectively. The relationship of the sine swirl disturbance ($\bar{W}_{1S}/\bar{U_0}$) with dimensionless upstream chamber size in Fig 13 has two parts. The left-hand part represents large axial-inlet upstream chambers, while the right-hand part represents small axial-inlet chambers

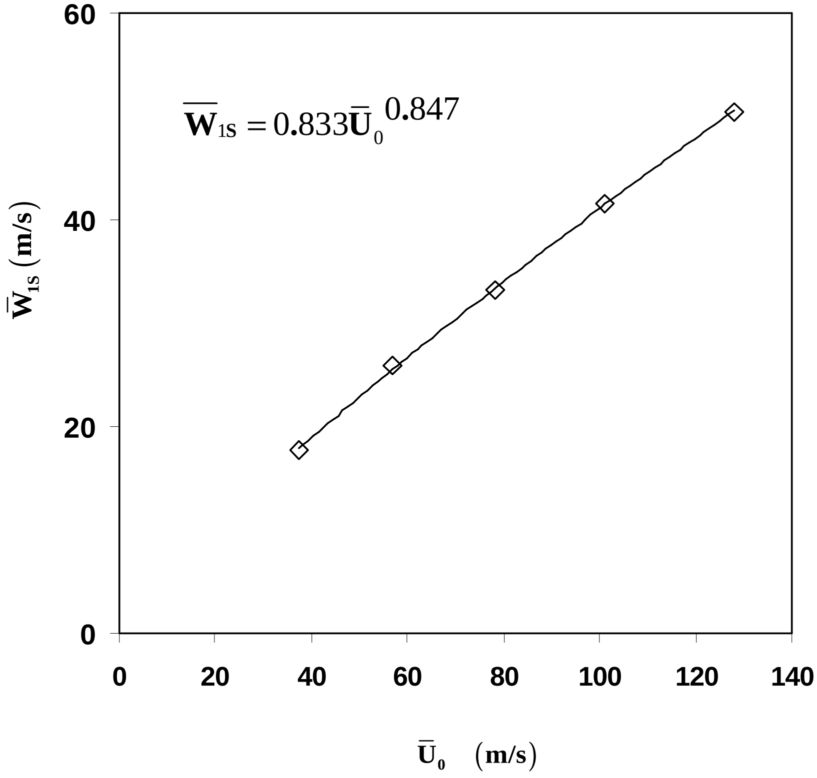

Fig. 12. Effect of seal inlet streamwise velocity $\bar{U}_0$ has a substantial effect on disturbance swirl velocity sine component at the seal inlet, with an impact exponent of 0.847.

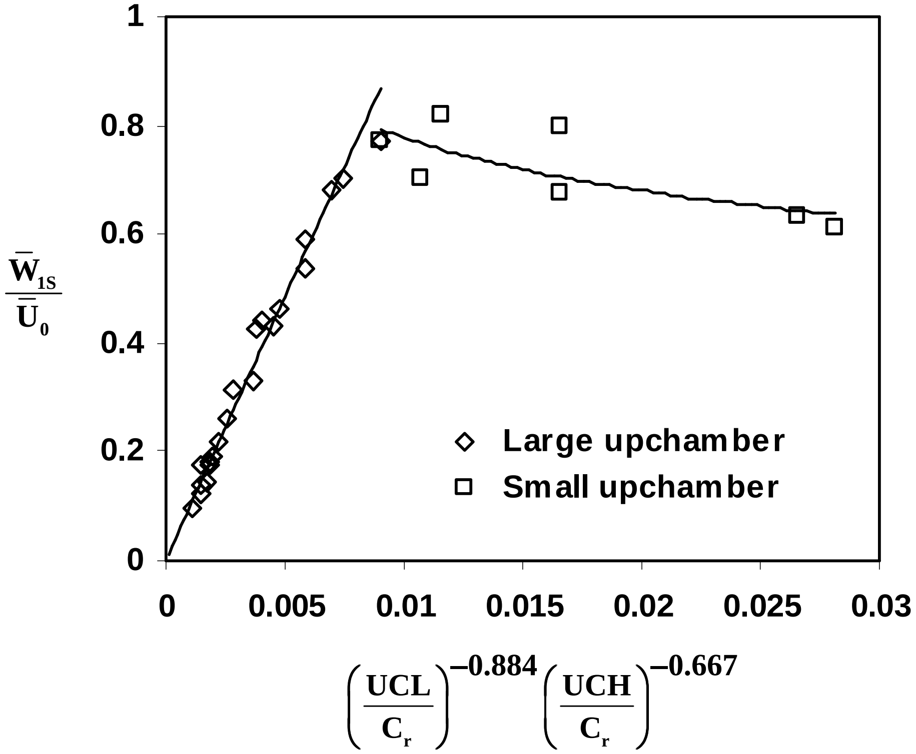

Fig. 13. Variation of dimensionless swirl disturbance velocity (sine) with upstream chamber size. The dividing point for "large" and "small" upstream chamber is $\left(\frac{\mathrm{UCL}}{\mathrm{C_r}}\right)^{-0.884}\left(\frac{\mathrm{UCH}}{\mathrm{C_r}}\right)^{-0.667} = 0.008$.

and radial-injection chambers. The dividing point was determined to be,

$$\left(\frac{UCL}{C_r}\right)\left(\frac{UCH}{C_r}\right) = 400 \tag{4.1}$$

The abscissa in Fig. 13 has already taken into account the impact exponents of UCL and UCH so that $(\bar{W}_{1S}/\bar{U}_0)$ exhibits a linear relation. For small axial-inlet upstream chambers, the slope of the $\bar{W}_{1S}$ curve is somewhat flat, indicating a minor impact of chamber size on $\bar{W}_{1S}$. Further, the shaft radius also plays a substantial role on $\bar{W}_{1S}$, with an impact exponent of 0.731.

$\bar{W}_{1S}$ at the seal inlet has a significant effect on $\bar{P}_{1C}$ along the rotor surface, whose integration gives the radial force exerted on the rotor surface. Therefore it is deduced that the upstream chamber size/shape has a considerable effect on the radial force via the considerable effect on $\bar{W}_{1S}$.

Since $\bar{W}_{1S}$ shows a significant dependence on $\bar{U}_0$ and only minor dependence on $\bar{W}_0$, it is suggested that the direct stiffness K has a close relationship with seal leakage while having essentially no relationship with the inlet swirl velocity.

Upstream chamber size/shape was also found to have certain effects on other flow disturbance variables, and the effect can not be expressed by one single relation. Accordingly, two groups of correlations were developed in the present study with one for large axial-inlet chambers and the other for small axial-inlet as well as radial-injection up-chambers.

(3) Axial Velocity Disturbance Cosine Component, $\bar{U}_{1C}$

$\bar{U}_{1C}$ at the seal inlet has a steep radial profile with a positive value near the tooth tip and a negative value near the rotor surface. Its effect on the force coefficients is summarized in Section $IV.B.2$. The seal inlet $\bar{U}_{1C}$ is determined, in descending order of importance, by $\bar{U}_0$, $\bar{W}_0$, C_r and Ω. Figure 14 shows the effect of $\bar{U}_0$ on the U_{1C} radial profile and a linear relationship exists between them.

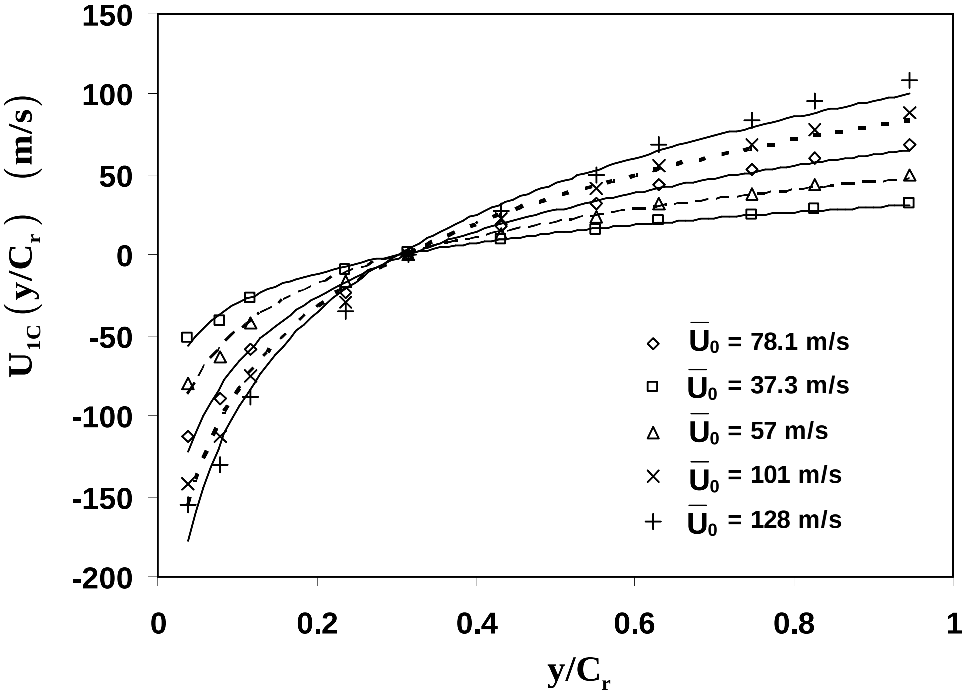

(a)U_{1C} radial Profile

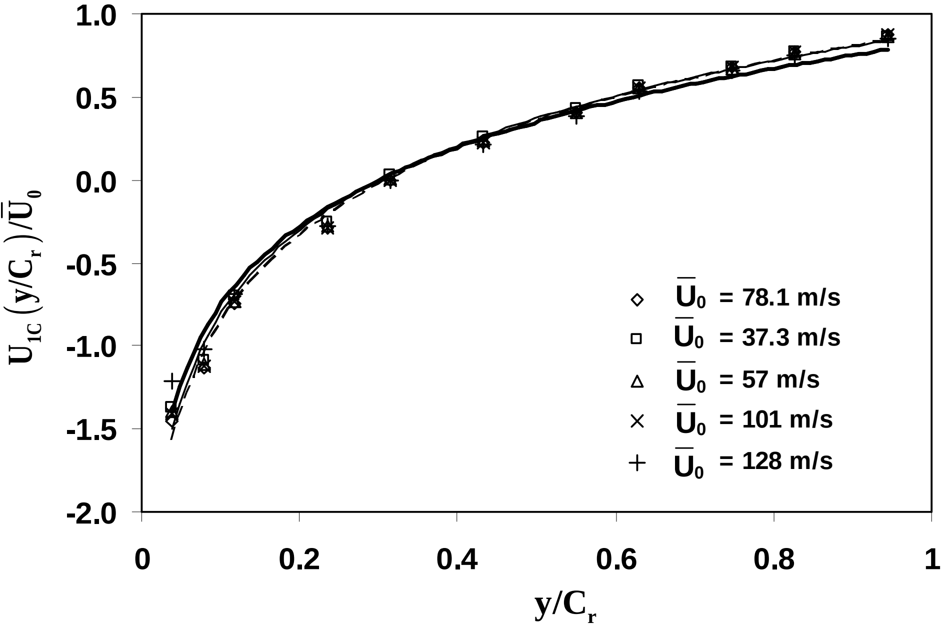

(b) U_{1C} Non-dimensionalized by $\bar{U}_0$

Fig. 14. Effect of seal inlet streamwise velocity on disturbance axial velocity (cosine).

(4) Axial Velocity Disturbance Sine Component, $\bar{U}_{1S}$

$\bar{U}_{1S}$ at the seal inlet is affected, in the order of importance, by $(\omega R_{sh} - \bar{W}_0)$, C_r, and $\bar{U}_0$. It is interesting to note that it is the swirl slip combination that has a large and consistent effect on $\bar{U}_{1S}$, rather than ω, R_{sh} and $\bar{W}_0$.

(5) Pressure Disturbance Cosine Component, $\bar{P}_{1C}$

The radial force exerted by the fluid on the rotor is obtained by integration of the pressure disturbance along the rotor surface, as shown in Eq. (3.22). Any configuration and operation condition quantities affecting the pressure disturbance will affect the radial force accordingly. $\bar{P}_{1C}$ at the seal inlet is controlled, in descending order of importance, by $\bar{U}_0$, $\bar{W}_0$, $\bar{P}_0$, C_r, and Ω.

(6) Pressure Disturbance Sine Component, $\bar{P}_{1S}$

$\bar{P}_{1S}$ at the seal inlet is affected, in the order of importance, by (ωR_{sh} - $\bar{W}_0$), $\bar{U}_0$, $\bar{P}_0$, and Ω. Also the seal inlet $\bar{P}_{1S}$ was found to have an almost linear relationship with the seal inlet $\bar{W}_{1C}$.

4. Summary

1. From the parametric study it was learned that the cross-coupled stiffness is influenced, in descending order of importance, by seal-inlet quantities W_{1C}, U_{1S}, P_{1S} and W_{1S}. In contrast to the historical assumption of $W_{1C} = 0$, the magnitude of W_{1C} was found to be larger than that of U_{1S}, and it is no less than that of the streamwise velocity disturbance U_{1C}.

2. The swirl "slip" velocity (ωR_{sh} - $\bar{W}_0$) was found to have a precisely correlated relationship with the bulk-average swirl velocity disturbance cosine component $\bar{W}_{1C}$, which exerts a surprisingly large effect on the cross-coupled stiffness k. In addition, it was found that the swirl "slip" is the predominant influencing

factor on axial velocity and pressure disturbance U_{1C} and P_{1S}.

3. The cosine component of swirl velocity disturbance W_{1C} is almost independent of the leakage flow rate. Likewise, the sine component W_{1S} shows nearly no dependence on the seal inlet swirl velocity.

4. The upstream chamber size and shape were found to have a substantial influence on the seal-inlet swirl disturbance velocity W_{1S}; this quantity plays a preeminent role in determining the direct stiffness K. The effect of upstream chamber size and shape on W_{1S} dramatically changes at the dividing point of about $(UCL/C_r)(UCH/C_r) = 400$.

C. Correlation Development

As mentioned above, the influence of each quantity on each seal-inlet disturbance variable differs. Accordingly, correlations for the seal-inlet boundary conditions were carefully devised in order for the influence of each quantity to be reflected as accurately as possible. The procedure and methodology used to formulate the seal inlet correlations are discussed below using, as examples, the correlation development of W_{1C} and W_{1S} for large axial-inlet upstream chambers. A similar method was adopted for correlation development of the disturbance variables for the other seal-inlet geometry category, i.e. small axial-inlet as well as radial-injection upstream chambers. The two newly developed groups of correlations are presented. Guidelines explaining how to apply these correlations and the application range of each are also discussed.

1. Correlation Development for W_{1C} (Large Axial-Inlet Upstream Chambers)

It was learned from the extensive parametric studies of large upstream chambers that $\bar{W}_{1C}$ is influenced, in descending order of importance, by $(\omega R_{sh}$ - $\bar{W}_0)$, C_r, $\bar{P}_0$, *UCL*, *UCH*, and Ω. Each of these parameters should appear in dimensionless form in the W_{1C} correlation, and the impact power, *i.e.* the exponent giving minimum scatter in curve fitting, of each should be preserved. However, the impact power of some parameters has to be compromised in order to obtain a reasonably simple correlation. The four steps used to develop the $\bar{W}_{1C}$ correlation using these parameters are as follows:

a. $\bar{W}_{1C}$ and the Swirl "Slip" (ωR_{sh} - $\bar{W}_0$)

Figure 10 exhibits a linear relation between $\bar{W}_{1C}$ and the swirl "slip" (ωR_{sh} - $\bar{W}_0$) that gives a greatly minimized scatter of $\bar{W}_{1C}$. Any change in the swirl "slip", whether it is from the spin speed, shaft radius or swirl velocity, will cause a rather precise linear variation of $\bar{W}_{1C}$. It is clear that the $\bar{W}_{1C}$ correlation should benefit from the improved precision and that the swirl slip (ωR_{sh} - $\bar{W}_0$) should be employed rather than $\bar{W}_0$ and ωR_{sh} individually.

b. $\bar{W}_{1C}$ and C_r, *UCL* and *UCH*

It was found that $\bar{W}_{1C}$ is directly proportional to C_r while being inversely proportional *UCL* and *UCH.* Thus, it was deemed necessary to combine these geometric quantities as shown in Fig. 15 where the exponents were found by a trial-and-error procedure to give maximum precision.

c. $\bar{W}_{1C}$ and Whirl-To-Spin Ratio (Ω/ω)

Upon combining the results of steps *a* and *b*, the bulk $\bar{W}_{1C}$ was non-dimensionalized as,

$$\frac{\bar{W}_{1C}}{\left(\omega R_{sh} - \bar{W}_0\right)\left(\frac{UCL}{C_r}\right)^{-0.13}\left(\frac{UCH}{C_r}\right)^{-0.15}} \tag{4.2}$$

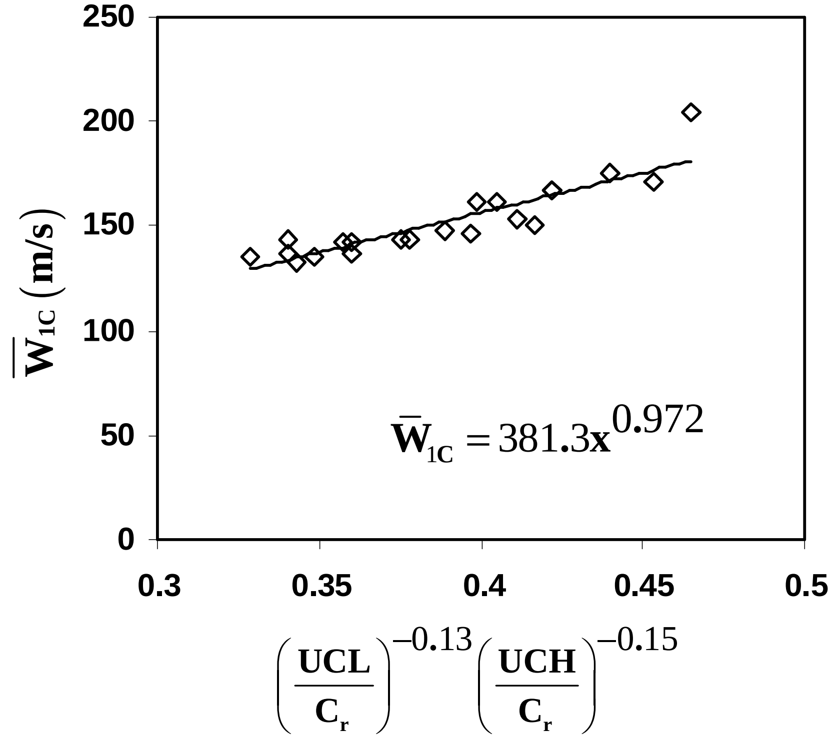

Fig. 15. Relation of the seal inlet W_{1C} with the dimensionless variable that combines the effect of Clearance C_r and upstream chamber size UCL and UCH. $\left[x \text{ represents } \left(\frac{\mathrm{UCL}}{\mathrm{C_r}}\right)^{-0.13}\left(\frac{\mathrm{UCH}}{\mathrm{C_r}}\right)^{-0.15}\right]$

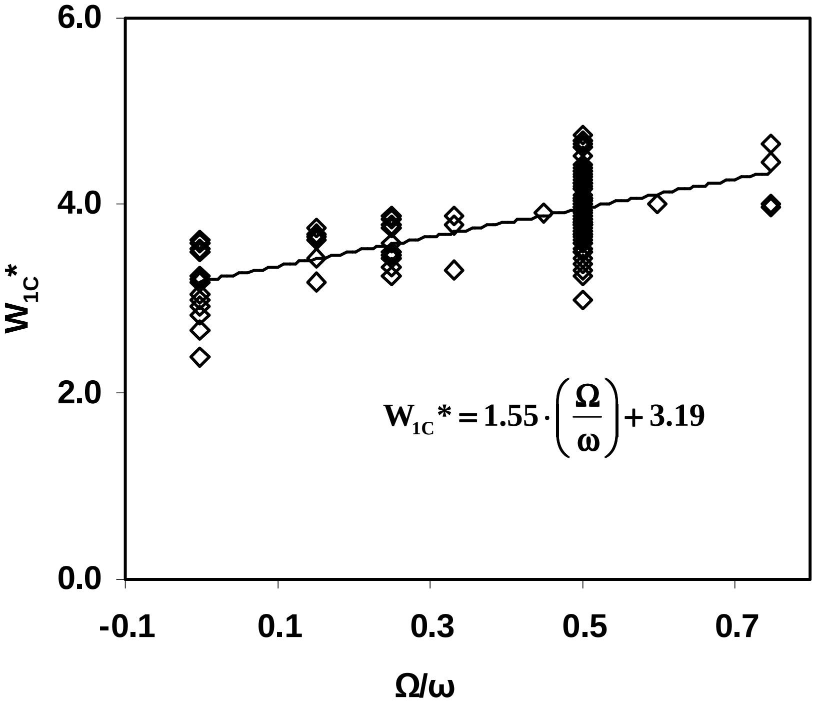

Fig. 16. Dimensionless swirl-disturbance velocity (cosine) variation with whirl spin ratio. [$W_{1C}*$ includes both the swirl "slip" and configuration effect.]

Then the effect of the whirl-to-spin ratio was incorporated by curve-fitting as shown in Fig. 16 as,

$$\frac{\bar{W}_{1C}}{\left(\omega R_{sh} - \bar{W}_0\right)\left(\frac{UCL}{C_r}\right)^{-0.13}\left(\frac{UCH}{C_r}\right)^{-0.15}} = 1.55\left(\frac{\Omega}{\omega}\right) + 3.19 \tag{4.3}$$

Finally, by rearranging Eq. (4.3), the correlation for bulk flow models can be written as Eq. (4.4); it is also listed in the table on p. 57.

$$\frac{\bar{W}_{1C}}{\left(\omega R_{sh} - \bar{W}_0\right)} = \left(\frac{UCL}{C_r}\right)^{-0.13}\left(\frac{UCH}{C_r}\right)^{-0.15}\left[1.55\left(\frac{\Omega}{\omega}\right) + 3.19\right] \tag{4.4}$$

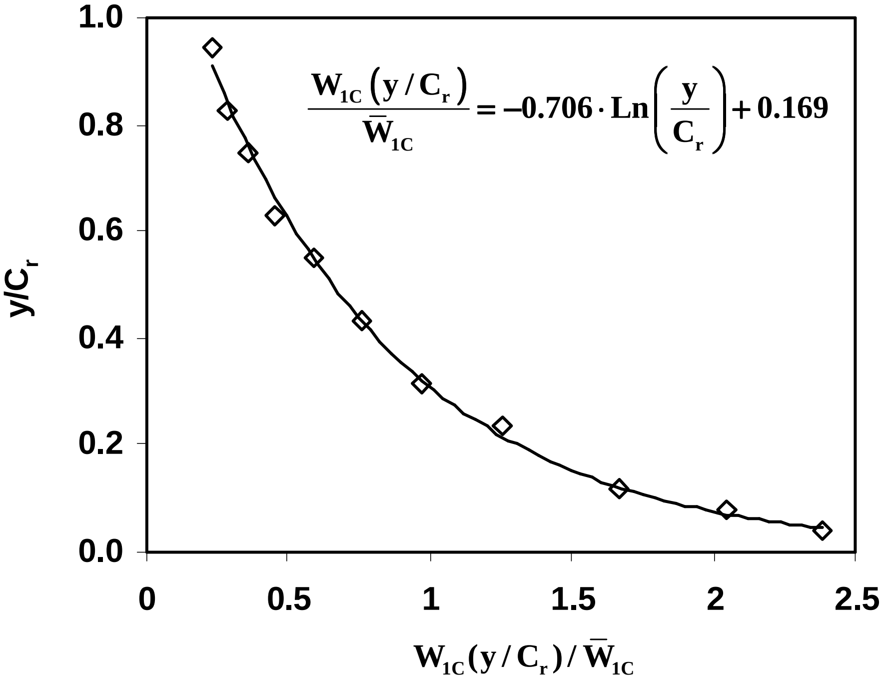

Fig. 17. Non-uniform radial profile of the swirl disturbance velocity (cosine) at the seal inlet.

d. W_{1C} Profile Correlation

A highly non-uniform W_{1C} radial profile was found across the clearance of the first tooth from the CFD perturbation solutions. Thus, for CFD models and CFD perturbation models, a correlation for this seal-inlet W_{1C} radial profile is more desirable than one for bulk $\bar{W}_{1C}$. Figure 17 displays the W_{1C} profile distribution for one typical operating condition (P_0 = 50 bar; M = 0.2,; W_{in} = 30m/s; C_r = 0.254mm; R_{sh} =76.2mm). The ordinate quantity is the dimensionless distance from the rotor surface, and the abscissa quantity is the W_{1C} radial profile non-dimensionalized by its bulk average value. The resulting curve fit of the CFD-perturbation solution within the clearance of the first tooth gives:

$$\frac{W_{1C}\left(y\right)}{\bar{W}_{1C}} = -0.706 \cdot Ln\left(\frac{y}{C_r}\right) + 0.169 \tag{4.5}$$

Applying Eq. (4.5) to Eq. (4.4), the complete expression for the W_{1C} profile correlation for CFD models and CFD-perturbation models was obtained, as shown in the table on page 57, as,

$$\begin{aligned}\frac{W_{1C}\left(y/C_r\right)}{\left(\omega R_{sh} - \bar{W}_0\right)} = \left(\frac{UCL}{C_r}\right)^{-0.13}\left(\frac{UCH}{C_r}\right)^{-0.15}\left[1.55\left(\frac{\Omega}{\omega}\right) + 3.19\right]\\ \left\{-0.706 \cdot Ln\left(\frac{y}{C_r}\right) + 0.169\right\}\end{aligned} \tag{4.6}$$

2. Correlation Development for $\bar{W}_{1S}$ (Large Axial-Inlet Upstream Chambers)

As discussed earlier, $\bar{W}_{1S}$ is influenced, in the order of importance, by C_r, $\bar{U}_0$, UCL, UCH, R_{sh} and Ω. Here $\bar{U}_0$ is used to non-dimensionalize $\bar{W}_{1S}$.

For large upstream chambers, UCL and UCH have negative impact exponents of -0.884 and -0.667 respectively while C_r and R_{sh} have positive impact exponents of 0.959 and 0.730, respectively. These four quantities were incorporated to formulate

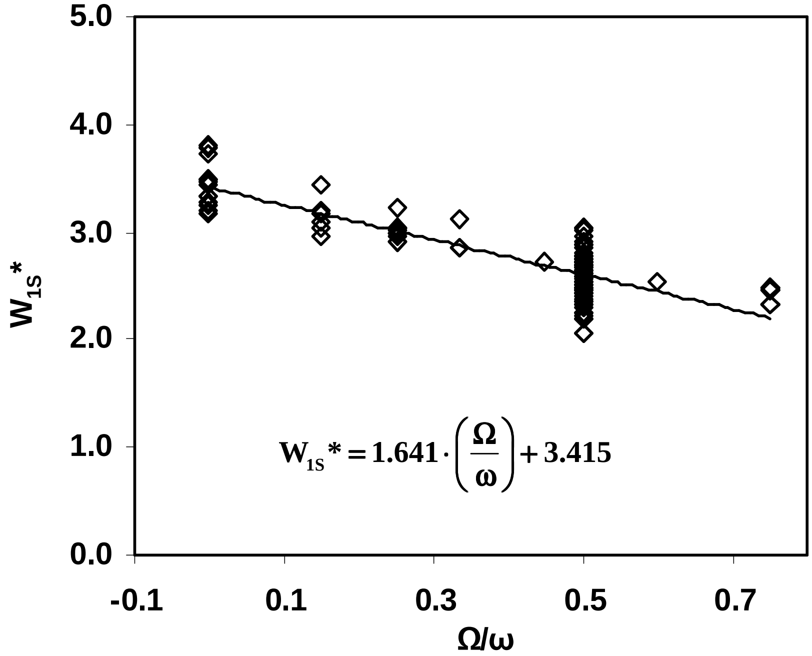

Fig. 18. Dimensionless swirl-disturbance velocity (sine) variation with the seal inlet whirl spin ratio.

the dimensionless variable. A trial combination of these four parameters is:

$$\left(\frac{UCL}{C_r}\right)^{-0.884}\left(\frac{UCH}{C_r}\right)^{-0.667}\left(\frac{R_{sh}}{C_r}\right)^{0.67} \tag{4.7}$$

Figure 18 displays the dimensionless W_{1S}* (defined in Eq. 4.5) variation with the whirl-to-spin ratio (Ω/ω), with W_{1S}* already incorporating the effect of both $\bar{U}_0$ and the configuration (*i.e.* C_r, *UCL*, *UCH*, and R_{sh}).

$$W_{1S}^{*} = \left[-1.641\left(\frac{\Omega}{\omega}\right) + 3.415\right] \tag{4.8}$$

where

$$W_{1S}^{*} = \frac{\overline{W}_{1S}}{\overline{U}_0\left(\frac{UCL}{C_r}\right)^{-0.884}\left(\frac{UCH}{C_r}\right)^{-0.667}\left(\frac{R_{sh}}{C_r}\right)^{0.67}} \tag{4.9}$$

Rearranging Eq. 4.5, the expression for the $\bar{W}_{1S}$ correlation is given by Eq. 4.6. It is also listed in Table IV.

$$\frac{\overline{W}_{1S}}{\overline{U}_0} = \left(\frac{UCL}{C_r}\right)^{-0.884} \left(\frac{UCH}{C_r}\right)^{-0.667} \left(\frac{R_{sh}}{C_r}\right)^{0.67} \left[-1.641\left(\frac{\Omega}{\omega}\right) + 3.415\right] \qquad (4.10)$$

3. Correlation Development for Other Disturbance Variables

Similar procedures were used to obtain the correlations for $\bar{U}_{1C}, \bar{U}_{1S}, \bar{P}_{1C}$ and $\bar{P}_{1S}$ for large upstream chambers as shown in Figs. 19 and 20. No correlation is necessary for $\bar{\rho}_{1C}$ and $\bar{\rho}_{1S}$ once correlations for $\bar{P}_{1C}$ and $\bar{P}_{1S}$ are obtained, because $\bar{\rho}_{1C}$ and $\bar{\rho}_{1S}$ can be easily evaluated from $\bar{\rho}_{1C} = \bar{P}_{1C}/RT$, and $\bar{\rho}_{1S} = \bar{P}_{1S}/RT$. The disturbance correlations at the seal inlet shown in Table IV are valid for large axial-inlet up-chambers as shown in Fig. 2(a) with $(UCL/C_r)(UCH/C_r) \geq 400$. For the small axial-inlet upstream chambers, as well as the radial injection chambers, shown in Fig. 2(b) with $(UCL/C_r)(UCH/C_r) < 400$, the same procedures gave the seal inlet flow disturbance boundary condition correlations listed in Table V.

4. Guidelines for Applying Correlations

The correlations are applicable for both bulk flow models and CFD models according to the following:

1. For bulk flow models, use the correlations for the bulk-averaged disturbance variables listed in Tables IV and V with the bulk option for W_{1C}.

2. For CFD-perturbation models, use the correlations for the bulk-averaged disturbance variables listed in Tables IV and V with the profile option for W_{1C}.

3. For full 3-D CFD models, use Eq. (3.10) along with the correlations for the bulk-averaged disturbance variables listed in Tables IV and V with the profile option for W_{1C}.

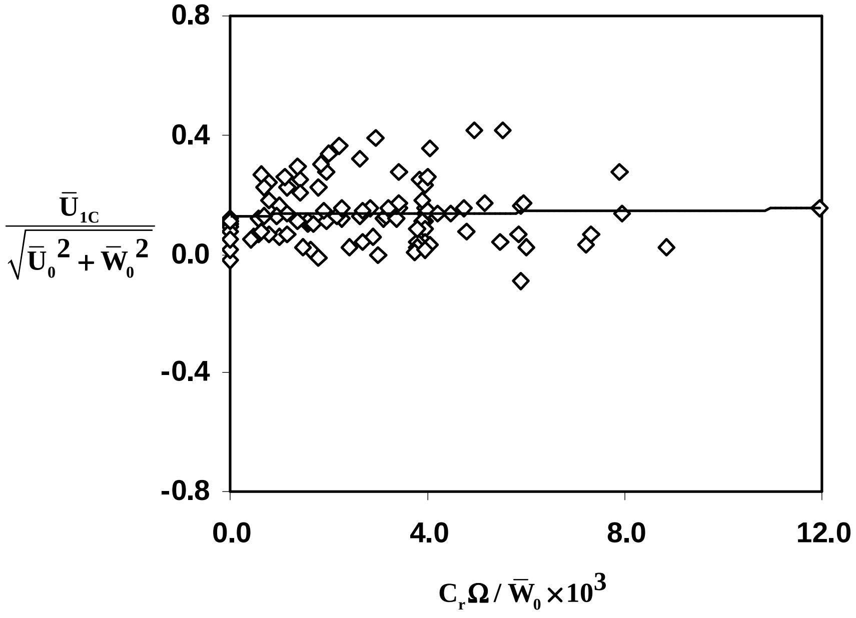

(a) Axial velocity disturbance (cosine)

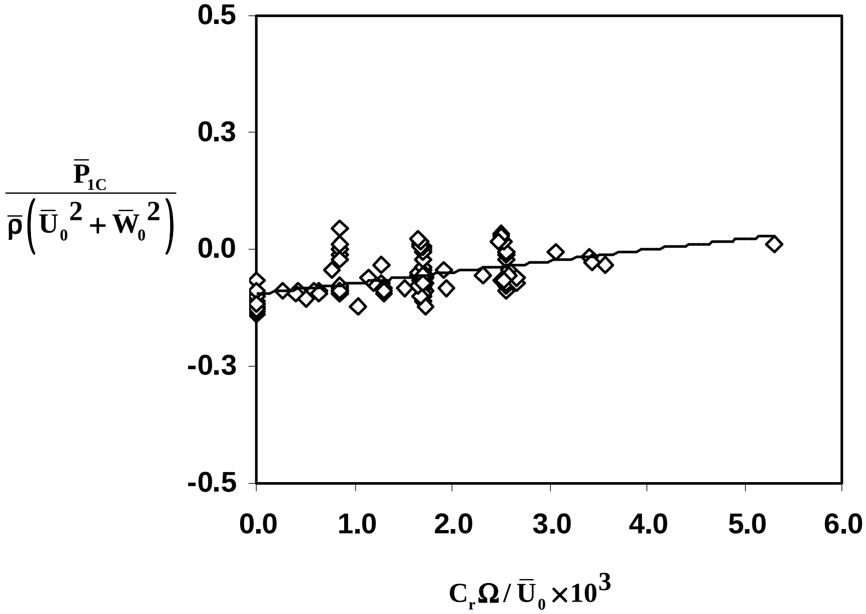

(b) Pressure disturbance (cosine)

Fig. 19. Bulk-averaged seal inlet disturbance correlations: (a) axial velocity disturbance (cosine), $\bar{U}_{1C}$; (b) Pressure disturbance (cosine), $\bar{P}_{1C}$.

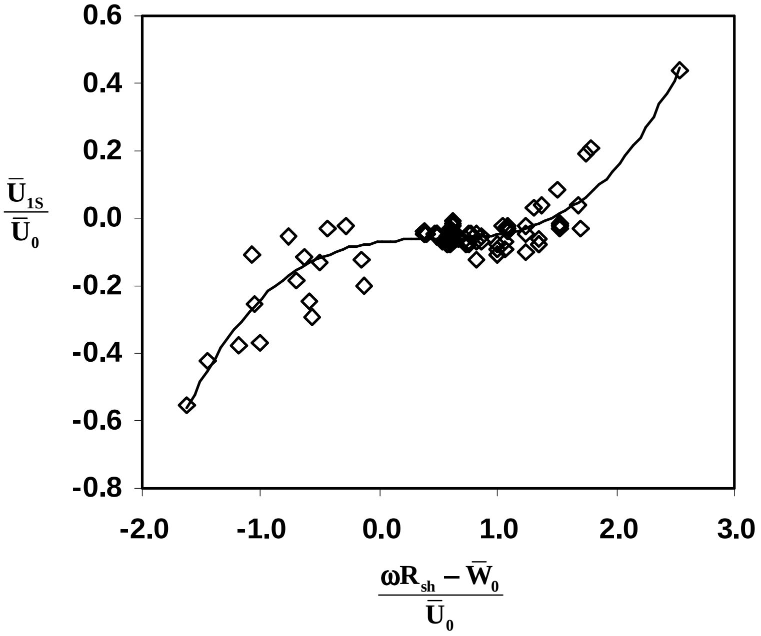

(a) Axial velocity disturbance (sine)

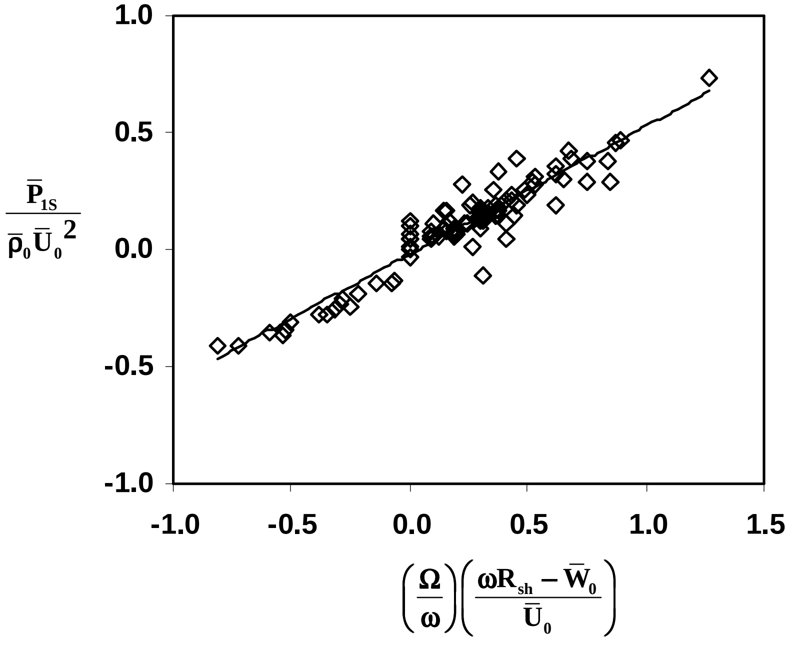

(b) Pressure disturbance (sine)

Fig. 20. Bulk-averaged seal inlet disturbance correlations: (a) axial velocity disturbance (cosine), $\bar{U}_{1S}$; (b) Pressure disturbance (cosine), $\bar{P}_{1S}$.

Table IV. Seal Inlet Flow Disturbance Boundary Conditions for Large Axial Inlet Up-Chambers

$\bar{W}_{1C}$ (bulk)	$\dfrac{\bar{W}_{1C}}{\left(\omega R_{sh}-\bar{W}_0\right)}=\left(\dfrac{UCL}{C_r}\right)^{-0.13}\left(\dfrac{UCH}{C_r}\right)^{-0.15}\left[1.55\left(\dfrac{\Omega}{\omega}\right)+3.19\right]$
$W_{1C}(y/C_r)$ (profile)	$\dfrac{W_{1C}\left(y/C_r\right)}{\left(\omega R_{sh}-\bar{W}_0\right)}=\left(\dfrac{UCL}{C_r}\right)^{-0.13}\left(\dfrac{UCH}{C_r}\right)^{-0.15}\left[1.55\left(\dfrac{\Omega}{\omega}\right)+3.19\right]$ $\left\{-0.706\cdot Ln\left(\dfrac{y}{C_r}\right)+0.169\right\}$
$\bar{W}_{1S}$	$\dfrac{\bar{W}_{1S}}{\bar{U}_0}=\left(\dfrac{UCL}{C_r}\right)^{-0.884}\left(\dfrac{UCH}{C_r}\right)^{-0.667}\left(\dfrac{R_{sh}}{C_r}\right)^{0.67}\left[-1.641\left(\dfrac{\Omega}{\omega}\right)+3.42\right]$
$\bar{U}_{1C}$	$\dfrac{\bar{U}_{1C}}{\sqrt{\bar{U}_0^2+\bar{W}_0^2}}=-1.69\dfrac{C_r\Omega}{\bar{W}_0}+0.125$
$\bar{U}_{1S}$	$\dfrac{\bar{U}_{1S}}{\bar{U}_0}=0.0541\left(\dfrac{\omega R_{sh}-\bar{W}_0}{\bar{U}_0}\right)^3-0.0737\left(\dfrac{\omega R_{sh}-\bar{W}_0}{\bar{U}_0}\right)^2$ $+0.0421\left(\dfrac{\omega R_{sh}-\bar{W}_0}{\bar{U}_0}\right)-0.0706$
$\bar{P}_{1C}$	$\dfrac{\bar{P}_{1C}}{\bar{\rho}_0\left(\bar{U}_0^2+\bar{W}_0^2\right)}=23.6\dfrac{C_r\Omega}{\bar{U}_0}-0.0959$
$\bar{W}_{1S}$	$\dfrac{\bar{P}_{1S}}{\bar{\rho}_0\bar{U}_0^2}=0.547\left(\dfrac{\Omega}{\omega}\right)\left(\dfrac{\omega R_{sh}-\bar{W}_0}{\bar{U}_0}\right)-0.0204$

Table V. Seal Inlet Flow Disturbance Boundary Conditions for Small Axial Inlet Up--Chambers and Radial-Injection Up-Chambers

$\bar{W}_{1C}$ (bulk)	$\frac{\bar{W}_{1C}}{\bar{U}_0} = 2.07\left(\frac{\omega R_{sh} - \bar{W}_0}{\bar{U}_0}\right) + 0.511$
$W_{1C}(y/C_r)$ (profile)	$\frac{W_{1C}\left(y/C_r\right)}{\bar{U}_0} = \left[2.07\left(\frac{\omega R_{sh} - \bar{W}_0}{\bar{U}_0}\right) + 0.511\right]\left\{0.563\left(\frac{y}{C_r}\right)^{-0.396}\right\}$
$\bar{W}_{1S}$	$\frac{\bar{W}_{1S}}{\bar{U}_0} = \left(\frac{UCL}{C_r}\right)^{0.1}\left(\frac{UCH}{C_r}\right)^{0.1}\left(\frac{R_{sh}}{C_r}\right)^{0.26}\left[-1.43\left(\frac{\Omega}{\omega}\right) + 1.53\right]$
$\bar{U}_{1C}$	$\frac{\bar{U}_{1C}}{\sqrt{\bar{U}_0^2 + \bar{W}_0^2}} = -83.2\frac{C_r\omega}{\sqrt{\bar{U}_0^2 + \bar{W}_0^2}} - 0.0819$
$\bar{U}_{1S}$	$\frac{\bar{U}_{1S}}{\sqrt{\bar{U}_0^2 + \bar{W}_0^2}} = -24.0\frac{C_r\Omega}{\sqrt{\bar{U}_0^2 + \bar{W}_0^2}} - 0.0283$
$\bar{P}_{1C}$	$\frac{\bar{P}_{1C}}{\bar{\rho}_0\bar{U}_0^2} = -5.78\frac{C_r\Omega}{\sqrt{\bar{U}_0^2 + \bar{W}_0^2}} + 0.233$
$\bar{W}_{1S}$	$\frac{\bar{P}_{1S}}{\bar{\rho}_0\left(\bar{U}_0^2 + \bar{W}_0^2\right)} = 0.469\frac{\sqrt{\omega R_{sh}}\left(\frac{3.5}{C_r}\omega R_{sh} - \bar{W}_0\right)}{\left(\sqrt{\bar{U}_0^2 + \bar{W}_0^2}\right)^{1.5}} + 0.022$

Recall that, even for choked flow gas seals, the up-chamber and even the seal inlet Mach number are less than 0.3. Thus, for gas as well as liquid seals the up-chamber and clearance of the first tooth exhibit what is essentially a uniform density. Therefore, the correlations are applicable for liquid as well as gas seals. Further, the correlations are applicable over an extremely wide range encompassing 0.10mm $< C_r <$ 0.50mm and $0.125 \leq \left| \left(\omega R_{sh} - \bar{W_0}\right) / \bar{W_0} \right| \leq 3.45$. The maximum swirl "slip" ratio among the computed cases that were correlated is 3.45, in which case the inlet swirl is -100 m/s and spin speed is 15,000 rpm. The inlet swirl velocity spans from -100 m/s to 250 m/s, which covers most seals of practical usage.

D. Summary

Thorough parametric studies from about 240 CFD-perturbation solutions were performed to better understand the seal-inlet rotordynamics. Specifically, these studies provided an improved understanding of how the seal-inlet disturbance quantities are influenced by seal configuration and operating conditions. Also, seal-inlet boundary condition correlations for the flow disturbance quantities were carefully developed based on new findings from the parametric studies. The parametric studies covered an extremely wide range so that the correlations would have a maximized range of applicability. Specific findings include:

1. Based on new findings from a careful parametric study, a complete set of correlations giving all of the seal inlet flow disturbance boundary conditions was developed. Especially the W_{1C} and W_{1S} correlations should be used to replace the historical guess that seal inlet $W_{1C} = 0$ and $W_{1C} = 0$. These new disturbance boundary conditions are applicable over an extremely wide range for seals with, for example, 0.1mm $< C_r <$ 0.5mm, -100m/s $< W_0 <$ 250m/s and

3,000 rpm $< \omega <$ 20,000 rpm. Because even choked flow gas seals exhibit an essentially uniform density (Mach number < 0.3) in the upstream chamber and seal inlet, the disturbance boundary conditions are applicable to gas as well as liquid seals.

2. From the parametric study it was learned that the cross-coupled stiffness is influenced, in descending order of importance, by seal-inlet W_{1C}, U_{1S}, P_{1S} and W_{1S}. In contrast to the historical assumption of seal-inlet $W_{1C} = 0$, the magnitude of W_{1C} is larger than that of U_{1S}, and it is similar to that of U_{1C}.

3. The seal-inlet swirl "slip" velocity $(\omega R_{sh} - \bar{W}_0)$ was found to have an extremely precise relationship with the cross-coupled stiffness as well as the seal-inlet bulk-average swirl velocity disturbance cosine component $\bar{W}_{1C}$. Thus, the number of experiments or computer runs needed to determine the effect of spin speed, shaft radius and inlet swirl velocity on the cross-coupled stiffness is greatly reduced by plotting the simplified relationship of the cross-coupled stiffness against the inlet swirl slip velocity $(\omega R_{sh} - \bar{W}_0)$. For example, seal rotordynamics test rig data at almost any shaft spin speed can be interpreted over a fairly wide range of spin speed, shaft radius and/or inlet swirl. In addition, it was found that the swirl "slip" is the predominant influencing factor on U_{1S} and P_{1S}.

4. The effect of upstream chamber size and shape on seal-inlet W_{1S} changes when $(UCL/C_r)(UCH/C_r) = 400$. It was also found that seal-inlet W_{1S} plays a significant role in determining the direct stiffness K.

CHAPTER V

CORRELATION ASSESSMENT

A. Introduction

The benefits of using the new seal-inlet boundary condition correlations were assessed by implementing them into a CFD-perturbation model. Two widely different test cases were employed. Case 1 is a test of the correlations for large upstream chambers using a simple liquid smooth-plain seal. Case 2 is a test for small, as well as radial injection, upstream chambers using a complicated gas labyrinth seal. Previous seal rotordynamic models, all of which assume $W_{1C} = W_{1S} = 0$, were also tested for the purpose of comparison.

B. Case 1: Long Liquid Smooth-Plain Seal

This is a test case for a simple liquid seal wherein the correlations for a large axial-inlet upstream chamber are appropriate. Specifically, Kanemori and Iwatsubo [53] measured the rotordynamic forces in a smooth-plain seal of L/D = 3 with a clearance and length of 0.394 mm and 240 mm, respectively. Water was used as the operating fluid. The seal pressure drops were 990 kPa and 500 kPa while the axial Re (= $2\rho U C_r/\mu$) were 9,300 and 16,300. The swirl velocity of the fluid entering the seal was measured using a pitot-tube installed in the upstream chamber.

1. CFD Considerations

The test rig upstream chamber dimensions were used for the CFD upstream chamber, with $UCL/C_r = 150$ and $UCH/C_r = 15$. Pressures at the domain inlet and exit are specified. On the rotor and stator walls, no-slip, adiabatic and smooth surface conditions were specified via standard wall-functions. At the domain exit the axial gradient of the velocity components and turbulence quantities were assumed zero. The computational cells were carefully designed in the near wall region so that the y^+ value of the first cell near the rotor varied between 15 and 55 from the inlet to the exit of the seal.

2. Grid Independence Testing

Grid independence testing was performed with a pressure drop of 490 kPa, a spin speed ω of 4680 rpm, and a swirl velocity ratio $(W_{in}/\omega R_{sh})$ of 0.67. Three grids were utilized whose cells inside the clearance have the dimension of 0.0381 mm × 0.0381 mm (coarse grid), 0.0254 mm × 0.0254 mm (production grid) and 0.0191 mm × 0.0191 mm (fine grid), respectively. The variation of the computed force coefficients from these three grids is very small. The coarse grid gave solutions with less than 2.2 percent discrepancy from the production grid and the production grid gave solutions with less than 1.5 percent discrepancy from the fine grid.

3. Results and Comparison with Measurement

The swirl "slip" ratio $(\omega R_{sh} - \bar{W}_0)/\bar{U}_0$ ranges from 0.5 to 0.9 in this investigation which is easily within the range 0.125∼3.45 over which the correlation is valid. Several new correlation versions (W_{1C}-profile, W_{1C}-bulk and the $W_{1C} = W_{1S} = 0$ versions) were tested to evaluate their performance for a liquid annular seal. The $W_{1C} = W_{1S} = 0$ version was included to show the benefit of having reasonable values for W_{1C} and W_{1S}, as all previous seal rotordynamic models (i.e. bulk-flow, CFD-perturbation and full 3-D CFD) were forced to assume that the swirl disturbance is zero. For simplicity, this correlation version will be referred to as "$W_{1C} = W_{1S} = 0$". The correlations listed in Table IV corresponding to large axial-inlet up-chambers were used in the present study because the configuration criterion (UCL/C_r)(UCH/C_r) is larger than 400 for the inlet upstream chambers.

Figure 21 shows the comparison with the measurements for the three whirl frequencies with a pressure drop of 990 rpm and an inlet swirl ratio ($W_{in}/\omega R_{sh}$) of 0.5. The new correlation versions with W_{1C}-profile and with W_{1C}-bulk gave almost the same prediction for the tangential impedance F_t/e; see Fig. 21 (a). Furthermore, both of them gave close agreement with measurements. The correlation version with $W_{1C} = W_{1S} = 0$ yielded considerably worse agreement with measurements than did the W_{1C}-profile and the W_{1S}-bulk versions because of the dependence of the tangential force on the seal-inlet swirl disturbance W_{1C}. The predicted F_t/e values generally differ from measurements by 40% at these conditions.

Comparison of radial impedance F_r/e between measurements and predictions from the same three correlation versions are shown in Fig. 21 (b). The W_{1C}-profile and W_{1C}-bulk versions gave almost identical radial impedance values as was found for the tangential impedance. Here predictions from both the W_{1C}-profile and W_{1C}-bulk versions are in reasonable agreement with the measurements. The agreement is particularly good when $(\Omega/\omega) = 0.5$, which is within the operating range where this type of rotordynamic instability typically occurs.

For the lower pressure drop of 500 kPa and the higher swirl velocity ratio of 0.69, tangential impedance F_t/e was over-predicted somewhat by both the W_{1C}-profile and W_{1C}-bulk versions. See Fig. 22 (a). Once again, the $W_{1C} = W_{1S} = 0$ version gave a substantially worse prediction than did the W_{1C}-profile and W_{1C}-bulk versions.

The W_{1C}-profile and W_{1C}-bulk predictions for F_r/e in Fig. 22 (b) are in very close agreement with measurements, especially near the important frequency of $(\Omega/\omega) = 0.5$. The version with $W_{1C} = W_{1S} = 0$ again gives more error for most of the operating range considered.

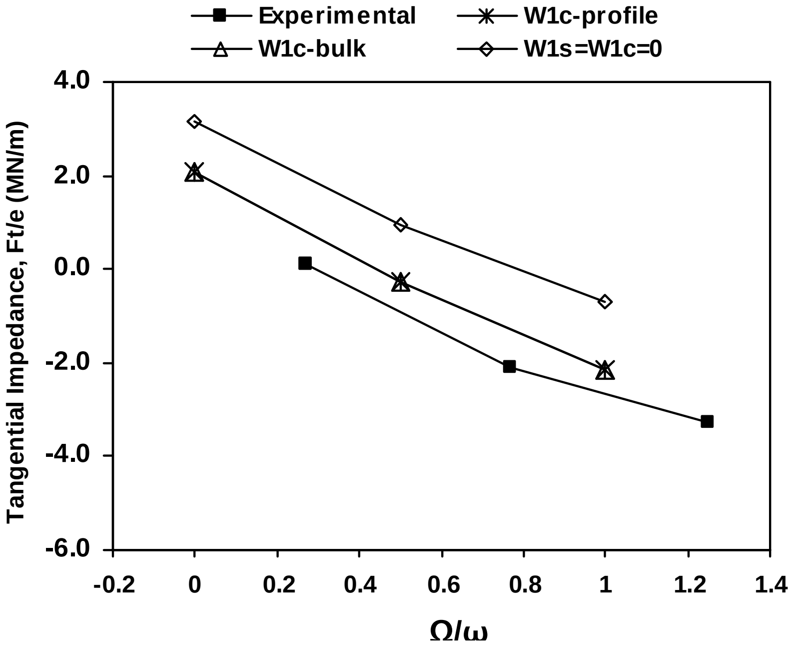

(a) Tangential Impedance

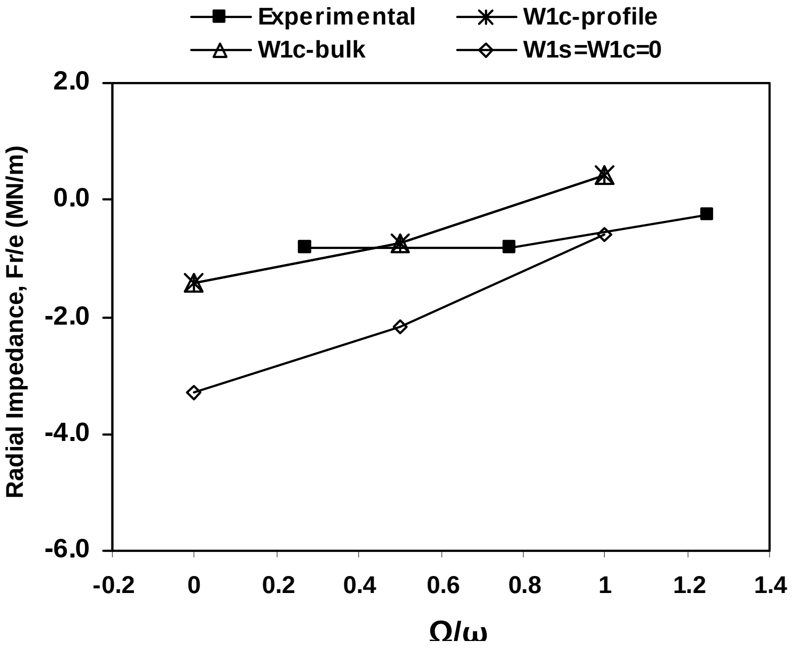

(b) Radial Impedance

Fig. 21. Comparison with measurements (Kanemori and Iwatsubo, 1994) of predictions using various seal-inlet, flow-disturbance boundary conditions: $\Delta P =$ 990 kPa, $\omega = 900$ rpm and $W_0/\omega R_{sh} = 0.50$.

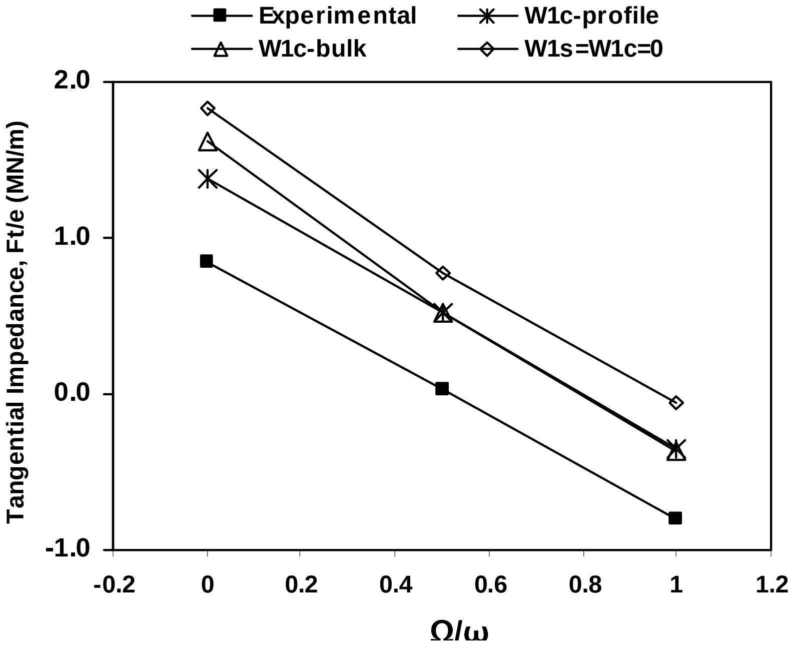

(a) Tangential Impedance

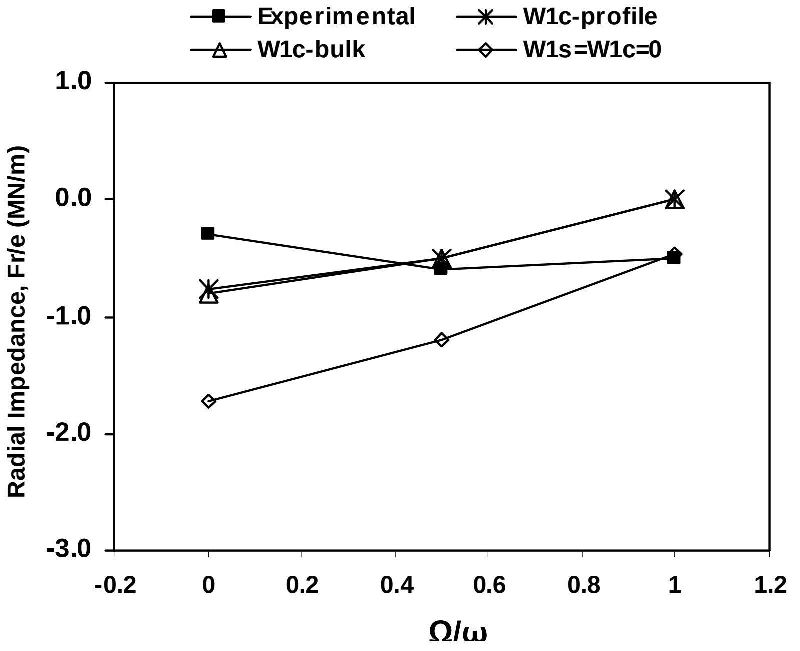

(b) Radial Impedance

Fig. 22. Comparison with measurements (Kanemori and Iwatsubo, 1994) of predictions using various seal-inlet, flow-disturbance boundary conditions: $\Delta P = 500$ kPa, $\omega = 600$ rpm and $W_0/\omega R_{sh} = 0.69$.

C. Case 2: Gas Labyrinth Seal

This is a test case for a rather complicated gas labyrinth seal that employs the correlations for the small axial-inlet, as well as the radial injection, upstream chamber. Soto and Childs [54] published the experimental results of this case, which are for a gas labyrinth seal with shunt injection. Recall that shunt injection is a very effective technique for improving seal stability. For some high-pressure compressors, shunt injection has become a fairly standard modification. The results confirmed that shunt injection at an angle against rotation has a large stabilizing effect and drastically reduces the cross-coupled stiffness coefficient. Even negative values of the cross-coupled stiffness coefficient were measured.

The gas labyrinth seal has very complicated flow patterns due to the presence of multiple cavities, tight clearances, and high shaft speeds. In addition, the present cases have high inlet swirl, high exit Mach number due to increased leakage and complex flow patterns in the injection chamber that make it a highly challenging test case to compute the rotordynamic forces.

1. CFD Considerations

The schematic diagram of the investigated balance piston seal with shunt injection is shown in Fig. 23. It is very long with originally 20 teeth on the stator wall. The fourth tooth from the high-pressure end was removed, and sixteen injection holes were machined through the cavity base for the cases considered here. High pressure air is injected through the holes against shaft rotation at a 30^o angle from the tangent. In the present CFD model, the sixteen injection holes were approximated by one circumferentially continuous injection slot with same flow area and same injection angle.

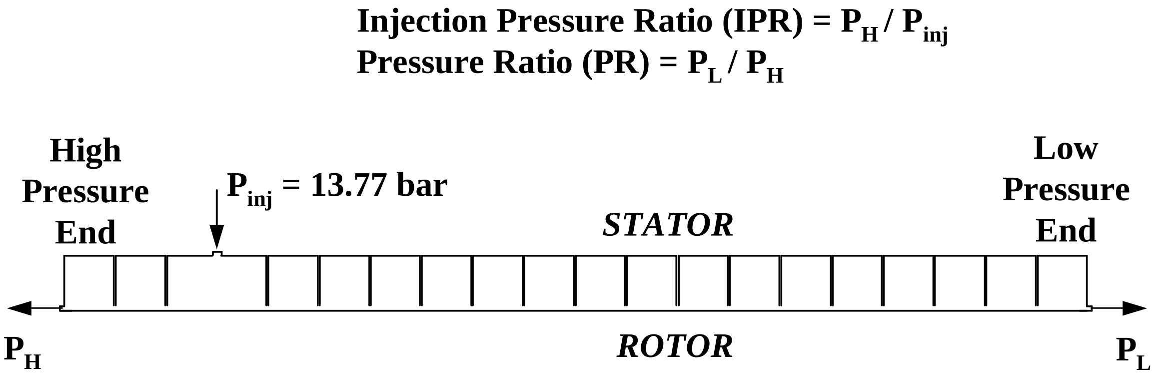

Fig. 23. Injection labyrinth seal configuration (not to scale); Tooth clearance = 0.22 mm (0.00866 in); tooth height =3.175 mm (0.125 in); Tooth pitch =3.175 mm (0.125 in); seal length (L) = 63.5 mm (2.5 in); Shaft radius (R_{sh}) = 64.69 mm (2.547 in).

In order to assess the new seal-inlet boundary conditions, the injection seal was approximated as having three distinct portions wherein each was computed separately. Two of these three portions were: the right-hand-side (18 teeth) and the left-hand-side (3 teeth) of the injection chamber, respectively, with the first tooth on each side treated as a seal-inlet. The third portion was the injection chamber having the circumferential injection slot as the inlet. The tangential and radial rotordynamic force components were computed for each portion separately, and their vector sum gave the values for the force coefficients.

The primary operating parameters that determine the flow pattern, other than the inlet swirl, are the pressure ratio ($PR = P_L/P_H$), the injection pressure ratio ($IPR = P_H/P_{inj}$) and the rotor spin speed. In this investigation, P_{inj} was fixed at 13.77 bar and the pressure at both ends was varied according to the considered pressure ratios. Two different shaft speeds (ω = 4680 and 8640 rpm) were investigated.

2. Grid Independence Testing

Grid independence tests have been conducted with pressure ratio $PR = 0.45$, injection pressure ratio $IPR = 0.85$ and shaft spin speed $\omega = 4680$ rpm. Three grids were utilized having cells inside the clearance with dimensions of 0.0381 mm × 0.0381 mm (coarse grid), 0.0254 mm × 0.0254 mm (production grid) and 0.0191 mm × 0.0191 mm (fine grid) respectively. The computed leakage and rotordynamic coefficients from the coarse grid deviate from those of the fine grid by less than 8.0 percent, while the deviation between the production grid and the fine grid falls within 3.3 percent.

3. Results and Comparison with Measurement

Comparisons of predicted and measured leakages are given in Fig. 24. The operating conditions of the test cases include two shaft speeds (4680 and 8640 rpm), three injection pressure ratios ($IPR = P_H/P_{inj}$ =0.85, 0.90 and 0.95) and three pressure ratios ($PR = P_L/P_H$ = 0.3, 0.45, and 0.65). The predicted leakages show excellent agreement with the measurements with about 2.0 percent over-prediction on average, considering the entire set of test cases involved. Thus, the error in the rotordynamic coefficients originating from the concentric-rotor, *i.e.* zeroth-order, solution appears to be small.

Similar to the liquid seals discussed above, the same three versions of seal-inlet flow disturbance boundary condition correlations were considered. They are the W_{1C}-profile, the W_{1C}-bulk, and the $W_{1C} = W_{1S} = 0$ versions. As mentioned earlier, the $W_{1C} = W_{1S} = 0$ version was included to show the benefit of using reasonable values of W_{1C} and W_{1S}. Because the Case 2 configuration has a radial injection up-chamber for both the left-hand-side and right-hand -side partial domains, the basic correlations of the Table V were used here. Three whirl-spin ratios (whirl/spin = 0.0, 0.1 and 0.15)

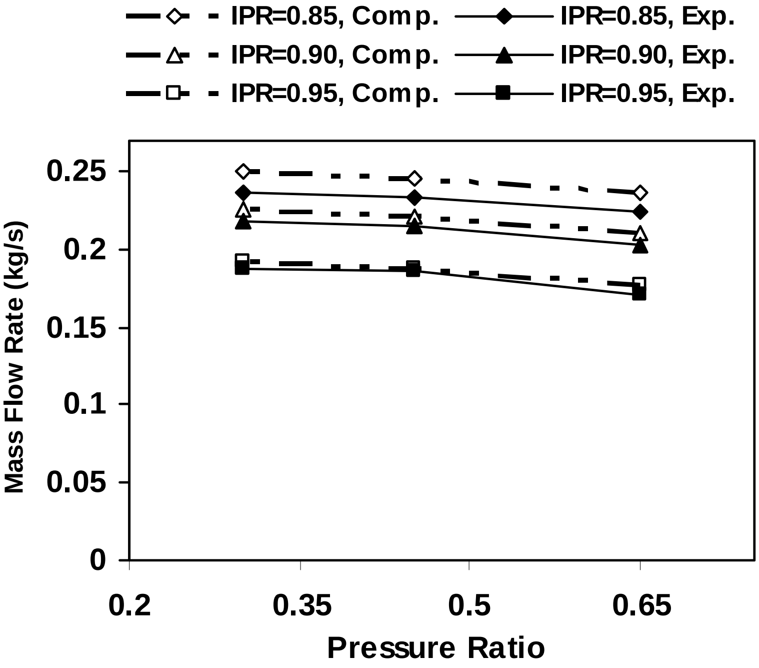

(a) Tangential Impedance

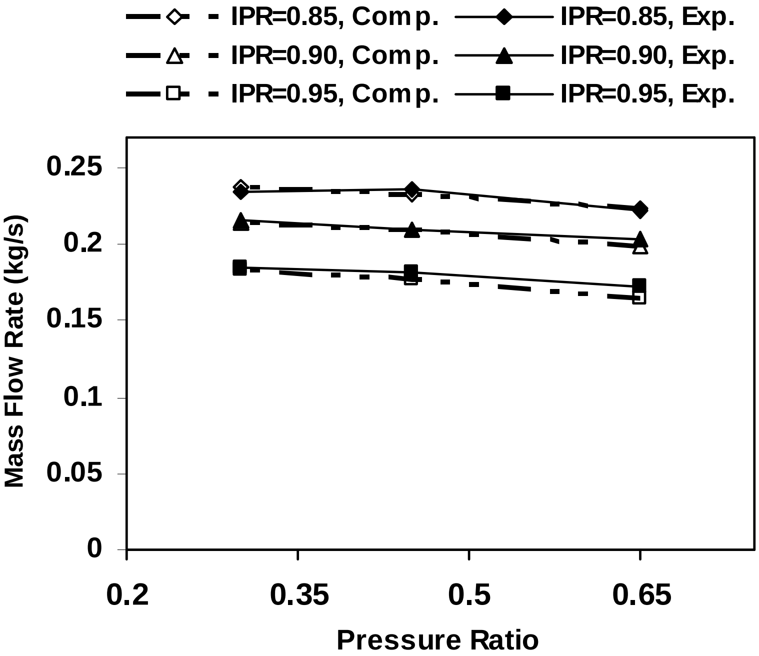

(b) Radial Impedance

Fig. 24. Comparison of predicted and measured (Soto, 1999) leakage with various shaft spin speeds, injection pressure ratios (IPR) and pressure ratios (PR).

were computed and curve-fitted to the usual quadratic linearized force equations to obtain the rotordynamic force coefficients. The predictions were compared with the measurements of [54] in Figs. 25 to 28.

a. Cross-Coupled Stiffness, k

Figure 25 shows the comparison of predicted and measured cross-coupled stiffness k with a pressure ratio PR of 0.65, two spin speeds of 4680 and 8640 rpm, and three injection pressure ratios varying from 0.85 to 0.95. The predicted cross-coupled stiffness coefficients from W_{1C}-profile and from W_{1C}-bulk show good agreement with measurements at the low spin speed; the benefit of having a reasonable seal-inlet W_{1C} and W_{1S} is seen by the substantially larger error for the $W_{1C} = W_{1S} = 0$ version. At the higher spin speed the W_{1C}-profile correlation again gives good agreement with measurements while the W_{1C}-bulk version under-predicts the measurements. Overall, the cross-coupled stiffness is predicted within about 14 percent of the measurements.

b. Direct Damping Coefficient, C

The comparison of the predicted and measured direct damping coefficient is shown in Fig. 26. The W_{1C}-profile and the W_{1C}-bulk versions give almost the same predictions at both spin speeds. At the lower spin speed these two versions predict the measurement within about 20 percent, while at the higher speed they predict it within about 30 percent.

c. Effective Damping Coefficient, C_{eff}

The effective damping, C_{eff}, is the net damping force divided by the whirl velocity. Sub-synchronous vibration with Ω equal to 0.5ω was assumed in evaluating C_{eff}. When positive, the net damping force acts in the direction opposite to the rotor

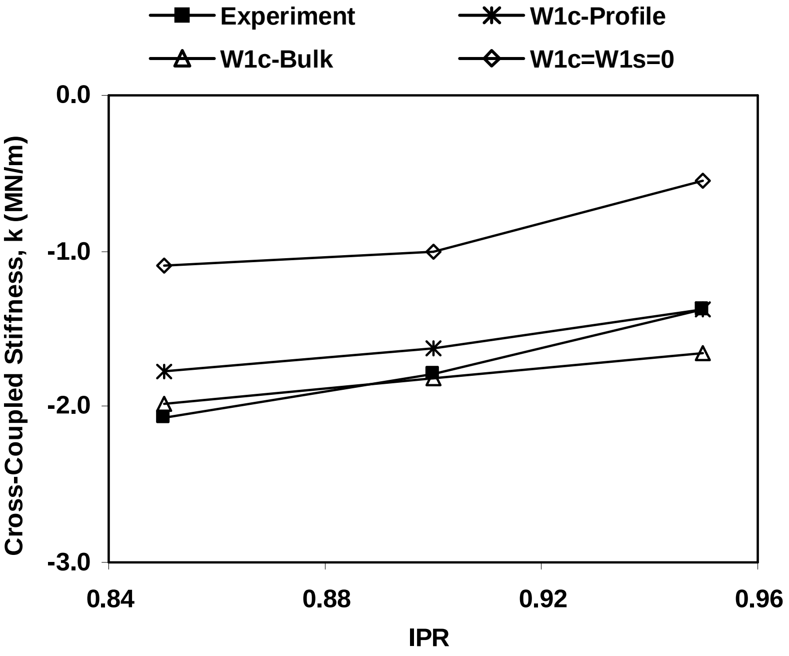

(a) $\omega = 4680\text{rpm};\ PR(P_L/P_H) = 0.65$

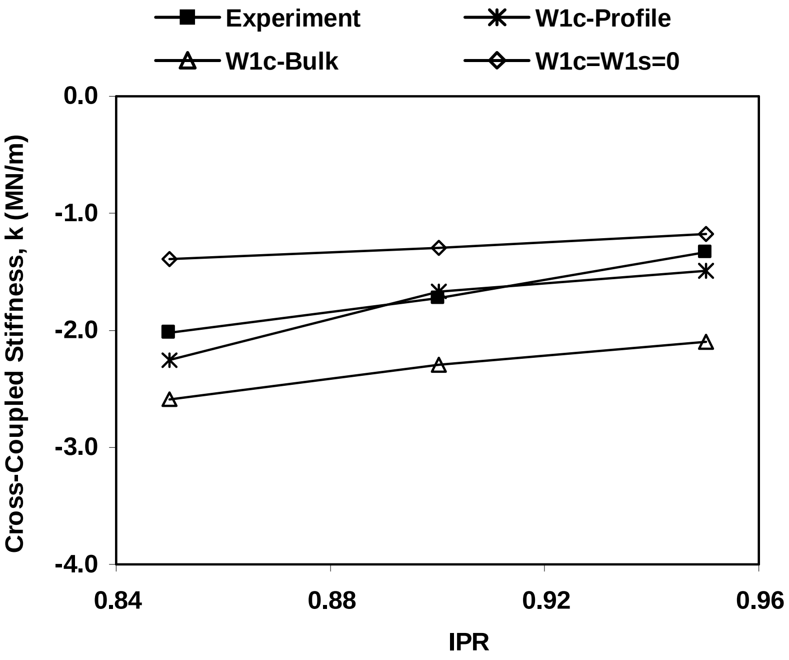

(b) $\omega = 8640\text{rpm};\ PR(P_L/P_H) = 0.65$

Fig. 25. Comparison with measurements (Soto, 1999) of predicted cross-coupled stiffness k using various seal-inlet, flow-disturbance boundary conditions; PR=0.65.

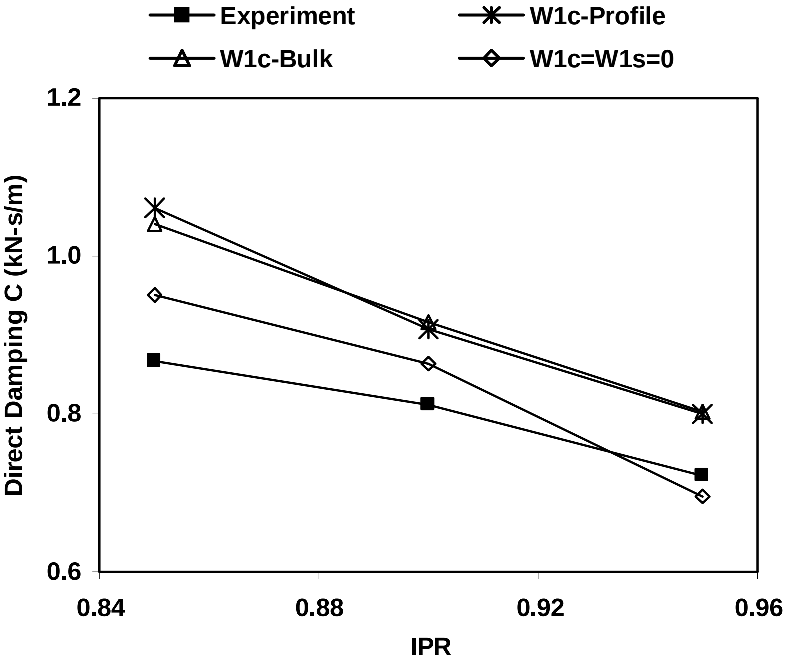

(a) $\omega = 4680\text{rpm}$; $PR(P_L/P_H) = 0.65$

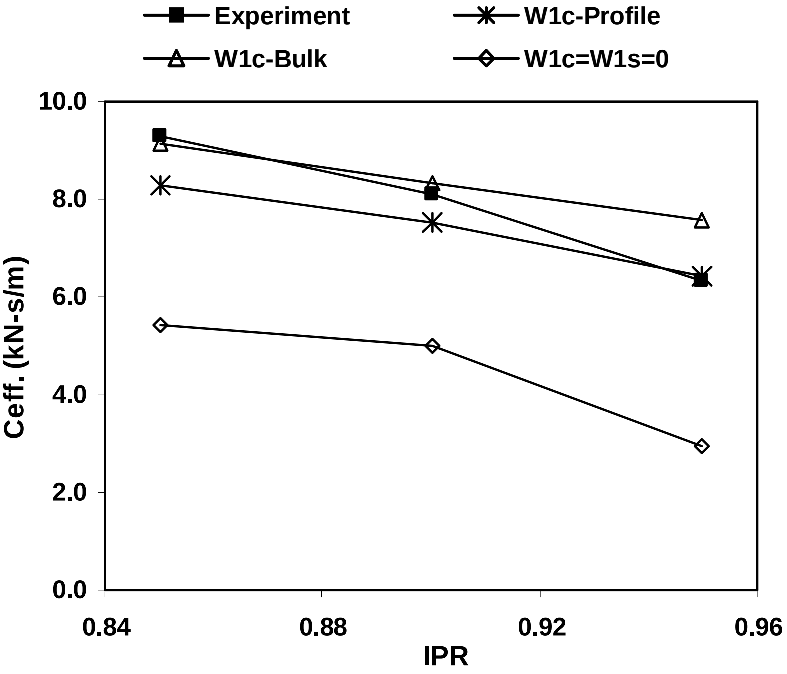

(b) $\omega = 8640\text{rpm}$; $PR(P_L/P_H) = 0.65$

Fig. 26. Comparison with measurements (Soto, 1999) of predicted direct damping coefficient C using various seal-inlet, flow-disturbance boundary conditions; PR=0.65.

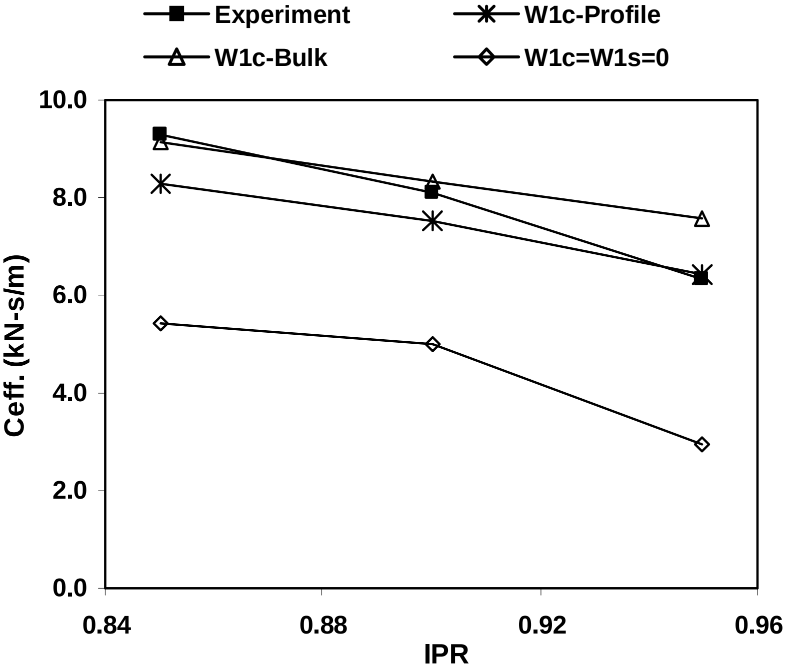

(a) $\omega = 4680\text{rpm};\ PR(P_L/P_H) = 0.65$

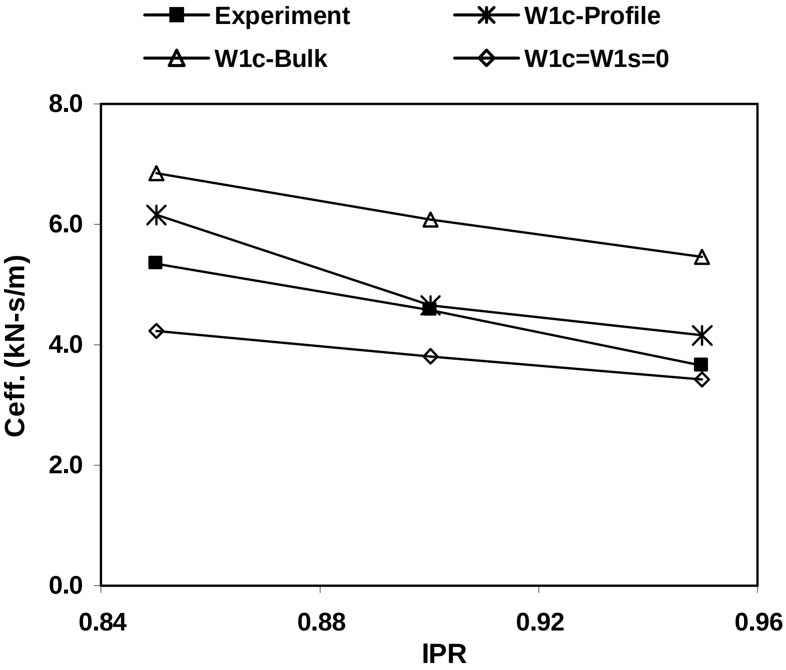

(b) $\omega = 8640\text{rpm};\ PR(P_L/P_H) = 0.65$

Fig. 27. Comparison with measurements (Soto, 1999) of predicted effective damping coefficient C_{eff} using various seal-inlet, flow-disturbance boundary conditions; PR=0.65.

whirl and is therefore the net stabilizing force. In Fig. 27, one finds that at the low spin speed, both W_{1C}-profile and W_{1C}-bulk versions give excellent agreement (within about 6 percent) with the measurements, whereas the $W_{1C} = W_{1S} = 0$ version gives substantial error. At the higher spin speed of 8640 rpm, the W_{1C}-profile version continues to give good agreement with measurement, while the W_{1C}-bulk version begins to significantly over-predict C_{eff} with a deviation of about 12 percent on average. Because C_{eff} is likely the best overall indication of seal stability, the W_{1C}-profile version is recommended over the W_{1C}-bulk version for the CFD models due to its superior overall performance. The W_{1C}-bulk version is recommended for the bulk-flow models because the W_{1C}-profile version cannot be utilized due to the modelling requirements.

d. Direct Stiffness, K

The direct stiffness coefficient represents the radial impedance force exerted on the rotor by the fluids, and a large magnitude of K indicates that instability-induced motion with large displacement is unlikely.

Figure 28 illustrates the predicted and measured direct stiffness using the various versions of the seal-inlet flow disturbance boundary conditions. All the predictions generally agree well with the measurements, i.e. within about 20 percent. From Eq.3.22, observe that the direct stiffness is obtained by integrating the cosine component of pressure disturbance (P_{1C}) along the rotor surface. As discussed in Section $IV.B.3$ (parametric study), it was found that P_{1C} is influenced primarily by W_{1S}, which is proportional to the leakage or U_0. Observe that increasing the injection pressure ratio ($IPR = P_H/P_{inj}$) reduces the flow rate (P_{inj} was constant in the present study) as depicted in Fig. 24. This flow reduction reduces the magnitude of W_{1S}, which in turn decreases the magnitude of P_{1C} and thus the radial impedance.

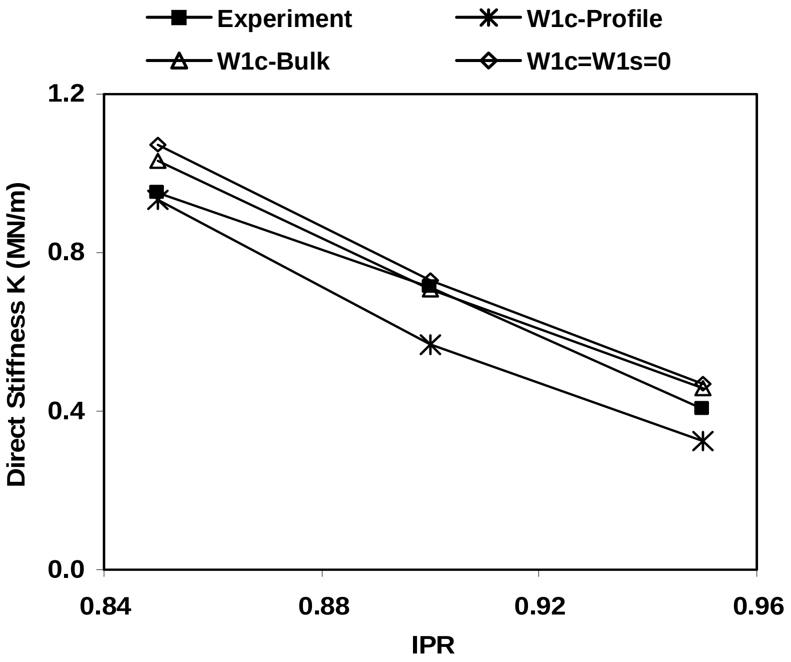

(a) ω = 4680rpm; $PR(P_L/P_H) = 0.65$

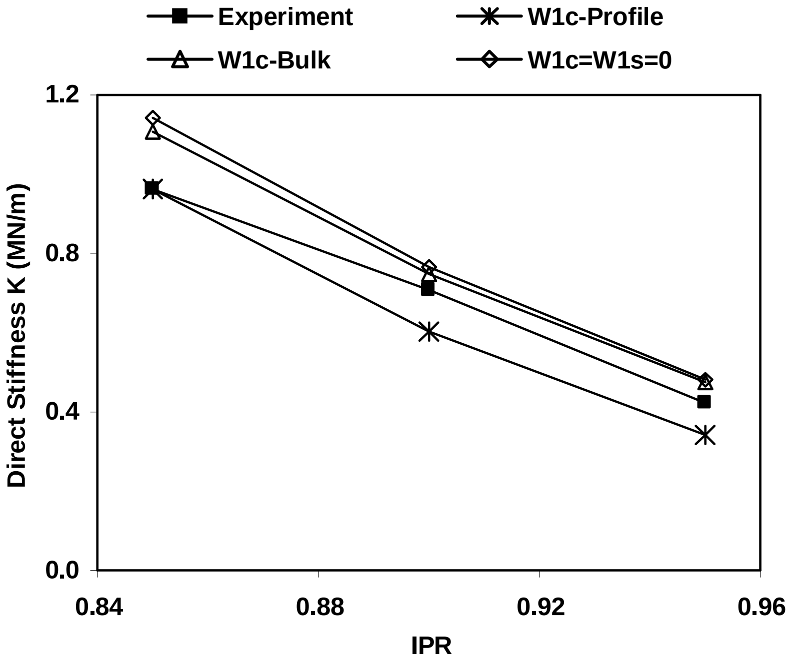

(b) ω = 8640rpm; $PR(P_L/P_H) = 0.65$

Fig. 28. Comparison with measurements (Soto, 1999) of predicted direct stiffness K using various seal-inlet, flow-disturbance boundary conditions; PR=0.65.

The W_{1C}-profile and W_{1C}-bulk correlation don't show any evidence as to which one is better in predicting the direct stiffness coefficients. This is not surprising due to the fact that the direct stiffness is only slightly influenced by W_{1C}, as noted earlier.

D. Summary

The benefits of using these boundary condition correlations were assessed using two very different seal test cases that have very different operating conditions. Case 1 is a test of the correlations for large axial-inlet upstream chambers employing a simple seal of smooth-plane configuration, and Case 2 is a test of the correlations for small axial-inlet, as well as radial injection, upstream chambers employing a complicated gas labyrinth seal. It was found that,

1. Considering how challenging the gas labyrinth test case is, the solutions using the new correlations with either the W_{1C}-profile option or the W_{1C}-bulk option agree well with the measurements.
2. For the liquid and the gas seals considered, improved agreement with measurements was generally obtained for the options with non-zero W_{1C} and W_{1S} compared to the option with $W_{1C} = W_{1S} = 0$.
3. The correlation set with the W_{1C}-profile option gave almost the identical prediction as that with the W_{1C}-bulk option for the liquid annular seal.
4. For the gas labyrinth seal, the correlation set with the W_{1C}-profile option gave a better prediction of C_{eff} and k than that with the W_{1C}-bulk option. For CFD-perturbation models and full 3-D CFD models, the W_{1C}-profile option is recommended. The W_{1C}-bulk option is appropriate for bulk models because they do not allow the radial distribution of any quantity.

5. One of the new findings from the 240 CFD-perturbation solutions constituting the parametric study is that the K is only slightly affected by W_{1C}. Thus it was not surprising that the $W_{1C} = W_{1S} = 0$ option gives good predictions for K.

CHAPTER VI

INFLUENCE OF TEETH DAMAGE ON ROTORDYNAMIC INSTABILITY

This chapter investigates the influence of labyrinth seal teeth damage due to rotor impacting on the performance and the rotordynamic characteristics of impeller eye seals in centrifugal compressors. A well-established CFD-perturbation model was employed to predict the seal rotordynamic coefficients. The inclusion in the CFD domain of at least an approximate shroud leakage path chamber is preferred for an accurate prediction of seal-inlet swirl velocity and flow-induced rotordynamic forces. Specifically, impeller eye seals with teeth damage were explored to determine: (a) their leakage increases due to the increased seal clearance and (b) their seal-inlet swirl velocity as well as larger rotordynamic forces, which tend to cause the system to become unstable. The effect of distorted teeth tip geometries on leakage and rotordynamic coefficients for a given seal radial clearance was also explored. The leakage path influence on seal-inlet swirl velocity W_0 and the effect of W_0 on the rotordynamic forces were also explored to thoroughly understand the rotordynamic characteristics of the eye seal subject to various degrees of teeth damage.

A. Introduction

Seal teeth damage in rotating machinery is a serious concern and could happen throughout the service life due to seal rubbing, erosion, or fatigue. Damage from rotor impacting and/or intense rubbing is the most frequently encountered type of damage, and it occurs when the rotor vibration amplitude exceeds the seal clearance. Labyrinth seals with teeth damage can change the machine rotordynamics, leading to a decreased level of efficiency, an increased rotor runout, and sometimes, a catastrophic failure of the machine. In addition, seal teeth damage accelerates the effects of both erosion and fatigue by wearing away protective coatings or distorting cooling passages that include the teeth tips.

Because of its destructive characteristics, extensive research efforts have been undertaken since the early work of Newkirk on rubbing damage in 1926: (a) to better describe the damage mechanisms and (b) to determine more reliable designs of rotating machinery. Most studies in rubbing damage have focused on the mechanical depiction of contact and rub generated vibration. As pioneers of rubbing research, Black [55] explained the rubbing physics when a rotor contacts a stator and Erich [56] proposed a model to predict the response of rotor and stator numerically. A well-cited literature survey on rubbing can be found in Muszynska [57] in which several physical phenomena were described during rotor/stator rubbing such as friction, impact, torsional load, thermal effect, and rotordynamic variation.

Seal rotordynamic force variation, specifically the rotordynamics of impeller eye labyrinth seals subject to rub damage, has received little attention. Sudden load changes of a centrifugal compressor, for example, could generate severe rubs of the labyrinth and cause the teeth tips to flatten out, which increases the radial clearance and creates undesirable flow characteristics across the labyrinth. These factors are detrimental to a compressor's efficiency and rotordynamic stability. In addition, higher differential pressure and hence larger thrust loading of the machine will arise from an excessive gas leakage from the discharge end seal [9]. Furthermore, the possibility of rubbing damage due to force/thermal imbalances increases with reduced seal clearance and increasing running speed. Therefore, an accurate prediction of performance deterioration and rotordynamic force variation during off-design operational conditions is necessary to estimate the dynamic behavior and to avoid rotor vibrations. [42] studied the seal clearance effects on spiral vibrations due to rubbing and showed that an increased clearance could improve the system's stability, in particular with regard to unstable spiral vibrations. The influence of leakage path inlet swirl on annular seal rotordynamics was experimentally investigated by [43] and [44] with water as the working fluid. A destabilizing effect was found arising from increasing inlet swirl for both normal and tangential forces. More recently, Wilcox and O'Brien [9] presented an in-depth fault diagnosis of stability problems in a centrifugal compressor and identified the rub-damaged buffer gas seals as the root cause for the persistent and worsening rotor vibrations. The issue of rotordynamic force variation of gas labyrinth seals with teeth damage, however, still remains untouched.

The objective of this portion of the overall investigation is to present a numerical analysis on this issue, as well as to gain insight into the mechanism that promotes the rotordynamic variations for different teeth damage conditions. The results should provide useful information for impeller eye seal design or fault diagnosis of stability problems in centrifugal compressors.

B. Numerical Method

The well-tested CFD-perturbation rotordynamics model described in Chapter III was employed in this study. Firstly, the zeroth-order equations are solved for a seal rotor in the centered position within the housing. Secondly, the disturbed variables are obtained from the first-order equations to account for a very small rotor displacement (*i.e.* perturbation). Thirdly, by integrating the pressure around the rotor circumference within the seal the flow-induced forces on the rotor are obtained. Further details can be found in Chapter III. The SIMPLEC algorithm was used in the present study in combination with the QUICK differencing scheme for the convection terms to minimize the numerical diffusion.

This CFD-perturbation model was validated by comparing with measurements of a liquid annular seal [53] and a gas labyrinth seal with shunt injection [54]. Excellent agreement was obtained for rotordynamic coefficients in both the tangential and radial directions.

1. CFD Considerations

Sealing in a typical compressor includes shaft seals, impeller eye seals, and balance piston seals. The impeller eye labyrinth seals are of major rotordynamics concern due to their diameter and the swirling leakage flow coming from the tip of the impeller. Figure 29 shows the schematic diagram of a typical impeller eye seal with damaged teeth. The layout of the leakage path chamber and labyrinth seal cavities are given in Figs. 29 (a) and (b). The eye labyrinth seal consists of a small rotor surface and a stator with 5 teeth on it. The "mushroomed" teeth tips due to rubbing damage are approximated by flat caps as illustrated in Fig. 29 (c). Various teeth damage conditions and teeth tip shapes were investigated concerning their influence on the eye seal's leakage and stability. The geometrical details and operating conditions of the considered rub-damaged seals are summarized in Table VI.

Air was used as the working fluid. The rotor running speed was 6,000 rpm. Inlet swirl velocity and pressures upstream and downstream of the impeller eye seal were specified as boundary conditions. The leakage path inlet swirl ratio, Γ (*i.e.* the ratio of the leak path chamber inlet circumferential velocity to the impeller rotation speed) was specified as 0.6, which is widely adopted in industrial applications. The leakage path upstream pressure was 13.77 bar, with a pressure ratio (*i.e.* the ratio of downstream pressure to upstream pressure) of 0.71. On the rotor and stator walls, no-slip surface conditions were specified via standard wall-functions. The near wall computational cells have y^+ within the range from 15 to 90 on near-rotor surfaces throughout the whole seal.

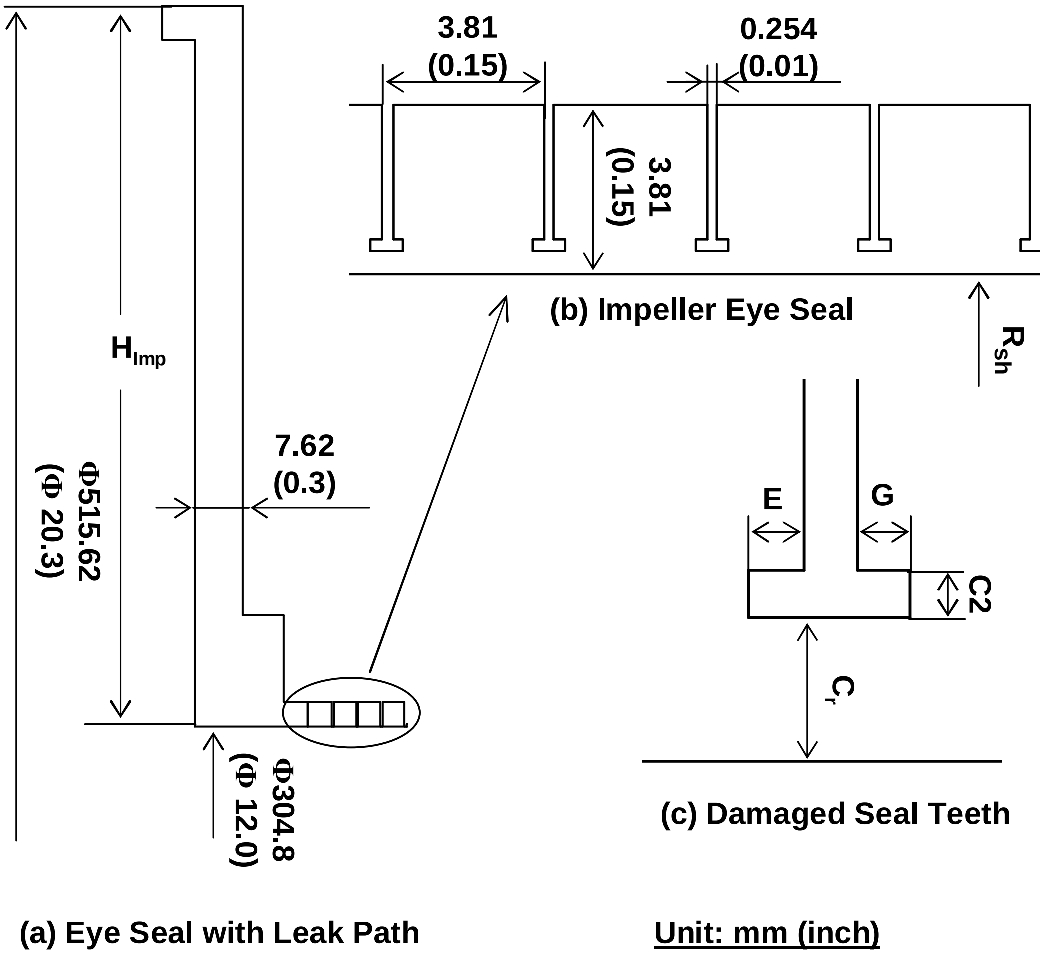

Fig. 29. Dimensions of impeller eye seal with leak path channel and damaged teeth tips: (a) leak path channel; (b) impeller eye seal; (c) damaged seal teeth.

Table VI. Dimensions of Damaged Eye Seal Teeth Tips

Case name	C_r (mm)	E (mm)	G (mm)	C2 (mm)
B1	0.254	0	0	N/A
B2	0.381	0.127	0.127	0.127
B3	0.508	0.254	0.254	0.127
B4	0.635	0.381	0.381	0.127
B5	0.762	0.508	0.508	0.127
D1	0.762	0	0	N/A
D2	0.762	0.254	0.254	0.254
D3	0.762	0	0.508	0.254
D4	0.762	0.508	0	0.254
D5	0.762	0.508	0.508	0.127

2. Grid Independence Study

Grid independence testing was performed for a typical eye seal at two seal clearances, *i.e.* $C_r = 0.254$ mm and 0.762 mm, respectively. Three grids were tested for each clearance as shown in Table VII. Grid independence was achieved for leakage, seal-inlet swirl and rotordynamic coefficients at 284 × 201 for $C_r = 0.254$ mm and 270 × 213 for $C_r = 0.762$ mm; the grids were used as the production grids. Very small deviations were obtained with the maximum discrepancy of 4.43% from direct stiffness coefficient (see Table VII).

C. Eye Seal Rotordynamics with Damaged Teeth

The magnified vector plots for the leakage path chamber and labyrinth seal cavities are presented in Fig. 30. A long, radially extended recirculation zone is found inside the leakage path chamber, with the downward main flow region near the stator and the reversal flow region near the rotor. Numerical integration of the radial velocity distribution across the leakage path shows that the mass flow ratio of the downward flow to the reversal flow is approximately 3:1.

1. Rotordynamics Variation with Increasing Damage

Rotor impacting on the labyrinth teeth increases the seal radial clearance and distorts the seal teeth-tips. Cases $B1$ to $B5$ in Table VI give the dimensions of the distorted teeth tips subject to the assumed increasing damage considered in this study.

a. Leakage and Seal-Inlet Swirl

Figure 31 shows the predicted leakage rate and the seal-inlet swirl velocity at different damage conditions for a rotor spin speed of 6,000 rpm, a leakage path inlet swirl ratio

Table VII. Grid Independence Testing Results

C_r	NI×NJ	m	$\frac{(m_c - m_f)}{m_f}$	W_0	$\frac{(W_{0c} - W_{0f})}{W_{0f}}$	k	$\frac{(k_c - k_f)}{k_f}$	C	$\frac{(C_c - C_f)}{C_f}$	K	$\frac{(K_c - K_f)}{K_f}$
(mm)		(kg/s)	(%)	(m/s)	(%)	(MN/m)	(%)	(KNs/m)	(%)	(MN/m)	(%)
0.254	224×159	0.3145	−−	99.58	−−	4.346	−−	1.070	−−	1.419	−−
	284×201	0.3138	0.23	99.46	0.12	4.368	-0.52	1.063	0.69	1.444	-1.72
	375×262	0.3139	-0.04	99.29	0.17	4.370	-0.05	1.062	0.09	1.386	4.19
0.762	235×166	1.321	−−	142.73	−−	0.5821	−−	1.070	−−	0.4017	−−
	270×213	1.316	0.34	141.19	1.09	0.5654	2.95	1.050	0.93	0.3847	4.43
	394×271	1.313	0.28	140.94	0.18	0.5576	1.41	1.041	0.82	0.3794	1.34

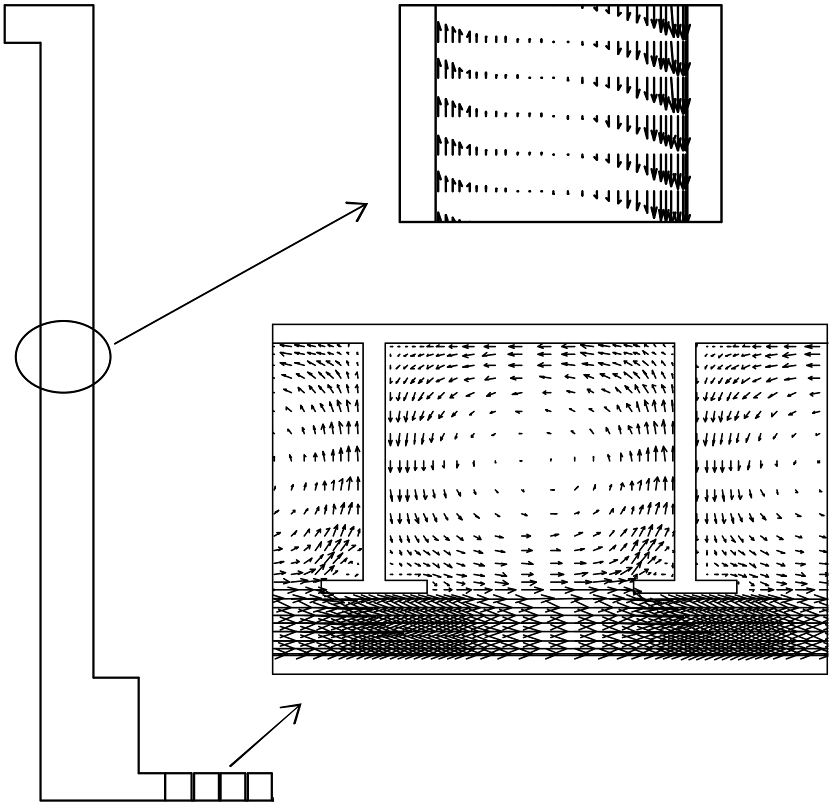

Fig. 30. Flow pattern for impeller eye seal with leak path channel.

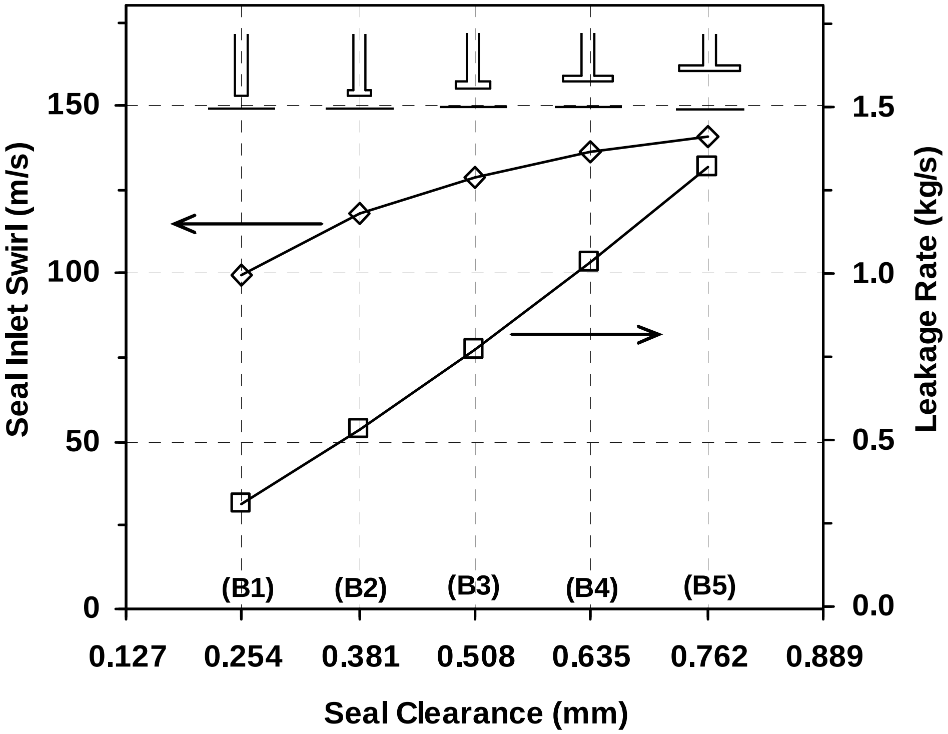

Fig. 31. Predicted leakage rate and seal-inlet swirl velocity at increasing teeth damage for impeller eye seal with leak path chamber.

of 0.6, and a pressure ratio of 0.71. It is found that the gas leakage rate increases approximately linearly with the increasing seal clearance. From the present results, a leakage increase of approximately 319.5% is expected for a damaged eye seal with a clearance of 0.762 mm, as compared to the undamaged seal (*i.e.* $C_r = 0.254$ mm). From Fig. 31, one can also find that the resultant seal-inlet swirl velocity W_0 increases with increasing leakage, but at a much lower rate than that of the leakage. Specifically, W_0 increases faster during the initial stage of teeth damage, *i.e.* 18.8% variation from *B1* to *B2*. Afterwards, the increase rate decreases, *e.g.* with only an increase of 3.6% from *B4* to *B5*. For a given seal with increasing teeth damage, the fact that W_0 increases in an asymptotic manner is attributed to the asymptotic behavior of the ratio of near-wall friction torque to the change of angular momentum (*i.e.* $rF_\theta / \int rW\rho\vec{V} \cdot d\vec{A}$), which will be elaborated on in Section VI.E.

Usually the gas labyrinth seal clearance is quite tight by design to limit the amount of gas leakage. Teeth damage to such seals is expected to allow excessive gas leakages that could considerably deteriorate the compressors' performance.

b. Rotordynamic Force Coefficients

Figures 32 and 33 show the predicted rotordynamic force coefficients k, C, C_{eff}, and K of the eye seal at different damage conditions for the same conditions as in Fig. 31. The variation of cross-coupled stiffness k with different damage conditions is somewhat unexpected. Instead of a decline with increasing seal clearance, k increases monotonically in magnitude from *B1* (*i.e.* $C_r = 0.254$ mm) to *B3* (*i.e.* $C_r = 0.508$ mm), reaches a maximum around *B3*, and then steadily declines at a slower rate (see Fig 32 (a)). The reverse trend was also observed for effective damping C_{eff} in Fig. 33 (a), which decreases rapidly from *B1* to *B2* and then recovers somewhat at a reduced rate. Essentially, a dramatic decrease in C_{eff} occurs during the initial teeth

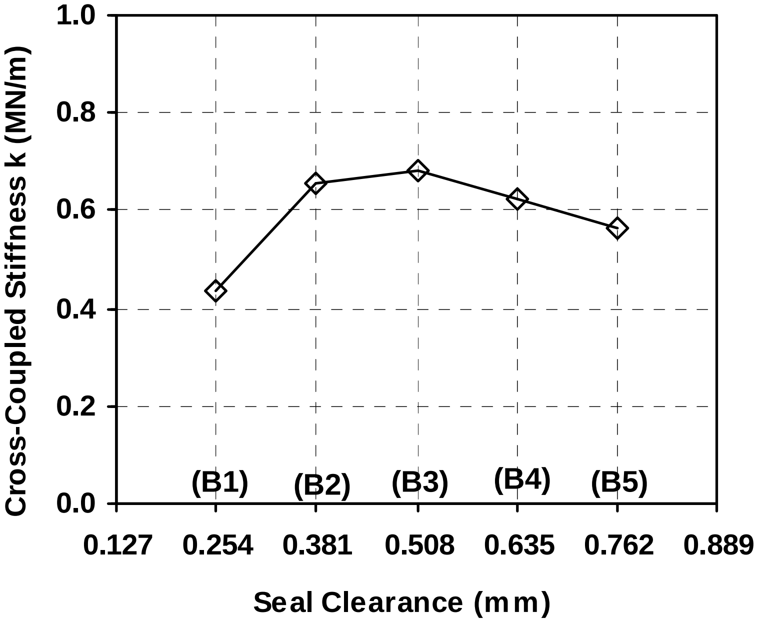

(a) Cross-Coupled Stiffness, k

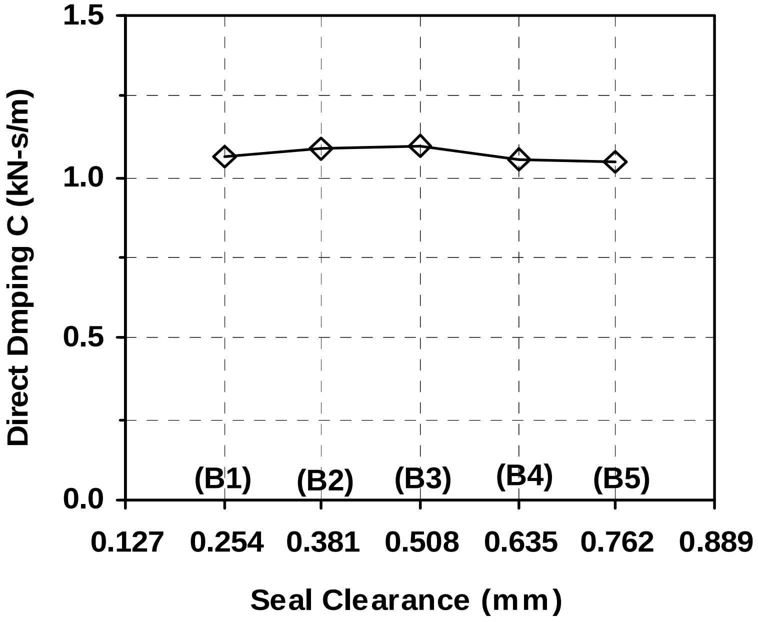

(b) Direct Damping, C

Fig. 32. Predicted dynamic force coefficients at increasing teeth damage for impeller eye seal with leak path chamber: (a) cross-coupled stiffness, k; (b) direct damping, C.

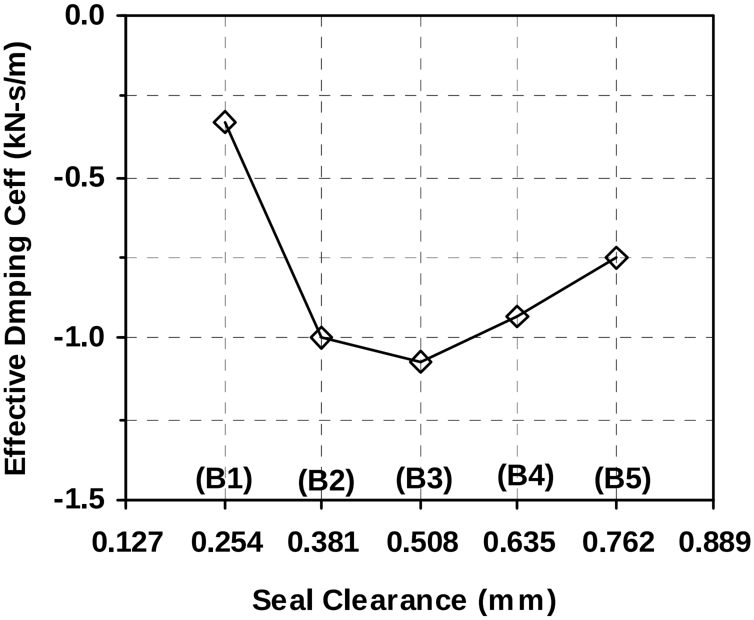

(a) Effective Damping, C_{eff}

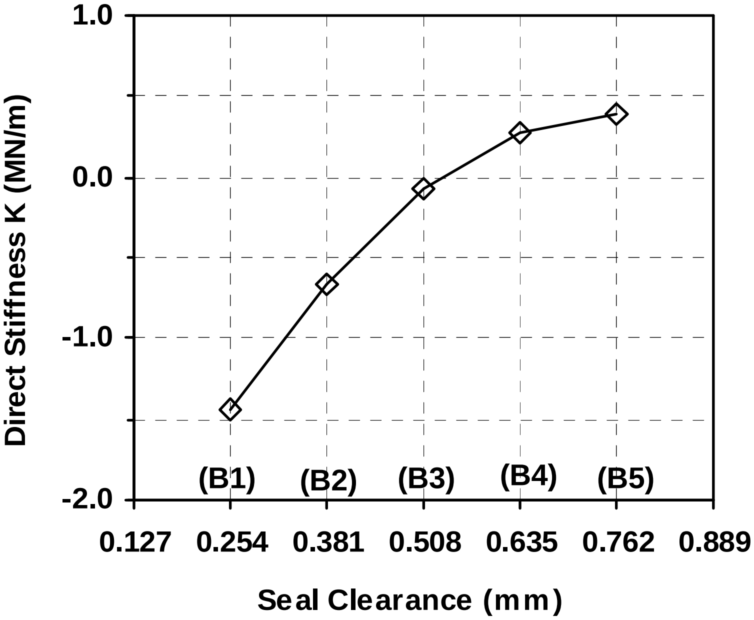

(b) Direct Stiffness, K

Fig. 33. Predicted dynamic force coefficients at increasing teeth damage for impeller eye seal with leak path chamber: (a) effective damping, C_{eff}; (b) direct stiffness, K.

damage, *i.e.* about 200% from *B1* to *B2* (*i.e.* $C_r = 0.381$ mm). The effective damping here has negative values, which represents a net destabilizing force. Values of C_{eff} that are increasing negative produce larger destabilizing forces and could drive the rotor-seal system unstable. Furthermore, rub-damaged seal teeth experience thermal distortion, which could exacerbate the rub and cause further damage. Interestingly, further damage didn't worsen the system's stability for $C_r > 0.508$ mm, but improved it somewhat. In his work concerning clearance effects on spiral vibrations [42], Childs showed that a widened clearance due to rubbing could help the system's stability, especially for unstable spiral vibrations. Childs' results are generally in support of the present results. The peaking behavior of both k and C_{eff} is actually resulting from the competing effects of the increasing W_0 due to the increased clearance and the stabilizing effects from the enlarging seal clearance as the damage grows worse. The stability deteriorates when the W_0 destabilizing effect dominates and will improve when the clearance effect dominates. Viewing Childs' results as the case where the clearance effect dominates, the results here are more inclusive when the impeller eye seal is of concern. The stabilizing effects due to the enlarging clearance will be further discussed in Section VI.D.

Fig. 32 (b) shows that the direct damping coefficient C remains almost unchanged for the different damage conditions. The direct stiffness coefficient K was found to increase continuously in an asymptotic way as the damage grows worse (see Fig. 33 (b)).

2. Influence of Deformed Teeth-Tip Shapes

Distinct teeth tip shapes have been found at the damage location depending on the wearing mechanism. Table VI gives dimensions of each deformed seal configuration (*D1* to *D5*) investigated in this study, all of which are of the same clearance (*i.e.* C_r

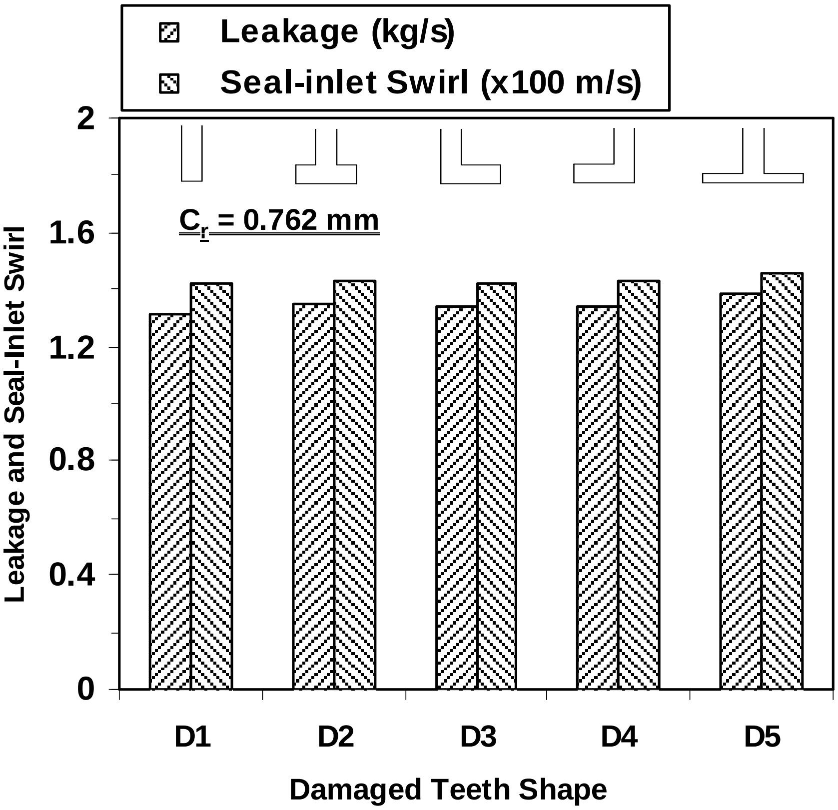

Fig. 34. Effect of damaged seal teeth tip shape on leakage and seal-inlet swirl.

= 0.762 mm). Figure 34 shows the influence of the teeth shapes on leakage and seal-inlet swirl velocity. In general, a small difference in leakage and seal-inlet swirl was found for different seal teeth configurations. The maximum variation of the leakage rate is around 5.1% and that of the seal-inlet swirl velocity is only 2.3%, with shape *D1* giving both the minimum leakage and minimum W_0, while shape *D5* gives both the maximum values, as illustrated in Fig. 34.

Figure 35 shows that shape *D1* (see top of Fig. 35) produces the largest destabilizing force, *i.e.* negative effective damping, among the five deformed shapes, while shape *D5* produces the least destabilizing force. The C_{eff} discrepancy between these two shapes is about 15%. The maximum variation for the direct stiffness K is about

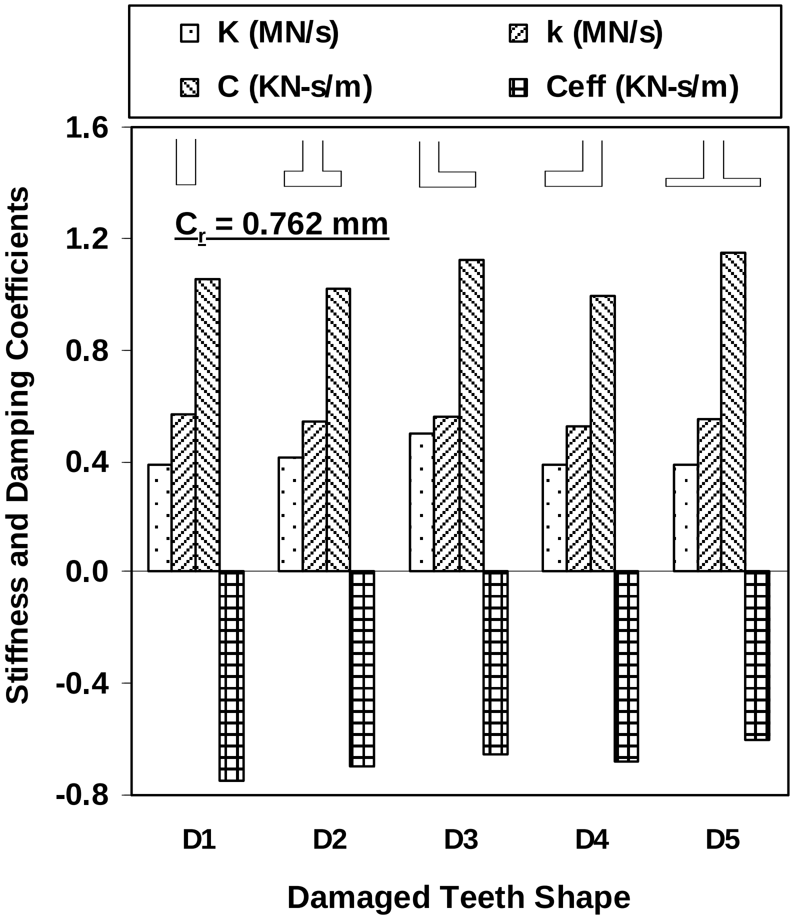

Fig. 35. Effect of damaged seal teeth tip shape on flow-induced force coefficients.

17%. It is concluded that the deformed teeth shapes do have a certain influence on the impeller eye seal rotordynamic forces, but it is not of significant consequence.

Comparing the magnitude of C_{eff} (evaluated from assuming $\Omega = 0.5\omega$) in Fig. 35 for the teeth tip shapes considered reveals that there is a slight variation of stability among these damaged teeth tip shapes.

D. Isolated Eye Seal Rotordynamics

An analysis has been undertaken to gain insight into the seemingly erratic rotordynamic variations with teeth damage. Emphasis has been placed on the leakage path influence on the seal-inlet swirl W_0 and the rotordynamic variation of an isolated seal (*i.e.* without leakage path chamber) with W_0. In this section by means of parametric study of W_0 and C_r, it will be shown how an isolated eye seal responds to seal-inlet swirl at different seal clearances, or equivalently at different damage conditions (because of the insignificant effect of teeth tip shapes for a fixed clearance) as discussed in the previous section.

Figures 36 and 37 give the variation of the predicted dynamic force coefficients with W_0 at different seal clearances for a running speed of 6,000 rpm and a pressure ratio of 0.71. One can see that both k and C_{eff} exhibit a nearly linear dependence on the seal-inlet swirl W_0. Further, all three C_{eff} profiles in Fig. 37 (a), as well as k profiles in Fig. 36 (a), intersect at one point where W_0 approximately equals the rotor peripheral speed ωR_{sh}. The effective damping C_{eff} indicates stabilization of the rotor when $W_0 < \omega R_{sh}$ and excitation of the rotor when $W_0 > \omega R_{sh}$.

Observing the varying profile slopes of both k and C_{eff} in Fig. 36 (a) and 37 (a), it is concluded that the stability characteristics of an eye seal with tighter clearance is more sensitive to seal-inlet swirl than a seal with looser clearances. Given the same

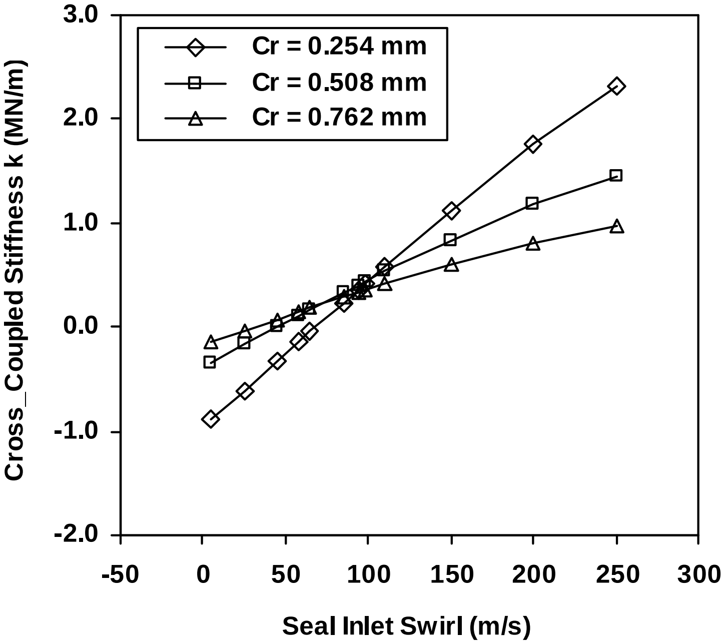

(a) Cross-Coupled Stiffness, k

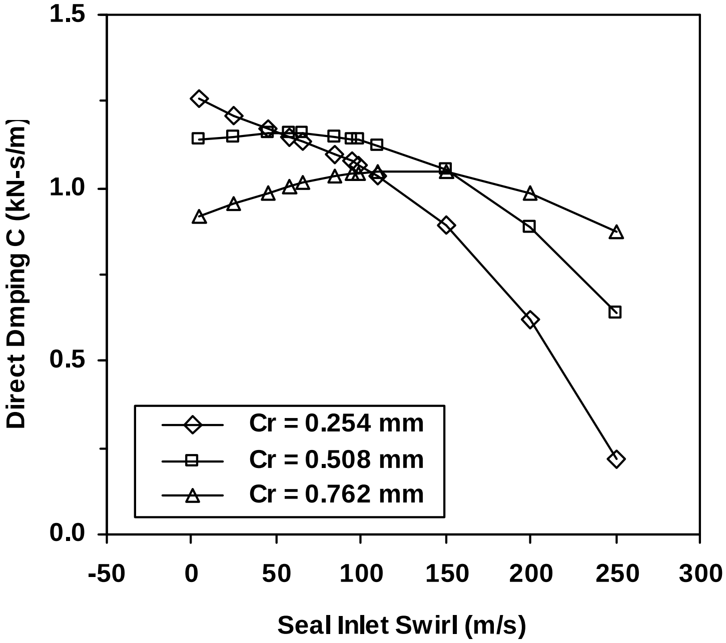

(b) Direct Damping, C

Fig. 36. Predicted dynamic force coefficients vs. seal-inlet swirl velocity at different teeth clearances: (a) cross-coupled stiffness, k; (b) direct damping, C.

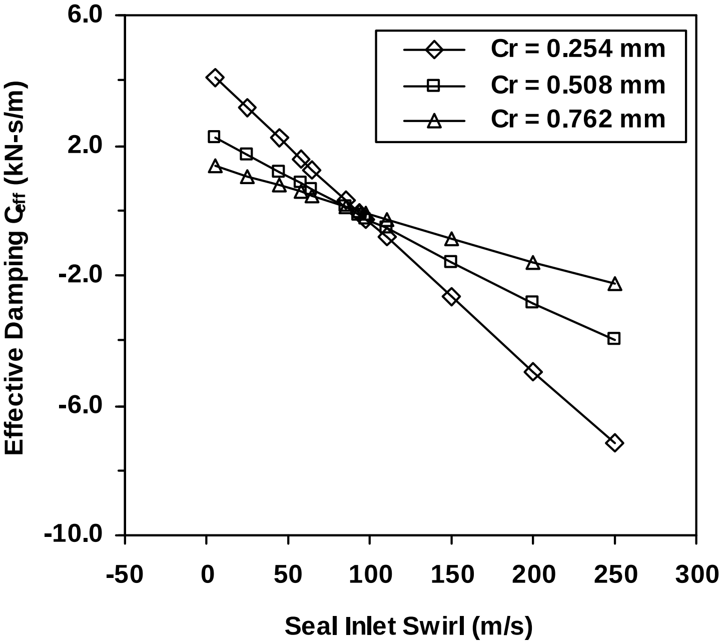

(a) Effective Damping, C_{eff}

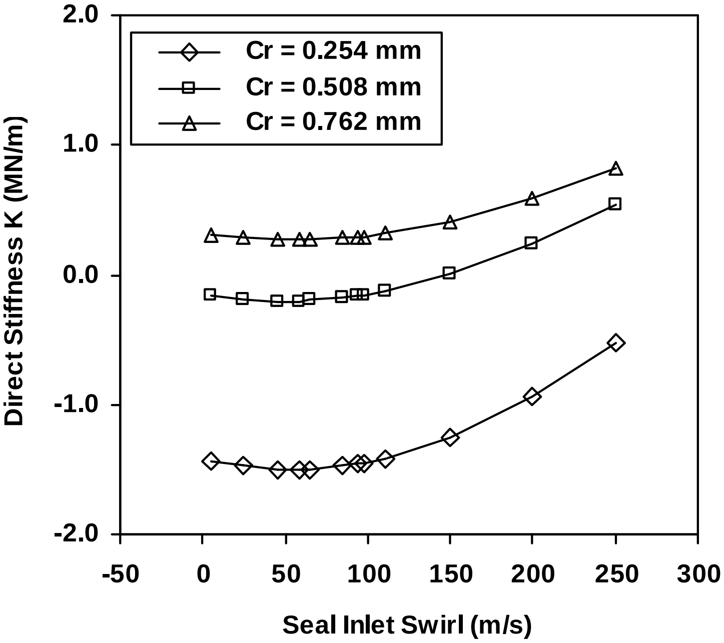

(b) Direct Stiffness, K

Fig. 37. Predicted dynamic force coefficients vs. seal-inlet swirl velocity at different teeth clearances: (a) effective damping, C_{eff}; (b) direct stiffness, K.

operational conditions, larger rotordynamic forces will be induced within a tighter clearance eye seal.

On the other hand, the W_0 effect on direct stiffness K and direct damping C is far from linear, as shown in Figs. 37 (b) and 36 (b). It is also noticed from Fig. 36 (b) that the variation of direct damping with seal-inlet swirl differs considerably at different seal clearances. Much greater sensitivity of C to W_0 is sighted at $C_r =$ 0.254 mm than those at $C_r = 0.508$ mm and $C_r = 0.762$ mm. The magnitude of C decreases monotonically with increasing W_0 except at $C_r = 0.762$ mm, which reaches a maximum around $W_0 = 140$ m/s and then slightly declines. All the direct damping coefficients are positive, which acts against the whirl direction. Again, the direct damping was found to offset a portion of the destabilizing effect of the cross-coupled stiffness force for gas labyrinth seals with high running speed.

Direct stiffness K demonstrates large sensitivity to seal clearance, with less sensitivity to W_0, especially for large clearances such as 0.508 and 0.762 mm. Moreover, the tighter the seal clearance, the higher sensitivity K demonstrates to the variation of C_r, and of W_0 as well.

E. Leakage Path Influence on W_0

In practice, the seal-inlet swirl is not readily known and could be extremely difficult to measure due to the leakage path geometry limitation upstream of the seal inlet. The ability to evaluate W_0 developed by the shroud leakage flow is essential for an accurate prediction of rotordynamic stiffness and damping coefficients for impeller eye seals. The flow field inside the leak path is very complex as depicted in Fig. 30. Its influence on W_0 is supposed to be heavily dependent on leakage path geometry, operational conditions, and fluid properties. The angular momentum conservation is governed by,

$$\vec{r} \times \vec{F}_{sh} + \int \vec{r} \times \vec{g}\rho dv + \vec{T}_{sh} = \frac{\partial}{\partial t}\int \vec{r} \times \vec{V}\rho dv + \int \vec{r} \times \vec{V}\rho\vec{V} \cdot d\vec{A} \tag{6.1}$$

Based on the assumptions of steady flow, uniform velocity and density with negligible shaft torque, the angular momentum conservation in the shaft axis direction can be simplified as,

$$rF_\theta = \int rW\rho\vec{V} \cdot d\vec{A} \tag{6.2}$$

For ideal fluid flow, the above equation reduces to the ideal angular momentum conservation, *i.e.* $r_1W_1 = r_2W_2$, which raises the bulk swirl velocity (across the leakage path) as the leakage flow goes radially inward within the leakage path chamber.

The left- and right-hand-side terms in Eq. (6.2) are the circumferential component of net shear friction and the change of angular momentum, respectively. For a particular leak path chamber geometry, the circumferential velocity exiting from the leakage path chamber is mainly determined by the left-hand side. The leakage path inlet angular momentum is proportional to the product of leakage path inlet swirl and impeller tip radius. From Eq. (6.2), it is evident that the leakage path inlet swirl ratio Γ $(= W/(R_{sh} + H_{Imp})\omega)$, rotor spin speed ω, impeller height H_{Imp}, and shaft radius R_{sh} all have the potential to alter the inlet momentum. The shear friction term is mainly determined by the near wall swirl gradients, the radius, and the fluid residence time within the leakage path. Two unevenly divided flow regions exist inside the leakage path with a large radially inward flow region near the stator and a small outward flowing region near the rotor, as shown in Fig. 30. Accordingly, the friction contribution from these two regions should be different in affecting the fluid circumferential velocity, and it largely depends on the flow ratio. Therefore, it is useful to propose a virtual swirl velocity termed "neutral swirl, W_{Neu}" which could incorporate the friction effects from both walls such that the net friction effect vanishes when the fluid circumferential velocity equals the neutral swirl.

Figure 38 shows the variation of the predicted seal-inlet swirl velocity W_0 with leak path inlet swirl ratio at three different teeth damage conditions for a rotor spin speed of 6,000 rpm, and a pressure ratio of 0.71. Comparison of the W_0 profiles for the three damage conditions (solid lines) reveals that higher W_0 is generally expected for an eye seal with greater teeth damage. This is because the shear friction effect becomes less important for seals with increasing clearance, and hence the swirl velocity is more determined by the leak path inlet angular momentum, which has a tendency to increase the swirl velocity. Again, greater changes of W_0 were observed during the initial damage stages (*i.e.* C_r from 0.254 mm to 0.508 mm) than subsequent stages (*i.e.* C_r from 0.508 mm to 0.762 mm).

Also plotted in Fig. 38 is the ideal vortex at the seal inlet calculated from the relation $R_{sh}W_0 = R_{Imp}W_{Imp}$. An interesting behavior was observed near $\Gamma = 0.25$ such that all three seal-inlet swirl profiles as well as the ideal vortex intersect. The resultant seal-inlet swirl is greater than the ideal vortex when Γ is less than 0.25, whereas it is less than the ideal vortex when Γ is larger than 0.25. This implies that the swirling flow is accelerated by the near-wall friction when $\Gamma < 0.25$, while is slowed down when $\Gamma > 0.25$. Therefore, it can be concluded that for the present geometry and conditions the neutral swirl W_{Neu} is approximately 0.25 times the local impeller rotational speed. This is in agreement with the fact that the inward-to-outward mass flow ratio is about 3:1 as has been discussed previously in Section VI.A. In addition, the neutral swirl at the leakage path inlet was plotted in Fig. 38 (dotted line) only to show, as the authors expected, that it crosses the leakage path inlet swirl profile at approximately $\Gamma = 0.25$.

Figure 39 shows the radial profile of the bulk (axial-direction average) swirl

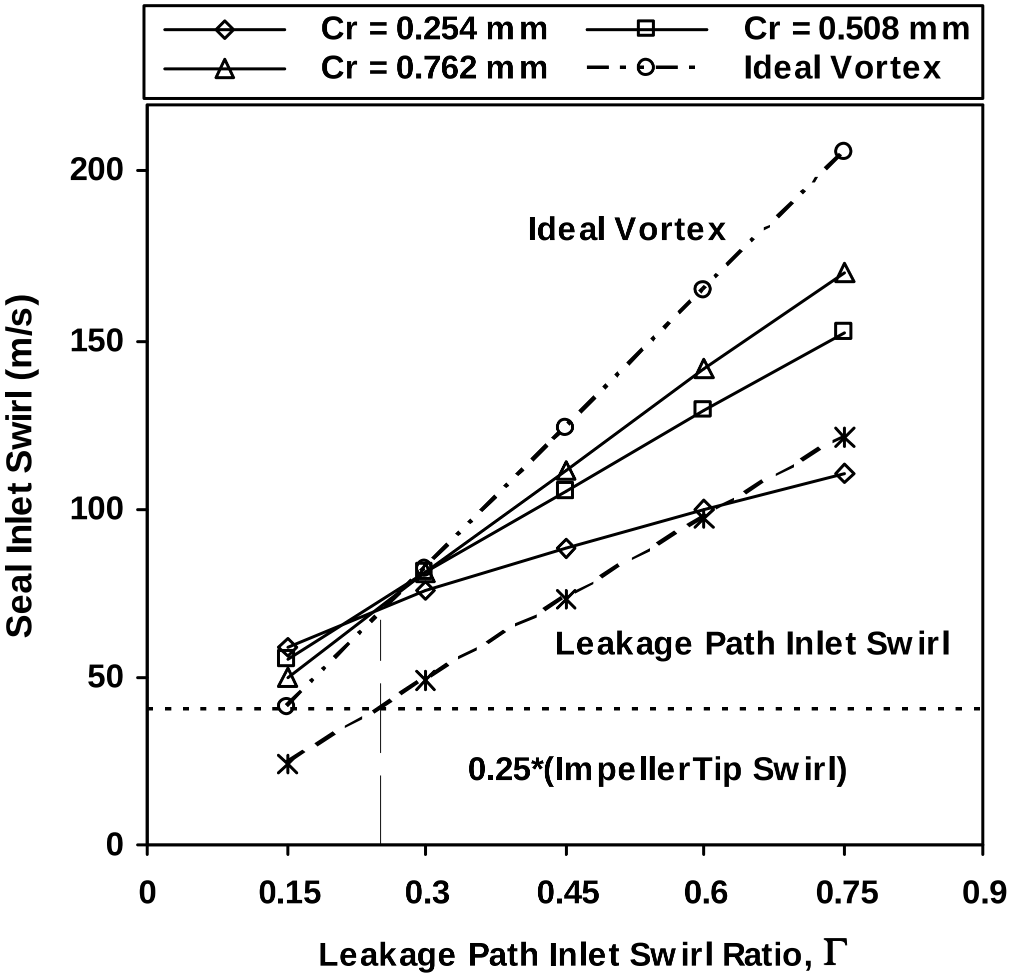

Fig. 38. Predicted seal-inlet swirl velocity vs. leak-path inlet swirl ratio Γ $[W/(R_{sh} + H_{Imp})\omega]$ in an impeller eye seal with leakage path.

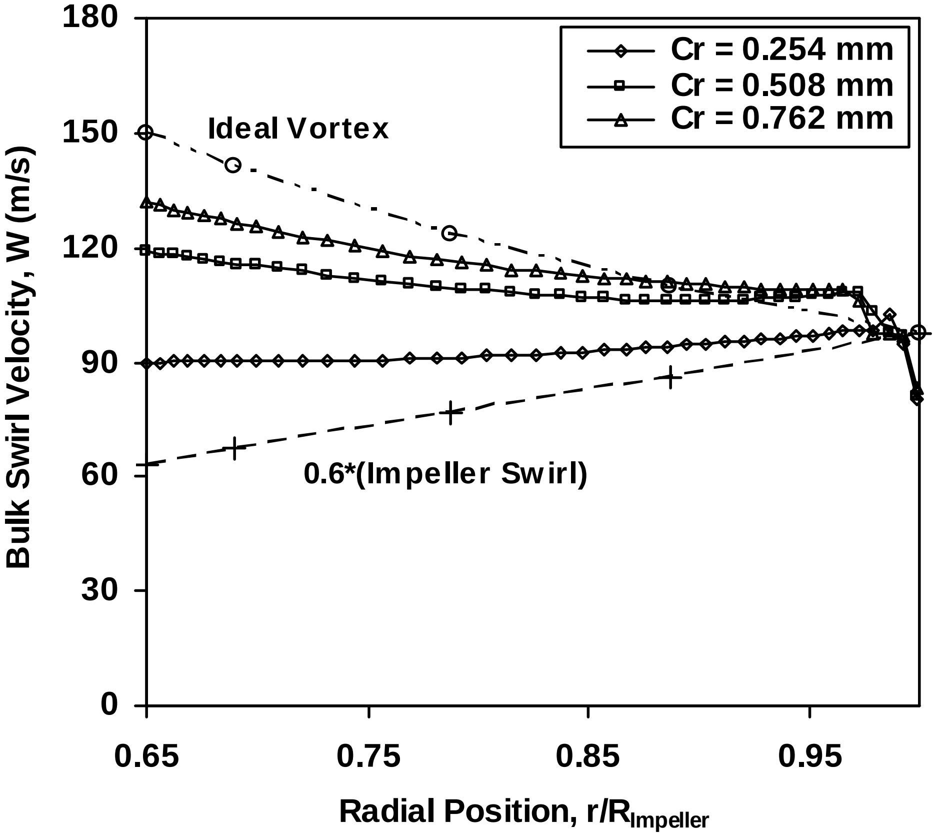

Fig. 39. Radial profile of bulk swirl velocity within leakage path chamber, leak-path inlet swirl ratio = 0.6.

velocity along the leakage path chamber for the same conditions as in Fig. 38 except that the leakage path inlet swirl ratio is fixe at 0.6. Persistent higher bulk swirl was observed along the leakage path for enlarged seal clearances than for tight ones, as has been also observed in Fig. 38. As expressed in Eq. (6.2), the swirl velocity is the competition result between the swirl increase tendency of the rotor wall shear forces and the radially inward flow of the leakage throughflow jet versus the swirl decrease tendency of the stator wall shear forces. These are strongly influenced by the fluid residence time as well as the near-wall swirl difference $[W - W_{Neu}]$. A seal with a tight clearance permits less gas leakage and therefore has a longer fluid residence time. Such a long residence time indicates that a fluid particle of the seal leakage throughflow travels around the circumference near the stator wall, as shown in Fig. 30, more times. Apparently this increased travel distance exerts a sufficiently increased swirl-resisting force on the particle that reduces its swirl velocity upon exiting the leak path chamber. Likewise, a seal with an increased clearance due to teeth damage experiences a much shorter residence time and ends up with higher swirl velocity. In industrial practice, the swirl ratio (*i.e.* the ratio of the local fluid bulk circumferential velocity to the local impeller rotation speed) of $0.6 \sim 0.65$ is typically assumed along the shroud leakage path chamber. Comparison of this empirical swirl (dashed line) with numerical predictions (three solid lines) shown in Fig. 39 indicates that the assumption of a constant ratio, e.g. 0.6, assumes larger friction than the numerical results here. Further, it is too crude to represent the variations of seal geometries and conditions, and presumably cannot give an accurate prediction of rotordynamic forces for a given test case.

Depicted in Fig. 40 (a) and 40 (b) are the variations of the predicted seal-inlet swirl velocity with impeller height ratio (*i.e.* H_{Imp}/R_{sh}) and running speed respectively, with $\Gamma = 0.6$, $\omega =$ 6,000 rpm, and the pressure ratio remaining the same

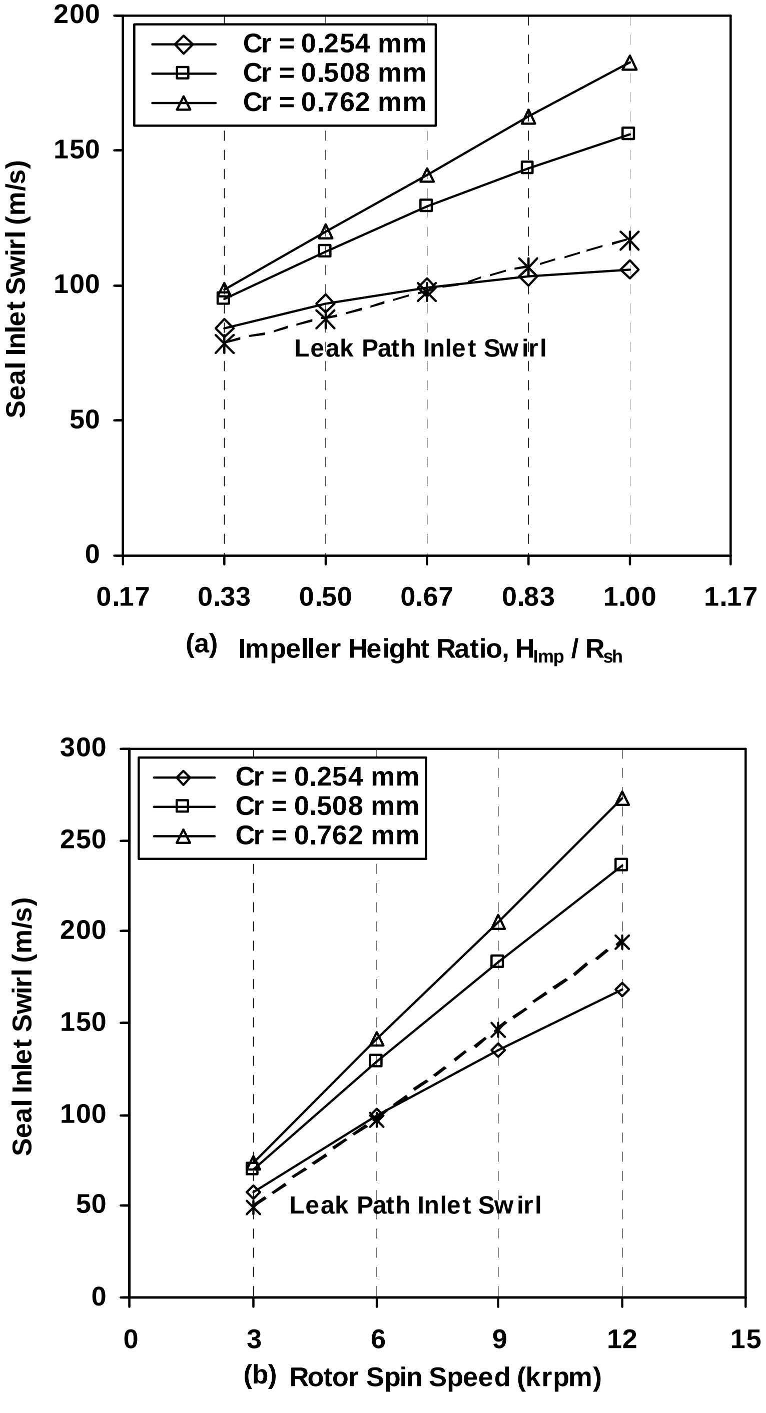

Fig. 40. Predicted seal-inlet swirl velocity vs. impeller height and running speed at different seal teeth damage conditions: (a) impeller height ratio, HImp/Rsh; (b) rotor spin speed.

Table VIII. Leak Path Width A Influence on Seal-Inlet Swirl

$Case$	A (mm)	$C_r = 0.254mm$		$C_r = 0.508mm$		$C_r = 0.762mm$	
		W_0 (m/s)	$\frac{(W_i - W_{i+1})}{W_{i+1}}$ (%)	W_0 (m/s)	$\frac{(W_i - W_{i+1})}{W_{i+1}}$ (%)	W_0 (m/s)	$\frac{(W_i - W_{i+1})}{W_{i+1}}$ (%)
1	5.08	100.3	−−	129.6	−−	141.4	−−
2	7.62	99.5	0.79	129.0	0.47	141.2	0.12
3	10.2	99.5	-0.02	129.1	-0.08	141.3	-0.06
4	12.7	99.7	-0.17	129.4	-0.18	141.2	0.03

as in Fig. 38 and 39. A wide range of impeller heights were covered in Fig. 40 (a), ranging from very short impellers (*i.e.* $H_{Imp}/R_{sh} = 0.33$) to very long ones (*i.e.* $H_{Imp}/R_{sh} = 1.0$). From Fig 40 (a), one can also see that seals with larger radial clearances are more sensitive to the variation of the impeller radius than seals with tighter clearances. An increased sensitivity of large clearance seals to the runing speed is found in Fig. 40 (b) which covers running speeds from 3,000 rpm to 12,000 rpm with $H_{Imp}/R_{sh} = 0.67$. One difference is that the seal inlet swirl increase in Fig. 40 (b) is proportional to ω while the increase in Fig. 40 (a) follows a quadratic function of the impeller tip radius ($H_{Imp} + R_{sh}$).

An analysis of the influence of the leakage path width and pressure ratio on seal inlet swirl W_0 was also undertaken. The negligible effect of leakage path width as shown in Table VIII lends further support to the proposed W_0 mechanism because neither inlet angular momentum nor wall friction is affected by the leakage path width variation.

F. Summary

Extensive numerical studies were performed to investigate the influence of teeth damage on the performance and rotordynamic characteristics of compressor impeller eye seals using the CFD-perturbation modelling approach. The inclusion of at least an approximate shroud leakage path chamber is preferred for an accurate prediction of the seal-inlet swirl velocity W_0 and the rotordynamic forces. Parametric studies on the variations of the seal-inlet swirl with the presence of a leakage path and its influence on seal rotordynamics were performed. Specific findings include:

1. Impeller eye seals with damaged teeth suffer significant leakage increases due to the enlarged seal clearance from the teeth damage. Higher seal-inlet swirl arises from the increased leakage flow (*i.e.* a decreased particle residence time) through the leak path chamber which generates larger rotordynamic forces.

2. For a fixed seal clearance and operational conditions, various geometries of the distorted teeth tip have a negligible effect on: (a) leakage, (b) seal-inlet swirl and (c) rotordynamic force coefficients.

3. Seal teeth damage causes significant variations of seal-inlet swirl and rotordynamic force coefficients for tight seal clearances (*i.e.* $C_r = 0.254 \sim 0.381$ mm) and only slight variations for large seal clearances (*i.e.* $C_r = 0.635 \sim 0.762$ mm).

4. Considering a particular impeller eye seal combined with its shroud leakage path chamber, the seal-inlet swirl W_0 is primarily determined by the angular momentum of the leakage path inlet and the net circumferential friction force from the rotor and stator. An increase in leakage-path-inlet swirl ratio, impeller height, or running speed will raise the seal-inlet swirl velocity in an approximately linear fashion. The leakage path width has no discernable effect on W_0

because neither inlet angular momentum nor wall friction is affected by leakage path width variation.

5. Considering the present eye seal without its leak path chamber, the cross-coupled stiffness and effective damping vary almost linearly with seal-inlet swirl, while direct stiffness and direct damping vary in a much different fashion. In addition, the magnitude of the effective damping coefficient was found to be inversely proportional to the seal clearance.

6. The rule-of-thumb assumption that the leak path swirl ratio, *i.e.* the ratio of the local fluid swirl to the local impeller spin speed, is approximately $0.6 \sim 0.65$ along the shroud leakage path is too crude to accurately represent the effect of seal geometries and conditions. Because this rule-of-thumb gives an incorrect seal-inlet swirl velocity that is important for all seal rotordynamics models, it needs to be improved.

CHAPTER VII

INFLUENCE OF ROTOR AXIAL GROWTH ON ROTORDYNAMIC FORCES OF HIGH-LOW LABYRINTH SEALS IN STEAM TURBINES

Rotors in high-performance steam turbines experience significant axial shifting relative to the stator during transients due to thermal expansion as well as a net pressure load. This relative axial-shifting could significantly alter the flow pattern and the flow-induced rotordynamic forces in labyrinth seals, which in turn, can considerably affect the rotor-seal system's performance. This chapter investigates the influence of rotor-axial-shifting on the leakage rate as well as the rotordynamic forces in high-low labyrinth seals over a range of seal clearances and inlet swirl velocities. A surprisingly large effect was detected for rotordynamic characteristics due to changes in seal configuration caused by rotor shifting. It was also found that a less destabilizing effect arose from rotor axial shifting in the leakage flow direction, whereas a more destabilizing effect arose from shifting against the leakage flow direction. A tentative explanation was proposed for the large sensitivities of dynamic forces to off-design operations due to rotor-axial-shifting.

A. Introduction

Rotors in large steam turbines experience noticeable thermal, as well as net pressure load, axial growth during transient operations such as the start-up process. The rotor axial shifting caused by the thermal expansion could significantly alter the performance and rotordynamic forces of the labyrinth. The seal forces could contribute to the rotordynamic instability of the rotor-bearing-seal system even though the force magnitude is smaller than that of the bearing fluid film forces. As the rotating speed increases or the seal clearance decreases, the labyrinth-seal-excited problems often become more and more critical in the system design. It is therefore necessary to predict these forces accurately for both reliable operations and the future design of high-performance steam turbines.

Despite the exigency of this problem, experimental or numerical data addressing the effect of the rotor-axial-shifting on the seal rotordynamic characteristics is rare. Baumann [49] investigated the damping behavior for a high-pressure radial compressor and mentioned that axial rotor positions seemed to have insignificant influence on tangential forces and hence couldn't be verified as the root cause for the system instability. More recently, Wang et al. [50] studied the flow characteristics in stepped seals when teeth disengagements occur due to axial movement and showed that the airflow features are largely dictated by the teeth tip to step distance. The issue of how the rotordynamic forces respond in the presence of rotor-shifting for labyrinth seals, however, still remains untouched.

1. Objectives

This work was partially motivated by the lack of reported data on the rotordynamic characteristics under rotor-axial-shifting circumstances, and was aimed at gaining an insight into the rotordynamics of labyrinth seals under these conditions using the CFD-perturbation modelling method. Specific objectives include:

1. To predict quantitatively the rotordynamic coefficients in a high-low labyrinth seal with various rotor axial shifting, over a range of seal clearances and inlet swirl velocities.
2. To explain the surprisingly large sensitivity variation of dynamic forces to seal configurations due to rotor shifting.
3. To provide useful information for high-low seal design as well as a stability diagnosis of high-performance steam turbines.

B. Numerical Method

A well-established CFD-perturbation model was employed to predict the rotordynamic coefficients. Using a perturbation method, the time-averaged, turbulent Navier-Stokes equations are decomposed into the perturbed zeroth- and first-order governing equations. The Reynolds-averaged Navier-Stokes equations are first solved to obtain the zeroth-order solution with the rotor in the centered position within the seal housing. Then the first-order solution of the perturbed Navier-Stokes equations is obtained to account for a very small rotor displacement (*i.e.* perturbation) from the centered position. Finally, by integrating the circumferential pressure variation around the circumference of the rotor within the seal the flow-induced forces on the rotor are evaluated. Further details can be found in Chapter III and in [25].

1. CFD Considerations

The schematic diagram of the investigated high-low labyrinth seal is shown in Fig. 41 (a). It consists of five blocks and a total of eleven teeth, with six long teeth and five short ones alternately arranged. Letters 'A' to 'S' are points located upon the rotor surface. Section 'D-E' is the high-portion rotor surface on the first rotor block, while section 'F-G' is the low-portion surface immediately downstream from the first block. The axial rotor position relative to the teeth is shown in Fig. 41 (b). In the present study, the ratio a/b was varied in the range of 0∼1.0 as the rotor experienced axial shifting due to thermal expansion. When $a/b = 0.5$, the shorter teeth are centered upon the rotor blocks, which is the position of design without any rotor displacement; a/b increases from 0.5 when the rotor shifts against the direction of flow (*i.e.* upstream rotor-shifting) and decreases from 0.5 when shifting in the direction of the flow (*i.e.* downstream rotor-shifting). The straight-through labyrinth

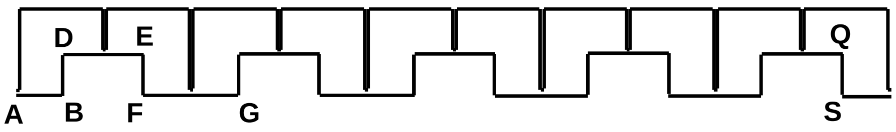

(a) Typical High-Low Labyrinth Seal Configuration

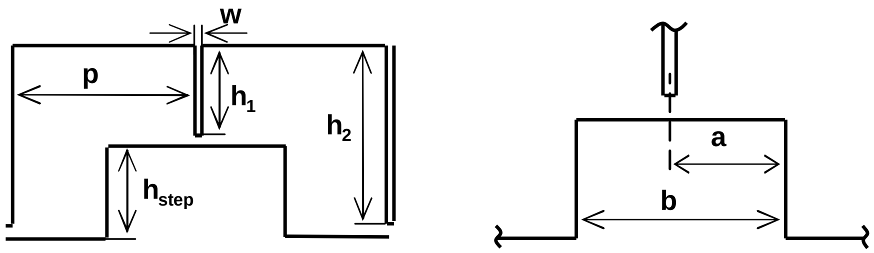

(b) Seal Dimensions and Relative Tooth Axial Position

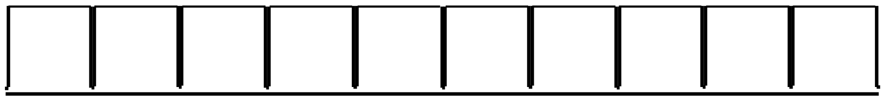

(c) Straight-Through Labyrinth Seal Configuration

Fig. 41. Schematic of labyrinth seals: (a) typical high-low seal configuration; (b) seal dimensions and relative tooth axial position; (c) straight-through labyrinth seal configuration.

seal shown in Fig. 41 (c) is a variant of the high-low labyrinth seal with the rotor blocks removed and with all the clearances unchanged.

Steam was used as the working fluid, and the running speed was 3,600 rpm. The labyrinth seal geometric details and operating conditions are listed in Table IX. Inlet swirl velocity and the pressures upstream and downstream of the seal were specified as boundary conditions. On the rotor and stator walls, no-slip surface conditions were specified via standard wall-functions. The near wall computational cells have both y^+ and x^+ within the range from 15 to 90 on both the high-portion and the low-portion surfaces across the seal.

2. Grid Independence Study

Grid independence testing was performed with an upstream pressure of 30.4 bar, a downstream pressure of 19.3 bar, and an inlet swirl velocity of 75 m/s. Four grids were tested as shown in Table X. Grid independence was achieved at 656 × 65 lines and was used as the production grid.

C. Results and Discussion

1. Leakage

Figure 42 shows the variation of the predicted leakage flow rate with relative axial rotor positions at three seal clearances. It was found that a small leakage variation was induced by rotor shifting. For example, the leakage shows a 9.4% increase when the rotor shifts against the flow direction from $a/b = 0.5$ to $a/b = 0.0$ (*i.e.* the most upstream position), and only a 4.6% decrease when the rotor shifts downstream from $a/b = 0.5$ to $a/b = 1.0$ (i.e. the most downstream position). Furthermore, for a given pressure difference the steam leakage is observed to vary approximately proportionally

Table IX. Dimensions and Conditions for Typical High-Low Labyrinth Seals in Steam Turbines.

Dimensions								Conditions				
Stator				Rotor								
w (mm)	p (mm)	h_1 (mm)	h_2 (mm)	b (mm)	h_{step} (mm)	R_{sh} (mm)	C_r (mm)	W_0 (m/s)	P_{up} (bar)	P_{dn} (bar)	ω (rpm)	T (K)
0.254	7.366	3.175	6.350	5.334	3.175	152.4	0.254∼0.762	8∼208	30.3	19.7	3,600	749

Table X. Grid Independence Testing Results

NI×NJ	k (MN/m)	$\frac{(k_c - k_f)}{k_f}$ (%)	C (KNs/m)	$\frac{(C_c - C_f)}{C_f}$ (%)
546×48	0.555	−−	2.56	−−
656×65	0.610	8.9	2.79	8.67
766×78	0.616	1.03	2.81	0.73
892×86	0.620	0.61	2.82	0.52

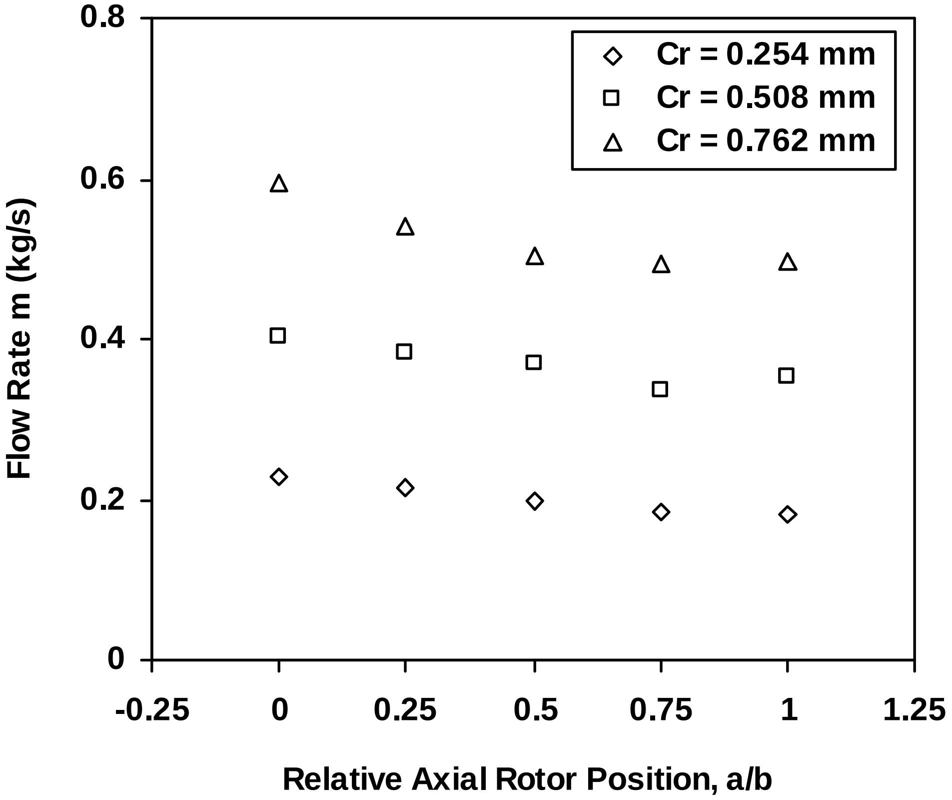

Fig. 42. Predicted mass flow rate vs. relative axial rotor position a/b for high-low seals.

with the seal radial clearance.

The vector plots of Fig. 43 show different flow patterns for a high-low labyrinth seal at three relative axial rotor positions, *i.e.* $a/b = 0.0$, 0.5, and 1.0. It can be observed from Fig. 43 (a) that the fluid approaches the long-teeth tip nearly horizontally when $a/b = 0.0$, although it approaches at a sharp angle when $a/b =$ 0.5 and 1.0. Figure 43 (b) shows that two large recirculation zones exist upstream of the shorter teeth for the rotor position $a/b = 0.5$. The smaller recirculation zone above the rotor block continuously decreases in size as the rotor shifts downstream from the teeth-centered position. An abrupt change in flow pattern occurs when a/b reaches 1.0, where the smaller recirculation zone vanishes and only the larger one remains. Perhaps this is related to the findings in Fig. 42 that at large clearances the leakage rate recovers somewhat when $a/b = 1.0$, in contrast to the constant decrease as a/b changes from 0.0 to 0.75. It is suggested that this recovery around $a/b = 1.0$ is related to the disappearance of the small recirculation zone.

Extreme conditions such as when the short teeth shift off the rotor block (*i.e.* $a/b < 0$ or $a/b > 1.0$) were also computed. In these situations, the flow pattern behaves quite differently and the induced dynamic forces increase significantly in magnitude. Therefore, the high-low labyrinth seals should be designed to have enough of a safety margin in order to avoid operation in such a flow regime.

2. Rotordynamic Forces

Leakage is not the only criterion that should be considered when selecting a seal for a certain application. The seal's rotordynamic behavior subject to rotor-shifting is also crucial and must be predicted accurately. Various operating conditions were investigated which cover a wide range of seal clearances and inlet swirl velocities as shown in Figures 44 through 48. One important finding from the above figures

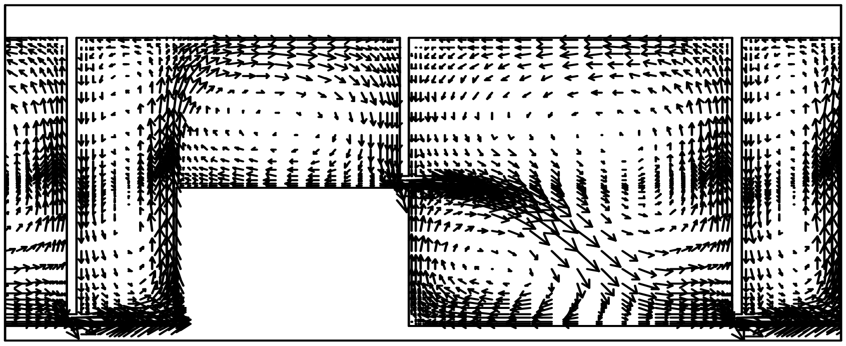

(a) a/b = 0.0

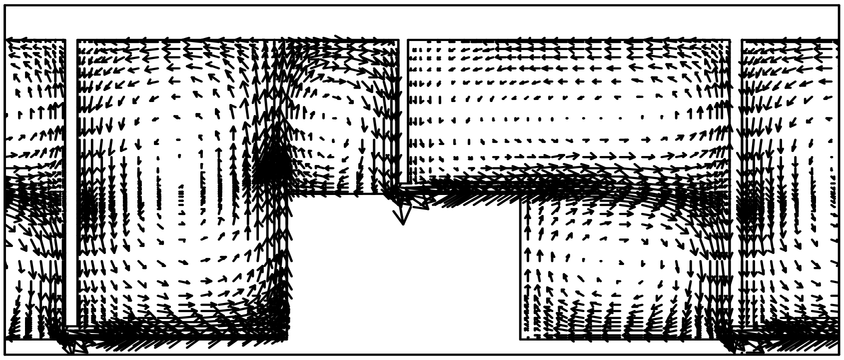

(b) a/b = 0.5

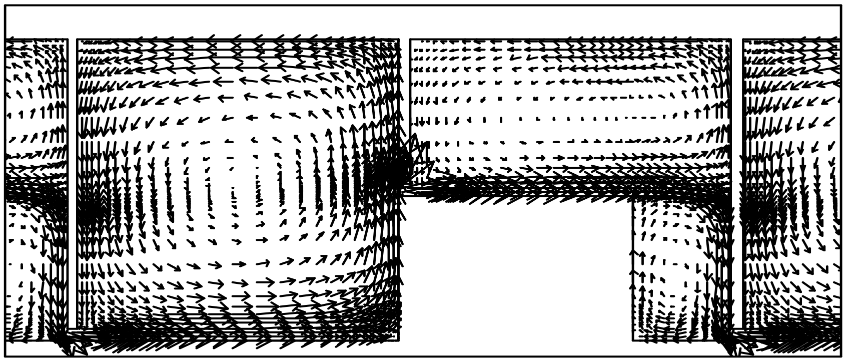

(c) a/b = 1.0

Fig. 43. Flow patterns within a high-low seal for different relative axial rotor positions: (a) $a/b = 0.0$; (b) $a/b = 0.5$; (c) $a/b = 1.0$.

is that the rotor-axial-shifting produces a surprisingly large effect on rotordynamic forces, which will be explained in detail below.

Figure 44 shows the variation of the cross-coupled stiffness k and direct damping coefficient C with relative axial rotor position a/b at three different seal clearances with the same operating conditions as in Fig. 42. For all the three clearances considered, downstream rotor-shifting steadily decreases the magnitude of both cross-coupled stiffness and direct damping. Furthermore, the seal rotordynamics is found to be quite sensitive to the axial rotor positions. For a given seal clearance $C_r = 0.254$ mm, for example, the cross-coupled stiffness k reduces 39.8% from $a/b = 0.0$ to $a/b = 0.25$, and 42.3% from $a/b = 0.25$ to $a/b = 0.5$. In addition, almost no discernable variation of direct damping was found for the seal clearances considered.

The effective damping ($C_{eff} = C - k/\Omega$), which incorporates the typically destabilizing k and the counteracting C, represents the net tangential force acting on the rotor. Sub-synchronous vibration with Ω equal to 0.5ω was assumed in evaluating C_{eff}. When positive, the net damping force acts in the direction opposite to the rotor whirl and therefore is the net stabilizing force. From Fig. 45 it is evident that the seal with an axial rotor position $a/b = 0.0$ is the most destabilizing. The stability characteristics are improved steadily as the rotor shifts downstream from $a/b = 0.0$ to a/b =1.0, and the least destabilizing characteristic is achieved at $a/b = 1.0$.

Seal inlet swirl is well recognized as a major source of turbomachiney seal instability. A deeper understanding of the influence of rotor-shifting can be acquired by examining the rotordynamic variation with inlet swirl W_0 as well as with different rotor positions.

Figure 46 shows the variation of the predicted k and C with seal inlet swirl velocity W_0 for a high-low seal with three different axial rotor positions as well as a straight-through "ST_TH" seal whose geometry is shown in Fig. 41 (c). The running

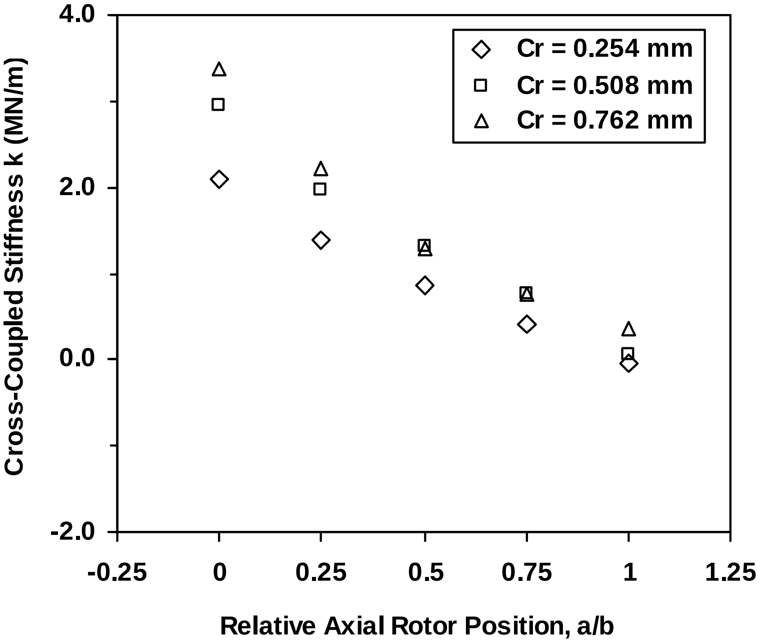

(a) Cross-Coupled Stiffness

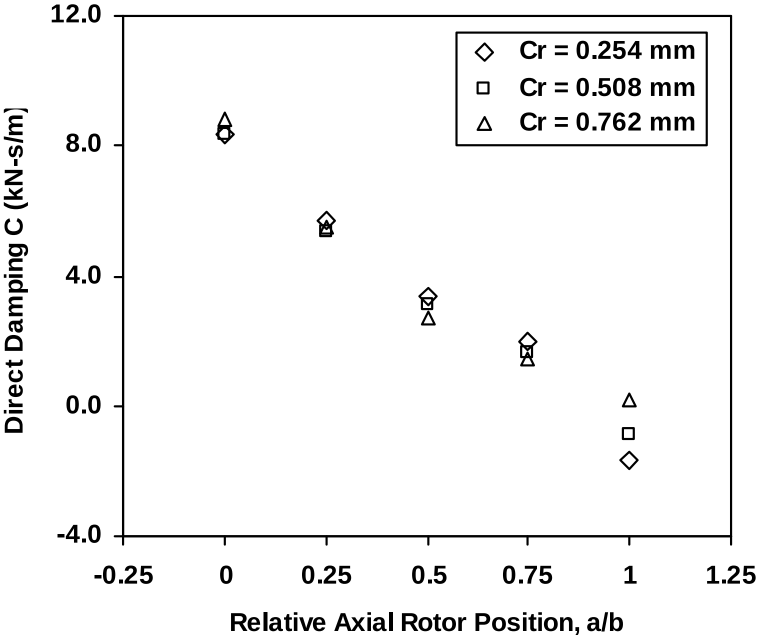

(b) Direct Damping

Fig. 44. Predicted tangential force coefficients vs. relative axial rotor position a/b for high-low seals: (a) cross-coupled stiffness; (b) direct damping. [$W_0 = 75$ m/s]

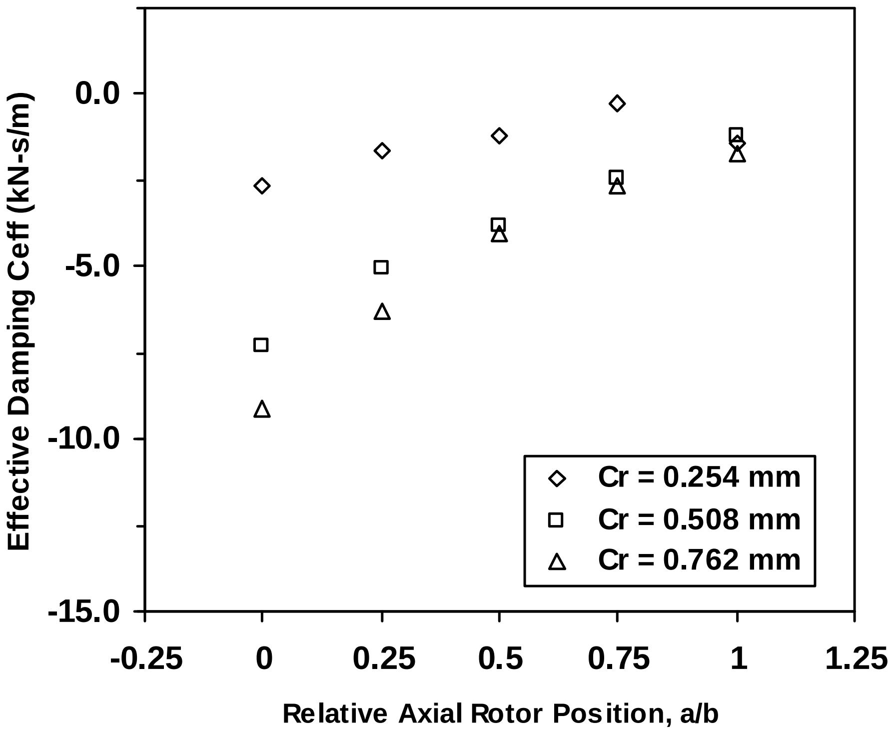

Fig. 45. Predicted effective damping coefficient vs. relative axial rotor position a/b for high-low seals. [$W_0 = 75$ m/s]

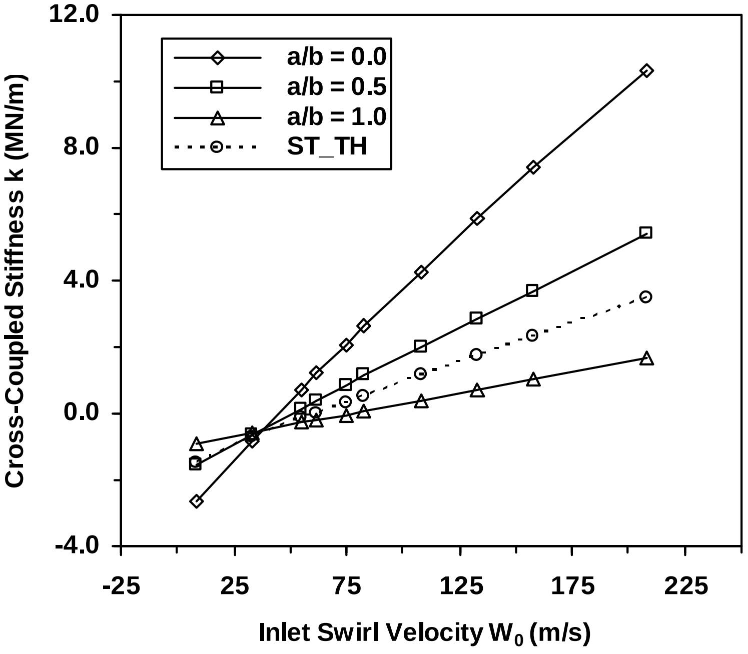

(a) Cross-Coupled Stiffness

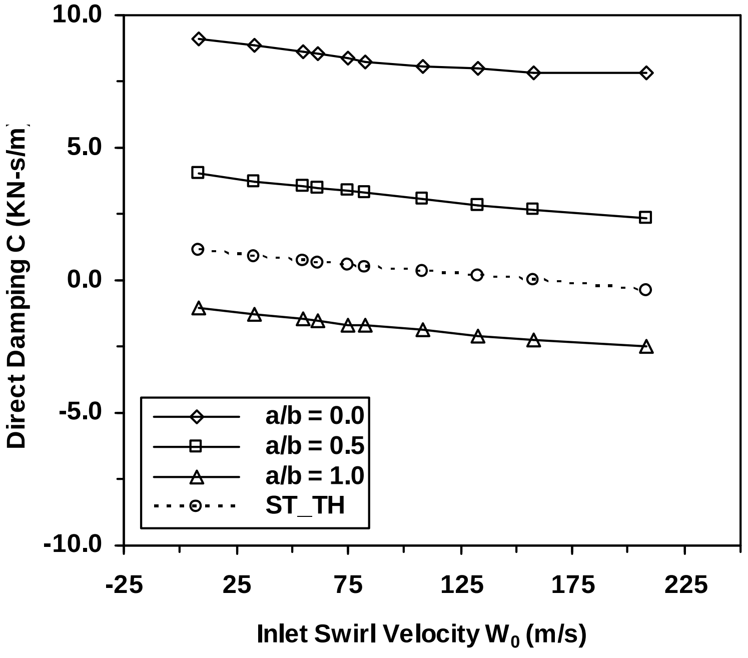

(b) Direct Damping

Fig. 46. Plot of cross-coupled stiffness k and direct damping C vs. inlet swirl velocity W_0 for different seal configurations: (a) cross-coupled stiffness; (b) direct damping. [$C_r = 0.762$ mm]

speed and other conditions are the same as in Figs. 42 - 45. From Fig. 46, it is found that both k and C exhibit nearly linear dependence on W_0 for the high-low seal as well as for the straight-through seal. On the other hand, the impact of W_0 on K is far from linear as illustrated in Fig. 48.

Another important finding from Fig. 46 is that both k and C show surprisingly large sensitivities to axial rotor positions, especially when W_0 is large. This can be seen from the apparent large difference of k for different rotor axial positions. In addition, inlet swirl W_0 exerts a remarkable effect on k while exerting only a trivial effect on C, as seen by comparing the steep profiles of k vs. W_0 in Fig. 46 (a) with the relatively flat profiles of C vs. W_0 in Fig. 46 (b).

It was further found from Fig. 46 (a) that, for both straight-through and high-low labyrinth seals, the plots of k vs. W_0 all pass through one particular point. Rotor-axial-shifting in high-low labyrinth seals does not change this point's location. The seal-inlet swirl velocity W_0 at this point is about 0.6 times the rotor peripheral speed, which coincidentally approximates the seal asymptotic swirl velocity (*i.e.* the seal exit swirl velocity for a very long seal). This implies that rotor axial shifting has a negligible effect on k [rotordynamic driving force] when the seal inlet swirl is around the seal asymptotic swirl (*i.e.* $W_0 \approx 0.6\omega R_{sh}$). When the swirl velocity remains fairly constant along the seal length, k gives shaft-position-independent behavior.

Figure 47 shows that rotor axial shifting has a negligible effect on C_{eff} [net rotordynamic force] when $W_0 \approx 1.2\omega R_{sh}$. Because C is not sensitive to the seal inlet swirl as shown in Fig. 46 (b), a combination of k and C gives a different inlet swirl value where C_{eff} exhibits shift-independent behavior.

Figure 48 illustrates the variation of direct stiffness K with seal configurations and inlet swirl velocities. The effect of axial rotor position is shown in Fig. 48 (a). For all three clearances, K decreases as the rotor shifts downstream from $a/b = 0.0$ to a/b

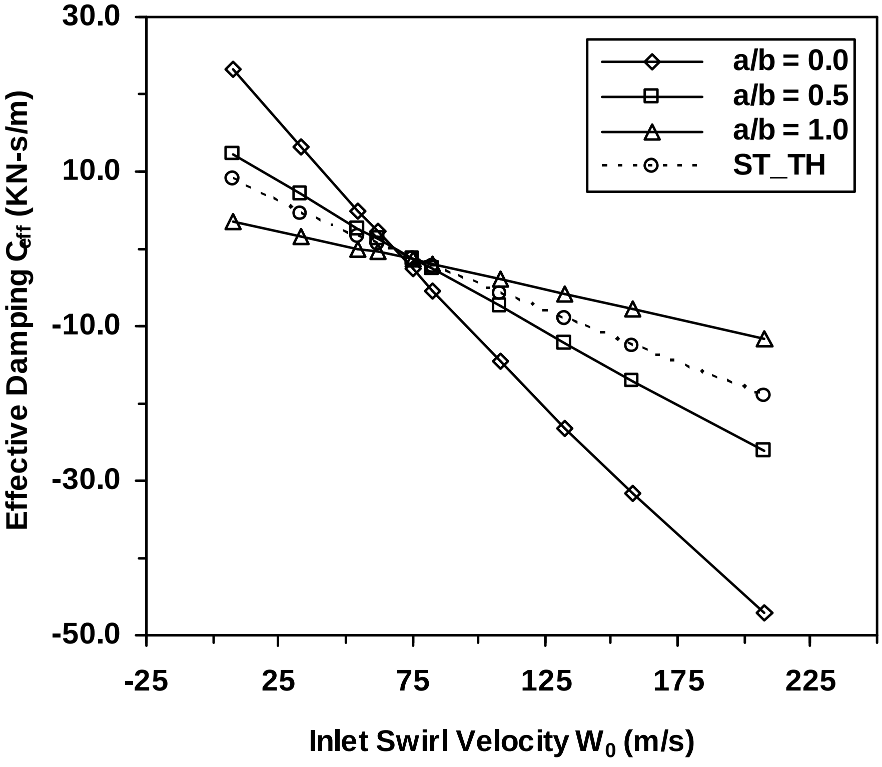

Fig. 47. Plot of effective damping C_{eff} vs. inlet swirl velocity W_0 for different seal configurations. [$C_r = 0.762$ mm]

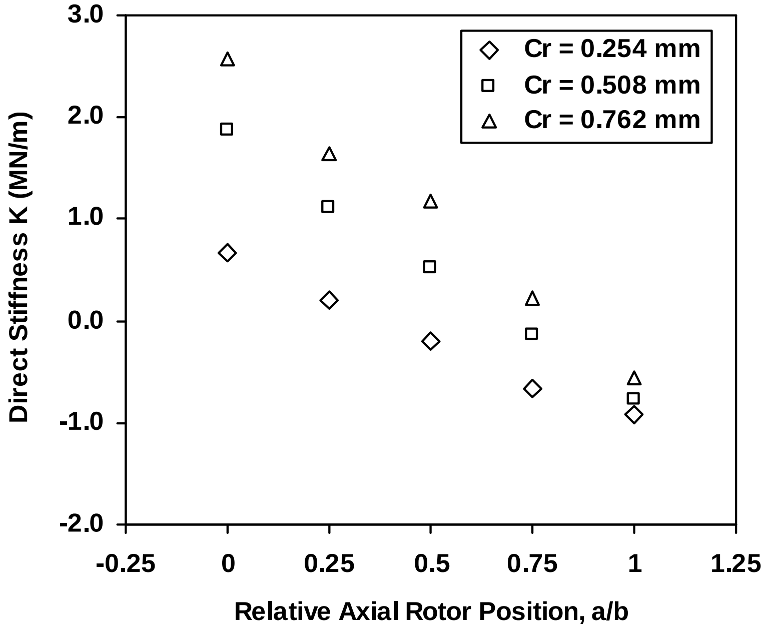

(a) Effect of seal clearance [$W_0 = 75$ m/s]

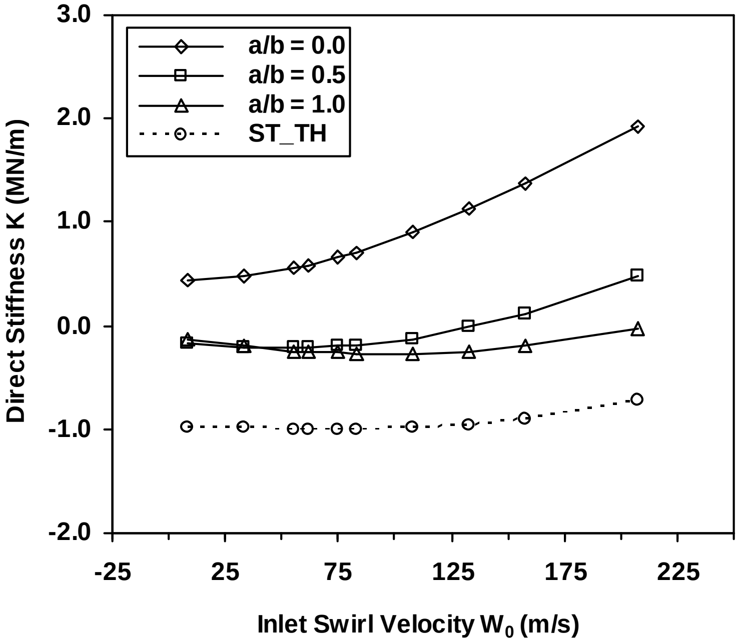

(b) Effect of inlet swirl [$C_r = 0.762$ mm]

Fig. 48. Predicted direct stiffness K: (a) effect of seal clearance [$W_0 = 75$ m/s]; (b) effect of inlet swirl velocity [$C_r = 0.762$ mm].

= 1.0. Additionally, a wide range of sensitivity of K to labyrinth seal configuration is observed from Fig. 48 (b). It is obvious that the straight-through seal gives the lowest K of all the seal configurations considered; perhaps this is because there is no radial impingement on the rotor in straight-through seals.

Figure 49 shows the C_{eff} distribution along the rotor surface for the high-low seal, with the thick line denoting the high portion (*i.e.* rotor block) and the thin line denoting the low portion (*i.e.* groove). By comparing the C_{eff} magnitude at the three relative rotor positions, it can be observed that the first several cavities, especially the first and the second, are more important in determining seal stability than the others. When the seal-inlet swirl is greater than the rotor peripheral speed, a large destabilizing effect is produced in the first two cavities, which then gradually decreases in the subsequent cavities and even becomes stabilizing in the last cavities. Specifically, the low portion immediately downstream of the first rotor block acts as the predominant part for stability characteristics of at least the present high-low labyrinth seal. This is compatible with the recent experimental results of Iwatsubo and Iwasaki [58] who found that adding swirl brakes at the inlet, particularly inside the first and second cavities, was effective in reducing the circumferential swirl velocity and therefore controlling seal stability.

Interestingly, for the two positions $a/b = 0.0$ and $a/b = 1.0$, the influence from the first several cavities is overwhelmingly larger than from the last several cavities. However, for the teeth-centered position ($a/b = 0.5$), a considerable destabilizing effect arises from the last several cavities and is almost comparable to the destabilizing effect from the first several cavities.

It is hypothesized that the near rotor swirl velocity variation along the axial direction has a substantial effect on the stability characteristics, thereby explaining the apparently large difference in the rotordynamic sensitivities to rotor position.

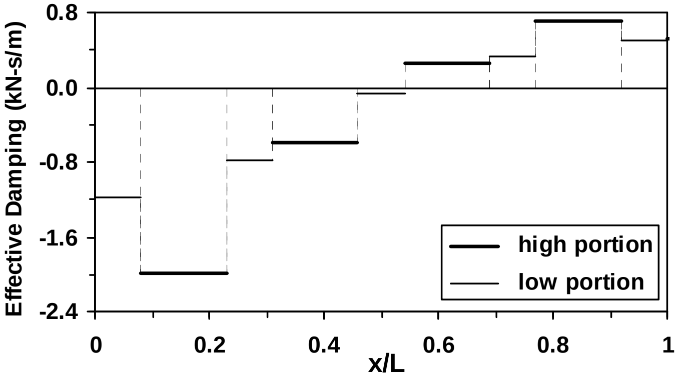

(a) a/b = 0.0

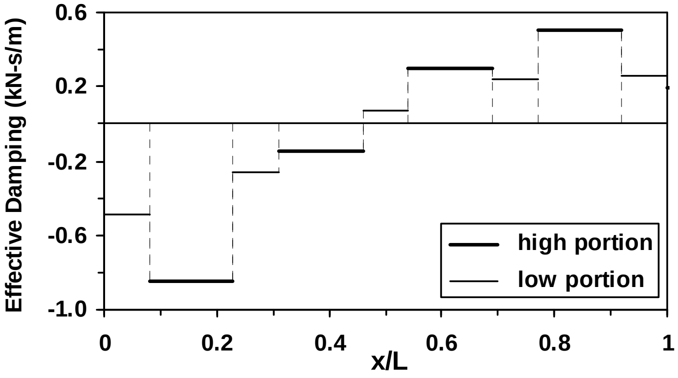

(a) a/b = 0.5

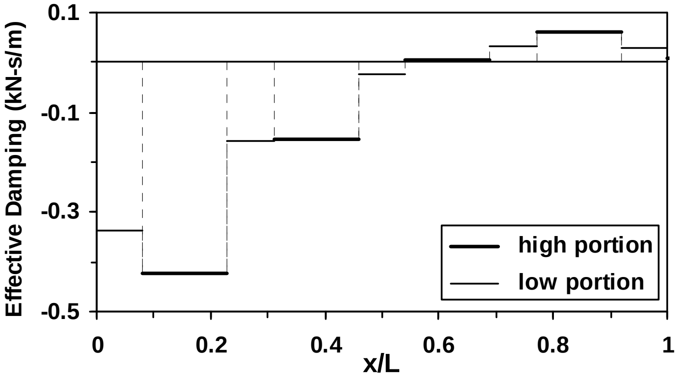

(a) a/b = 1.0

Fig. 49. Effective damping distribution along the rotor surface for high-low seals at different relative axial rotor positions: (a) a/b = 0.0; (b) a/b = 0.5; (c) a/b = 1.0. [C_r = 0.762 mm; W_0 = 75 m/s]

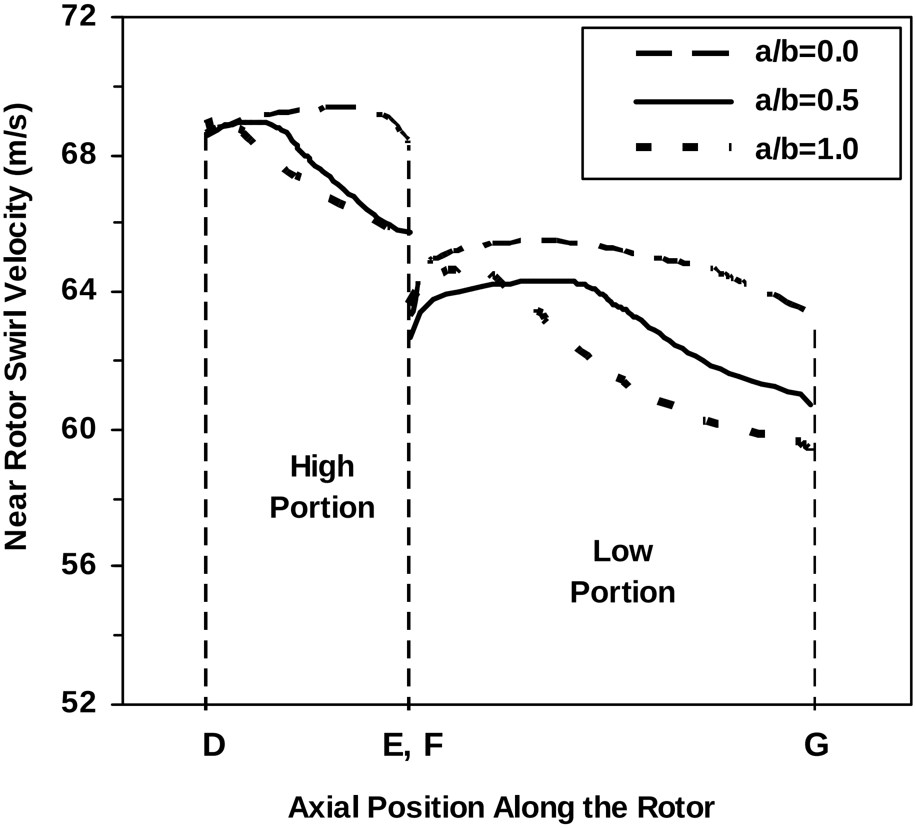

Fig. 50. Axial distribution of swirl velocity within a high-low labyrinth seal: (a) high portion, D-E; (b) low portion, F-G. [$C_r = 0.762$ mm; $W_0 = 75$ m/s]

Figure 50 shows the near-rotor swirl velocity distribution inside the first and second cavities with the same operational conditions as those in Fig. 44 and 45. The seal clearance is 0.254 mm, and the definition of points *D, E, F, G* can be found in Fig. 41 (a). For a fixed seal inlet swirl velocity, the near wall swirl velocity inside the seal is mainly influenced by the leakage rate, or equivalently by the fluid particle residence time within the seal. The smaller the leakage, the longer the residence time, and thus the more a fluid particle will adjust from the seal inlet swirl value toward the asymptotic swirl value, which is about 0.6 times the rotor peripheral speed. Therefore, for seal inlet swirl values greater than the asymptotic swirl value, smaller swirl velocities will be developed along the rotor, which produce a smaller net destabilizing force. This rotordynamics mechanism is endorsed by the predicted relationship between leakage and effective damping coefficient for a high-low labyrinth seal at $a/b = 0.0$ as shown in Fig 51.

D. Summary

Numerical studies were performed to investigate the influence of rotor axial shifting on rotordynamic forces in high-low labyrinth seals using a CFD modelling approach. Various operational conditions were considered to gain a better understanding of the labyrinth seal rotordynamics, which covered a range of seal clearances and seal-inlet swirl velocities. Seal configurations were found to have a surprisingly large effect upon dynamic force coefficients. A rotordynamic mechanism was proposed to explain the variations of the seal stability sensitivity to rotor axial shifting. Specific findings include:

1. Rotor axial shifting was found to have surprisingly large effects on rotordynamic force coefficients. Both k and C show sensitivities to labyrinth seal

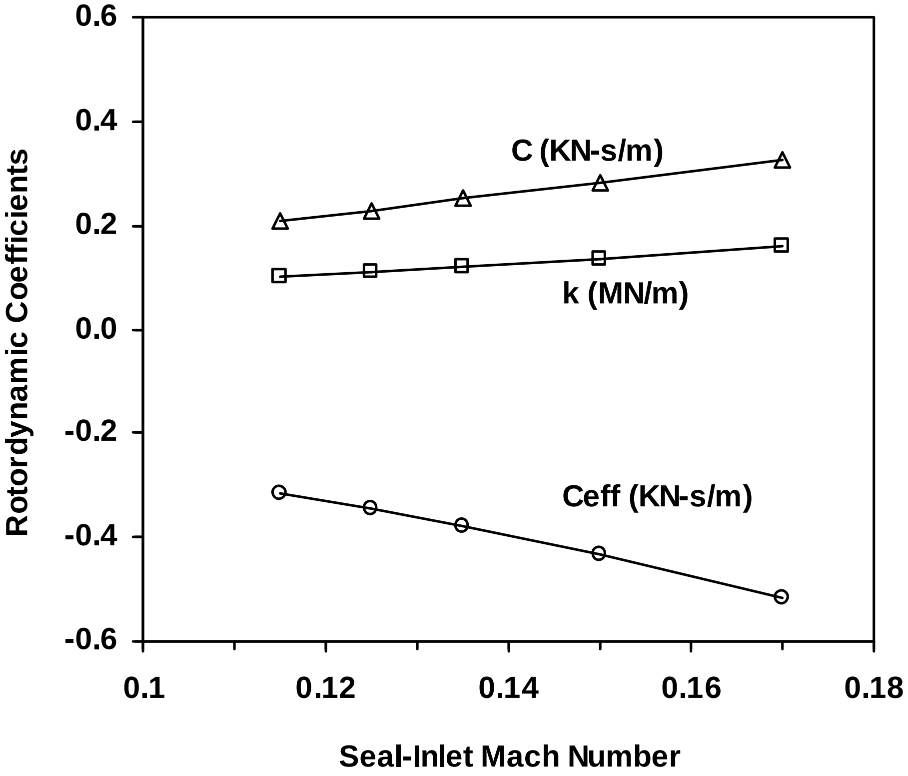

Fig. 51. Effect of inlet Mach number on rotordynamic coefficients. [$C_r = 0.762$ mm; $W_0 = 75$ m/s; $\omega = 3{,}600$ rpm; $P_{dn} = 19.7$ bar; $T_{up} = 749$ K]

configurations due to different relative rotor-teeth positions. The variation of cross-coupled stiffness k between $a/b = 0.5$ and $a/b = 0.0$, for example, is 143% for a high-low labyrinth seal with $C_r = 0.254$ mm and 125% for a seal with $C_r = 0.508$ mm.

2. Compared to a seal with a centered teeth position ($a/b = 0.5$), the seal subject to rotor-shifting in the upstream direction (*i.e.* against the leakage) suffers an increased leakage and produces a more destabilizing rotordynamic effect, while the seal with downstream rotor-shifting brings a reduced leakage and a less destabilizing effect.

3. Cross-coupled stiffness was found to show negligible dependence on rotor position when the seal inlet swirl is around the seal asymptotic swirl (*i.e.* $W_0 \approx 0.6\omega R_{sh}$) and the swirl velocity remains fairly constant along the seal length.

4. The first several cavities, especially the first and the second cavities, are the most important components in determining the stability characteristics for high-low labyrinth seals.

5. The substantial influence of swirl variation along the rotor on rotordynamics is suggested to explain the large sensitivity differences of seal rotordynamics caused by the rotor axial shifting.

CHAPTER VIII

SUMMARY AND CONCLUSIONS

A. Boundary Condition Correlation Development and Assessment

Extensive parametric studies were performed over a wide range of conditions in order to gain insight into the dynamic characteristics at the seal inlet. Then, this insight was employed in devising seal-inlet boundary condition correlations for the flow disturbance quantities with the goals of simplicity, maximized breadth of application, and relative freedom from numerical difficulties. The benefit of using these correlations was evaluated using two very different seal test cases. For both cases, improved agreement with measurements was obtained in comparison to previous models. The primary findings are as follows:

1. The cross-coupled stiffness k is influenced, in descending order of importance, by seal-inlet W_{1C}, U_{1S}, P_{1S} and W_{1S}. In contrast to the historical assumption of seal-inlet $W_{1C} = 0$, the magnitude of W_{1C} is larger than that of U_{1S}, and it is similar to that of U_{1C}.

2. The W_{1C} and W_{1S} boundary condition correlations developed here should be used to replace the historical assumption of $W_{1C} = 0$ and $W_{1S} = 0$ at the seal inlet.

3. The seal-inlet swirl "slip" velocity $(\omega R_{sh} - \bar{W}_0)$ was found to have an extremely precise relationship with the cross-coupled stiffness as well as the seal-inlet bulk-average swirl velocity disturbance cosine component $\bar{W}_{1C}$. Thus, the number of experiments or computer runs needed to determine the effect of spin speed, shaft radius and inlet swirl velocity on the cross-coupled stiffness is greatly reduced

by plotting the simplified relationship of the cross-coupled stiffness against the inlet swirl slip velocity $(\omega R_{sh} - \bar{W}_0)$ rather than against ω or W_0 alone.

4. The upstream chamber size and shape were found to have a substantial influence upon the seal-inlet swirl disturbance velocity W_{1S}, which plays a significant role in determining the direct stiffness K.
5. For the liquid and gas seals considered, improved agreement with measurements was generally obtained using the developed boundary condition correlations with the option for non-zero W_{1C} and W_{1S}, compared to the option with $W_{1C} = W_{1S} = 0$.
6. For all of the gas labyrinth seals considered, the correlation set with the W_{1C}-profile option gave a better prediction of C_{eff} and k than that with the W_{1C}-bulk option. For CFD-perturbation models and full 3-D CFD models, the W_{1C}-profile option is recommended. The W_{1C}-bulk option is appropriate for bulk models because they do not allow the radial distribution of any quantity.
7. Direct stiffness K is only slightly affected by W_{1C}. Thus it was not surprising that the $W_{1C} = W_{1S} = 0$ option gives good predictions for K.

B. Labyrinth Teeth Damage Effects on Rotordynamics of Compressor Eye Seals

The inclusion of at least an approximate shroud leakage path chamber is preferred for an accurate prediction of rotordynamic forces for compressor impeller eye seals. The general findings to be learned concerning the teeth damage influence on rotordynamics of eye seals are as follows:

1. Impeller eye seals with damaged teeth suffer significant leakage increases due to the enlarged seal clearance from the teeth damage.

2. For a fixed seal clearance, the distorted teeth-tip shapes have a negligible influence on: (a) leakage, (b) seal-inlet swirl velocity and (c) rotordynamic forces.

3. for a fixed leak path chamber and seal geometry, the seal-inlet swirl W_0 is primarily determined by the leakage path inlet angular momentum and the net friction effect from the rotor and stator.

4. The rule-of-thumb assumption that the leakage path swirl ratio, *i.e.* the ratio of the local fluid swirl to the local impeller spin speed, is approximately $0.6 \sim 0.65$ along the shroud leakage path is too crude to allow accurate estimation of the seal inlet swirl W_0. Because this rule-of-thumb gives an incorrect seal-inlet swirl velocity, which is important for all seal rotordynamics models, it needs to be improved.

C. Rotor Axial Growth Effects on Steam Turbine Seal Rotordynamics

Rotor axial growth significantly alters the flow pattern and rotordynamic forces within labyrinths, which in turn could considerably affect the rotor-seal system's stability characteristics. The findings that are of specific interest are:

1. The rotor axial growth was found to have surprisingly large effects on the rotordynamic force coefficients. Both k and C show sensitivities to labyrinth seal configurations from different relative rotor-teeth positions.

2. Compared to the rotor design position (*i.e.* $a/b = 0.5$), the seal subject to rotor growth in the upstream (*i.e.* against the leakage) direction suffers an increased leakage and produces a more destabilizing rotordynamic effect, while the seal with downstream rotor-shifting gives a reduced leakage and a less destabilizing effect.

3. All plots of k vs. W_0 intersect approximately at one point which is not altered by rotor axial growth. The inlet swirl velocity corresponding to this particular point was found to be about 0.6 times the rotor peripheral speed, which is itself approximately the asymptotic seal swirl velocity.

4. The first several cavities, especially the first and the second, are the most important in determining the stability characteristics for high-low labyrinth seals.

D. Conclusions

Based on the findings in this study, the following conclusions can be made:

1. The seal inlet W_{1C} was found to be a very important seal inlet boundary condition that has been assumed as zero; however, the other seal inlet boundary condition quantities, such as the inlet energy loss coefficient, have had a range of assumed values. Because the developed boundary condition correlation for W_{1C} and W_{1S} were found to give rotordynamic force predictions that are close to measurements, these correlations are recommended for CFD-perturbation models, bulk-flow models, and full 3-D CFD models to specify improved boundary conditions at the seal inlet.

2. The finding that a precise relationship exists between the cross-coupled stiffness k and the swirl "slip" $[\omega R_{sh} - W_0]$is very promising for reducing the experiment cost or computer runs required when the dependence of k upon spin speed, shaft radius and inlet swirl velocity is needed.

3. In the case of seal teeth damage in centrifugal compressors, it is the change of seal clearance that exerts a major influence on rotordynamic characteristics, while the deformation of the seal teeth tips has a negligible effect. In addition,

the inclusion of a leakage path chamber is preferred for an accurate prediction of the dynamic forces in impeller eye seals.

4. At least for steam turbines, the change of high-low seal configurations due to relative rotor axial growth was found to have a significant influence upon rotordynamic force coefficients. Enough safety margin should be considered for the design of high-low labyrinth seals to avoid unexpected self-excited vibrations.

NOMENCLATURE

Roman Symbols

C, c	Direct and cross coupled damping coefficients (kN-s/m)
C_r	Seal radial clearance (mm)
C_2, E, G	Height, left width, and right width of the teeth tip (mm)
e	Radius of rotor whirling motion (mm)
F	Fluid reaction force (N)
H_{Imp}	Radial height from eye seal to impeller discharge
K, k	Direct and cross coupled stiffness coefficients (N/m)
k	Turbulent kinetic energy ($\mathrm{m}^2/\mathrm{s}^2$)
$\dot{m}$	Mass flow rate (kg/s)
M, m	Direct and cross coupled inertia coefficients (Ns^2/m)
M	Axial velocity Mach number
P	Pressure (Pa)
P'	Pressure correction (Pa)
ΔP	Pressure drop (Pa)
r	Radial coordinate
R	Universal gas constant [N-m/(kg $\cdot$ K)]
R_{sh}	Shaft radius of the seal (m)
R^*	Concentric-rotor surface location
U	Streamwise (axial) velocity component (m/s)
V	Radial velocity component (m/s)
W	Swirl velocity component (m/s)
W_0	Swirl velocity at seal inlet

x	Streamwise (axial) coordinate
y	Radial distance from rotor surface (m)
t	Time (s)

Greek Symbols

ϵ	Relative eccentricity of the rotor $[e/C_r]$
ε	Turbulent kinetic energy dissipation rate ($\mathrm{m^2/s^3}$)
γ	The gas compressibility factor
Γ	Leakage path inlet swirl ratio $[W_{Imp}/(\omega R_{Imp})]$
μ	Dynamic viscosity [g/(ms)]
ν	Kinetic viscosity $[= \mu/\rho]$ (m^2/s)
θ	Circumferential coordinate
Φ	General dependent variable such as velocity and pressure
Φ_1	First-order general dependent variable
$\hat{\Phi}_1$	Complex function of first order dependent variable
ρ	Density (kg/m^3)
τ	Shear stress (Pa)
ω	Shaft speed (rpm)
Ω	Rotor whirling speed (rpm)
ξ	Minor loss coefficient at the seal inlet

Subscripts

c	Coarse grid
dn	Downstream
eff	Effective coefficient

f	Fine grid
H	High pressure End in Upstream chamber inlet
Imp	Impeller tip
in	Upstream chamber inlet
inj	Injection
L	Low pressure End
$mach$	Mach number
r	Radial
sh	Shaft
t	Tangential
up	Upstream
$0, 1$	Zeroth- and first-order, respectively
$1C$	First order cosine component
$1S$	First order sine component
ex	Exit

Superscripts

$\wedge$	Complex function
$^{-}$	Overbar denotes radially bulk-averaged value
.	First derivative
..	Second derivative

Abbreviations

CFD	Computational Fluid Dynamics
IPR	Injection pressure ratio, P_H/P_inj

PR	Pressure ratio, $P_L/{}_PH$
PDBC	Perturbation with Disturbed Boundary Condition
UCL	Upstream chamber length(m)
UCH	Upstream chamber height (m)

REFERENCES

[1] D.W. Childs, *Turbomachinery Rotordynamics: Phenomena, Modeling and Analysis*, New York: John Wiley and Sons, 1993.

[2] J. S. Alford, "Protecting turbomachiery from self-excited rotor whirl," *ASME Journal of Engineering for Power*, vol. 87, pp. 333–344, 1965.

[3] H.F. Black and D.N. Jensen, "Dynamic hybrid properties of annular pressure seals," *Journal of Mechanical Engineers*, vol. 113, pp. 353–361, 1970.

[4] D.W. Childs, "Dynamic analysis of turbulent annular seals based on Hirs lubrication equation," *ASME Journal of Lubrication Technology*, vol. 105, pp. 429–436, 1983.

[5] D.W. Childs, "Finite length solutions for rotordynamic coefficients of turbulent annular seals," *ASME Journal of Lubrication Technology*, vol. 105, pp. 437–444, 1983.

[6] F.J. Dietzen and R. Nordmann, "Calculating rotordynamic coefficients of the seals by finite-difference techniques," *ASME Journal of Tribology*, vol. 109, pp. 338–394, 1987.

[7] N. Kim and D.L. Rhode, "A new CFD-perturbation model for the rotordynamics of incompressible flow seals," in *Proceedings of ASME TURBO EXPO 2000*, Munich, Germany, May 2000, 2000-GT-402.

[8] G. Venkatesan and D.L. Rhode, "CFD determination of pre-chamber flow perturbation inlet boundary conditions for seal rotordynamic models," in *Proceedings of ASME Turbo Expo 2003: Power for Land, Sea, and Air*, Atlanta, GA, June 2003, ASME, 2003-GT-38038.

[9] D. Wilcox and D.P. O'Brien, "Determining the root causes of subsynchronous instability problems in two centrifugal compressors," in *Proceedings of the Thirty-second Turbomachinery Symposium*, Houston, TX, September 2003, pp. 9–19.

[10] T. Iwatsubo, "Evaluation of instability forces of labyrinth seals in turbines or compressors, rotordynamic instability problems in high-performance turbomachinery," in *Proceedings of a Workshop Held at Texas A&M University*, College Station, TX, 1980, June 1980, pp. 489–498.

[11] C. Nelson, "Rotordynamic coefficients for compressible flow in tapered annular seals," *ASME Journal of Triboloy*, vol. 107, pp. 318–325, 1985.

[12] H.R. Wyssmann, T.C. Pham, and R.J. Jenny, "Prediction of stiffness and damping coefficients of centrifugal compressor labyrinth seals," *ASME Journal of Engineering for Gas Turbines and Power*, vol. 106, pp. 920–926, 1984.

[13] J.K. Scharrer, "A comparison of experimental and theoretical results for labyrinth gas seals," Ph.D. dissertation, Texas A&M University, College Station, TX, 1987.

[14] L. San Andes, "Dynamic force and moment coefficients for short length annular seals," *ASME Journal of Triboloy*, vol. 115, pp. 61–70, 1993.

[15] L. San Andes, "Effect of shaft misalignment on the dynamic force response of annular pressure seals," *STLE Tribology Transactions*, vol. 36, pp. 173–182, 1993.

[16] O. Marquette and D.W. Childs, "An extended three-control-volume theory for circumferentially-grooved liquid seals," *ASME Journal of Triboloy*, vol. 118, pp. 276–285, 1996.

[17] L.T. Tam, A.J. Przekwas, A. Muszyuska, R.C. Hendricks, M.J. Braun, and T.L. Mullen, "Numerical and analytical study of fluid dynamic forces in seals and bearings," *ASME Journal of Vibration, Acoustics, Stress and Reliability in Design*, vol. 110, pp. 315–325, 1988.

[18] M.M. Athavale, A.J. Przekwas, and R.C. Hendricks, "A finite-volume numerical method to calculate fluid forces and rotordynamic coefficients in seals," in *AIAA/SAE/ASME/ASEE 28th Joint Propulsion Conference and Exhibit*, Nashville, TN, July 1992, AIAA Paper 92-3742.

[19] D.W. Childs and J.K. Scharrer, "An Iwatsubo-based solution for labyrinth seals: A comparison to experimental results," *ASME Journal of Engineering for Gas Turbins and Power*, vol. 108, pp. 124–131, 1986.

[20] D.L. Rhode, S.J. Hensel, and M.J. Guidry, "Labyrinth seal rotordynamic force using a three-dimensional Navier-Stokes code," *ASME Journal of Triboloy*, vol. 114, pp. 683–689, 1992.

[21] D.L. Rhode, S.J. Hensel, and M.J. Guidry, "Three-dimensional computations of rotordynamic force in a labyrinth seal," *STLE Tribology Transactions*, vol. 36, pp. 461–469, 1993.

[22] E Isshi, C Kato, K. Kikuchi, and Y. Ueyama, "Prediction of rotordynamic forces in a labyrinth seal based on three-dimensional turbulence flow computation," *JSME International Journal, Series C*, vol. 40, pp. 743–748, 1997.

[23] E.A. Baskharone and S.J. Hensel, "A finite-element perturbation approach to fluid/rotor interaction in turbomachinery elements. Part 1: Theory," *ASME Journal of Fluids Engineering*, vol. 113, pp. 353–361, 1991.

[24] J.S. Alford, "A quasi-two-dimensional method for the rotordydamic analysis of centered labyrinth liquid seals," *Journal of Engineering for Gas Turbines and Power*, vol. 121, pp. 144–152, 1999.

[25] N. Kim, S. Park, and D.L. Rhode, "Predicted effects of shunt injection on the rotordynamics of gas labyrinth seals," *ASME Journal of Engineering for Gas Turbines and Powers*, vol. 125, pp. 167–174, 2003.

[26] S.V. Patankar, *Numerical Heat Transfer and Fluid Flow*, New York: Hemisphere Publishing and McGraw-Hill B.C., 1980.

[27] P.M. Gresho, "Incompressible fluid dynamics: Some fundamental formulation issues," *Annual Review of Fluid Mechanics*, vol. 23, pp. 413–453, 1991.

[28] J.J. Moore and A.B. Palazzolo, "CFD comparison to 3-D laser anemometer and rotordynamic force measurements for grooved liquid annular seals," in *Proceedings of ASME/STLE: International Tribology Conference*, Ontario, Canada, June 1998, pp. 43–56.

[29] F.J. Dietzen and R. Nordmann, "A 3-dimensional fiite-difference method for calcualting the dynamic coefficients in seals," in *Proceedings of a Workshop of Rotordynamic Instability Problems in High-Performance Turbomachinery Held at Texas A&M University*, College Station, TX, 1988, pp. 211–227.

[30] J.S. Alford, "Rotordynamic coefficients of circumferentially grooved liquid seals using the averaged Navier-Stokes equations," *ASME Journal of Tribology*, vol. 119, pp. 556–567, 1997.

[31] M. Arghir and J. Frene, "Forces and moments due to the misalignment vibrations in annular liquid seals using the averaged Navier-Stokes equations," *ASME*

Journal of Tribology, vol. 119, pp. 279–290, 1997.

[32] I.U. Haq, C.V. Kumar, and R.M. Al-Zaid, "Indentification of the intermittent synchronous instability in a high performance steam turbine rotor due to deteriorated labrinth seals," in *Proceedings of the International Gas Turbin & Aerospace Congress & Exhibition*, Stockholm, Sweden, June 1998, ASME, 98-GT-305.

[33] E.E. Clark, "Rotating equipment loss prevention - an insurer's viewpoint," in *Proceedings of the 25th Turbomachinery Symposium*, Turbomachinery Laboratory, Texas A&M University, College Station, TX, June 1996, pp. 103–122.

[34] J.S. Sohre, "Steam turbine blade failures, causes and correction," in *Proceedings of the 4th Turbomachinery Symposium*, Turbomachinery Laboratory, Texas A&M University, College Station, TX, May 1975, pp. 71–79.

[35] J.R. Dugas, "Maximizing an ethylene plant's turbomachinery reliability," in *Proceedings of 8th Turbomachinery Symposium*, Turbomachinery Laboratory, Texas A&M University, College Station, TX, July 1989, pp. 55–67.

[36] M.F. White, "An investigation of component deterioration in gas turbines uisng transient performance simulation," in *Proceedings of ASME TURBO EXPO 1988*, Reno-Tahoe, NV, 1988, 88-GT-258.

[37] C.B. Meher-Homji and R. Bhagave, "Condition monitoring and diagnostic aspects of gas turbine transsient response," in *Proceedings of the International Gas Turbine and Aeroengine Congress Exposition*, Cologne, Germany, June 1992, 92-GT-100.

[38] A.N. Lakshminarasimha, M.P. Boyce, and C.B. Meher-Homji, "Modelling and

analysis of gas turbine performance deterioration," in *Proceedings of the International Gas Turbine and Aeroengine Congress Exposition*, Cologne, Germany, June 1992, 92-GT-395.

[39] D.L. Rhode and R.I. Hibbs, "Tooth thickness effect on the performance of gas labyrinth seals," *ASME Journal of Triboloy*, vol. 114, pp. 791–795, 1992.

[40] D.L. Rhode and R.I. Hibbs, "Clearance effects on corresponding annular and labyrinth seal flow leakage characteristics," *ASME Journal of Triboloy*, vol. 115, pp. 699–704, 1993.

[41] H. Zimmerman, A. Kammerer, and K. H. Wolff, "Performance of worn labyrinth seals," *ASME* 94-GT-131, 1994.

[42] D.W. Childs, "Clearance effects on spiral vibrations due to rubbing," in *Proceedings of the ASME - Design Engineering Technical Conference*, San Francisco, CA, October 1997, DETC97/VIB-4058.

[43] A. Guinzburg, C.E. Brennen, A.J. Acosta, and T.K. Caughey, "The effect of inlet swirl on the rotordynamic shroud forces in a centrifugal pump," *ASME Journal of Engineering for Gas Turbines and Power*, vol. 115, pp. 287–293, 1993.

[44] Y. Hsu and C.E. Brennen, "Effect of swirl on rotordynamic forces caused by front shroud pump leakage," *Journal of Fluids Engineering*, vol. 124, pp. 1005–1010, 2002.

[45] J.K. Whalen, "The use of engineering thermoplastics for centrifugual compressor labyrinth," in *Proceedings of 23rd Turbomachinery Symposium*, Turbomachinery Laboratory, Texas A&M University, College Station, TX, 1994, pp. 81–89.

[46] J.K. Whalen, "Thermoplastics labyrinth seals for centrifugal compressors," in *Proceedings of 33rd Turbomachinery Symposium*, Turbomachinery Laboratory, Texas A&M University, College Station, TX, 2004, pp. 113–125.

[47] J. Armstrong and F. Perricone, "Turbine instability solution - honeycomb seals," in *Proceedings of 25th Turbomachinery Symposium*, Turbomachinery Laboratory, Texas A&M University, College Station, TX, pp. 47–56.

[48] N. Benabould, M. Borchi, and A. Tesei, "Hassi r'mel high pressure injection project with centrifugal compression," in *Proceedings of Second European Congress on Fluid Mechinery for the Oil, Petrochemical, and Related Industries*, Vienna Austria, June 1984, pp. 167–176.

[49] U. Baumann, "Rotordynamic stabilty tests on high-pressure radial compressors," in *Proceedings of 28th Turbomachinery Symposium*, College Station, TX., October 1999, pp. 115–122.

[50] Y. Wang, C. Young, G. Snowsill, and T. Scanlon, "Study of airflow features through step seals in the presence of disengagement due to axial movement," in *Proceedings of ASME TURBO EXPO 2004*, Vienna, Austria, June 2004, GT2004-53056.

[51] D.L. Rhode and R.G. Adams, "Rub-groove width and depth effects on flow predictions for straight-through labyrinth seals," *ASME Journal of Triboloy*, vol. 1126, pp. 781–787, 2004.

[52] B.E. Launder and D.B. Spalding, "The numerical computation of turbulent flow," *Computer Methods in Applied Mechanics and Engineering*, vol. 3, pp. 269–289, 1974.

[53] Y. Kanemori and T. Iwatsubo, “Forces and moments due to combined motion of conical and cylindrical whirls for a long seal,” *ASME Journal of Triboloy*, vol. 116, pp. 489–498, 1994.

[54] E. Soto and D.W. Childs, “Experimental rotordynamic coefficient results for: (a) a labyrinth seal with and without shunt injection and (b) a honeycomb seal,” *ASME Journal of Engineering for Gas Turbines and Power*, vol. 121, pp. 153–159, 1999.

[55] H.F. Black, “Interaction of a whirling rotor with a vibrating stator across a clearance annulus,” *Journal of Mechanical Engineering Science*, vol. 10, pp. 1–12, 1968.

[56] F.F. Erich and O’Connor J.J., “Stator whirl with rotor in bearing clearance,” in *ASME Paper 66. WA/MD-8*, 1966.

[57] A Muszynska, “Rotor-to-stator element rub-related vibration phenomena in rotating machinery - literature review,” *Shock and Vibration Digest*, vol. 21, pp. 3–11, 1989.

[58] T. Iwatsobu and Y. Iwasaki, “Experimental and theoretical study on swirl-braked labyrinth seal,” in *Proceedings of the 6th International Conference on Rotor Dynamics (IFToMM)*, London, England, October 1989, pp. 564–572.

VITA

Jinxiang Xi was born on July 30, 1974 in Ju-Yie, Shandong, China. He received his B.S. degree in July 1996 from Shanghai Jiaotong University and his M.S. degree in June 1999 from Xi'an Jiaotong University, both in Mechanical Engineering. He conducted spray research for one year at the University of California, Irvine before he transferred to Texas A&M University to pursue his Ph.D. degree in Sept. 2001. His areas of research interest are Computational Fluid Dynamics, Rotordynamics, Spray Combustion, and Multiphase Flow. Jinxiang Xi married Xiuhha Si in 2002, and has a son, Jensen Siyuan. He can be reached at:

1051 Austin Ave.
College Station, TX 77845